



VCU

Virginia Commonwealth University
VCU Scholars Compass

Theses and Dissertations

Graduate School

2021

Biomass-derived Electrode Materials and Sustainable Processes for Supercapacitors

Katelyn M. Shell
Virginia Commonwealth University

Follow this and additional works at: <https://scholarscompass.vcu.edu/etd>

 Part of the [Bioresource and Agricultural Engineering Commons](#), [Other Chemical Engineering Commons](#), and the [Other Materials Science and Engineering Commons](#)

© Katelyn M. Shell

Downloaded from

<https://scholarscompass.vcu.edu/etd/6830>

This Dissertation is brought to you for free and open access by the Graduate School at VCU Scholars Compass. It has been accepted for inclusion in Theses and Dissertations by an authorized administrator of VCU Scholars Compass. For more information, please contact libcompass@vcu.edu.

Biomass-derived Electrode Materials and Sustainable Processes for Supercapacitors

A dissertation submitted in partial fulfillment of the requirements for the degree of Doctor of Philosophy at Virginia Commonwealth University.

by

Katelyn Maria Shell

Bachelor of Science in Chemical and Life Science Engineering from Virginia Commonwealth University, May 2018

Bachelor of Science in Chemistry from Virginia Commonwealth University, May 2018

Associate of Science in Engineering from Virginia Western Community College, May 2015

Advisor: Dr. Ram B. Gupta

Virginia Commonwealth University

Richmond, Virginia

September, 2021

Acknowledgements

It is hard to express the gratitude owed to all of those who helped me achieved my goals. I would not be where I am today without the support I received over the past several years. To all of you who were present physically and in spirit, I thank you.

I would like to express my sincerest gratitude to Dr. Ram B. Gupta for offering his first-hand support of my research and studies. From an undergraduate in his lab to now, he has allowed me to pursue my own research interests while offering much needed guidance along the way. He has taught me to think outside-of-the-box and pushed me to learn new skills I never thought I would have. I would like to give a special thank you to Dr. Nastassja Lewinski who has been there for me since my undergraduate years. She allowed me to enter her office at any moment to share my thoughts, concerns, and triumphs. I would like to thank the remaining members of my committee Dr. Stephen Fong, Dr. Hani El-Kaderi, and Dr. Katherine Tibbetts. You have read my work, listened to my talks, and given me insightful comments to help me become a better researcher and professional.

I would like to give special thank you to Dr. Dylan D. Rodene for being my mentor in the beginning and becoming both a professional colleague and great friend. He guided me in my first days as a graduate student and devoted countless hours to help me become a stronger writer and presenter. To other members of the Gupta group, namely Ms. Jethrine Mugumya, Dr. Julian Bobb, and Dr. Gaind Pandey, I truly appreciate all of your contributions over the last few years. I would like to thank the many members of the El-Kaderi, both past and present: Alex Richard for teaching me BET methods and always promoting great conversations in the area of carbon-based materials, Mohammad Shehab who is a great friend and was always there to help with the Nova instrument

and glovebox, Dr. Nazgol Norouzi, Dr. Shamara K. Weeraratne, and Dr. Ahmed A. Abdelkader. You have all given your time and selfless effort towards aiding me in my goals. I am truly thankful to my undergraduate students, Mr. Shaan Y. Vohra and Mr. Robert F. Rafferty. Not only did I teach you how to be successful researchers, but you taught me how to be a leader and an educator.

I would like to thank the United States Department of Energy as various works presented were financially supported by DOE grant No. DE-EE0008252 (Pilot-Scale Biochemical and Hydrothermal Integrated Biorefinery (IBR) for Cost-Effective Production of Fuels and Value Added Products). To my collaborators, particularly those at South Dakota School of Mines (SDSMT) and Technology and Old Dominion University (ODU), I express my sincerest gratitude for continual project support. Dr. Vinod S. Amar, Mr. Bharathkiran Maddipudi, and Dr. Rajesh Shende at SDSMT and Mr. Anuj Thakkar and Dr. Sandeep Kumar at ODU have all worked tirelessly to deliver project goals.

Lastly, I would like to take a moment and thank the many members of my family and friends. To my parents Caroline D. and Marcus (Mark) P. Shell, you raised me to be strong, independent, kind, and resourceful. I appreciate everything you've ever done for me. To my significant other, Taylor A. Nelson, you have been my biggest support. You walked into this adventure with me, given me numerous inspirational talks, helped me prepare for my presentations, and kept me sane through the most hectic moments. Now, I look forward to entering this new adventure with you. Tabitha S.M. Tracy and Chelsea (Elle) E. White, you have been my closest friends. Eric C. Shell, Jean R. (Granny) and Leslie D. Shell (Pepaw), Rosaline N. (Sitti) and Samuel N. Duvall (Granddaddy), the Nelsons, and the Saunders, all of you have supported me throughout my life, watched me grow, and witnessed my success along the way. To my other friends and family, I thank you for your continued support and I am always here to return the favor.

Table of Contents

List of Tables	vii
List of Figures.....	viii
Chapter I. Introduction of Biomass-Derived Electrochemical Energy Storage Materials	1
<i>1.1 Introduction of Electrochemical Energy Storage Types</i>	<i>2</i>
1.1.1 Energy Demand	2
1.1.2 Electrochemical Energy Storage Types.....	3
1.1.3 Supercapacitors.....	5
<i>1.2 Biomass as an Electrode Material</i>	<i>6</i>
1.2.1 Sources and Characteristics	6
1.2.2 Activation Techniques.....	8
1.2.3 Economic Viability.....	9
<i>1.3 Integrated Biorefinery.....</i>	<i>9</i>
<i>1.4 Specific Aims</i>	<i>11</i>
<i>1.5 Layout of Dissertation.....</i>	<i>12</i>
Chapter II. Production of Levulinic Acid and Biocarbon Electrode Material from Corn Stover Through an Integrated Biorefinery Process.....	14
<i>2.1 Introduction.....</i>	<i>15</i>
<i>2.2 Experimental</i>	<i>18</i>
2.2.1 Synthesis of biocarbon electrode material from solid residue.....	18
<i>2.3 Results and Discussion.....</i>	<i>20</i>
2.3.1 Analysis of biocarbon produced from solid residue.....	21
2.3.2 Electrochemical Performance.....	24
<i>2.4 Conclusions</i>	<i>25</i>
Chapter III. Supercapacitor Performance of Corn Stover-Derived Biocarbon Produced from the Solid Co-products of a Hydrothermal Liquefaction Process	27
<i>3.1 Introduction.....</i>	<i>28</i>
<i>3.2 Experimental</i>	<i>32</i>
3.2.1 Materials	32
3.2.1 Production of Biochar via Hydrothermal Liquefaction.....	33
3.2.2 Facile one-step carbonization process	34
3.2.3 Physical characterization	35
3.2.4 Electrochemical measurements	35
3.2.5 Statistical analysis.....	37
<i>3.3 Results and Discussion.....</i>	<i>38</i>
3.3.1 Physical characterizations.....	38

3.3.2 Electrochemical Characterizations	44
3.3.3 Optimization statistical analysis	51
3.3.4 Perspectives	54
3.4 Conclusions	54
Chapter IV. Production of Supercapacitor Carbon Electrodes from Corn-stover via a Facile Thermal Activation.....	55
4.1 Introduction.....	56
4.2 Experimental	57
4.2.1 Materials	57
4.2.2 Biochar synthesis.....	58
4.2.3 Biocarbon Synthesis	59
4.2.4 Electrode Fabrication.....	59
4.3 Results and Discussion.....	60
4.4 Conclusions	65
Chapter V. Phytoremediation of Nickel via Water Hyacinth for Biocarbon-derived Supercapacitor Applications.....	67
5.1 Introduction.....	68
5.2 Materials and Methods.....	71
5.2.1 Materials	71
5.2.2 Water Hyacinth Cultivation and Harvesting	72
5.2.3 Production of Biocarbon.....	72
5.2.4 Physical Characterizations.....	73
5.2.5 Electrochemical Characterizations	73
5.3 Results and Discussion.....	75
5.3.1 Physical Characterizations.....	77
5.3.2 Electrochemical Characterization.....	86
5.4 Conclusions	90
Chapter VI. Graphitized Biocarbon Derived from Hydrothermally Liquefied Low Ash Content Corn Stover.....	92
6.1 Introduction.....	94
6.2 Materials and Methods.....	97
6.2.1. Materials	97
6.2.2 Corn Stover pre-processing	98
6.2.3 Conversion of corn stover to biochar via HTL.....	98
6.2.4 Catalytic and thermal activation of biochar.....	98
6.2.5 Biocarbon Synthesis and Electrode Fabrication.....	99
6.2.6 Characterizations	100
6.3. Results and Discussion.....	103

6.4. Conclusions	115
Chapter VII. Process Scale-up Modeling and Technoeconomic Analysis of Biocarbon Production	117
7.1 Introduction.....	118
7.2 Methods	120
7.2.1 Bench Scale Process	120
7.2.2 Aspen Plus Model.....	121
7.2.3 Technoeconomic Analysis.....	122
7.3 Results and Discussion.....	123
7.3.1 Aspen Plus Modeling.....	125
7.3.2 Technoeconomic Analysis.....	129
7.3.3 Limitations of the Model	133
7.4 Conclusions	134
Chapter VIII. Conclusions and Future Directions	135
8.1 Dissertation Conclusions	136
8.2 Future Directions	139
References	141
Appendix A1. Electrode and Coin Cell Fabrication	175
Appendix A2. Electrochemical Test Set-up	179
Appendix A3. CHI Code for Electrochemical Testing 3-Cell.....	181
Appendix A4. CHI Code for Electrochemical Testing 2-Cell.....	185
Appendix A5. VBA Code for Long Term Chronopotentiometry.....	188
Appendix A6. Supplemental for Supercapacitor Performance of Biocarbon Produced from Non-catalytic Hydrothermal Liquefaction of Corn Stover Biomass.....	191
Appendix A7. Supplemental for Phytoremediation of Nickel via Water Hyacinth for Biocarbon-derived Supercapacitor Applications.....	195
Appendix A8. Supplemental for Electrochemical Studies on Graphitized Biocarbon Derived from Hydrothermally Liquefied Low Ash Content Corn Stover	199
Appendix 9A. Mechanism of Electrochemical Impedance Spectroscopy (EIS).....	202

List of Tables

Table 2.1. Summary of conditions and results for solid residue-P1 and solid residue-P2.

Table 3.1. Hydrothermal liquefaction (HTL) parameters for received biochar.

Table 3.2 S_{BET} parameters for selected samples calculated from N_2 adsorption-desorption isotherms.

Table 3.3 Crystallite size, interplanar distance, and specific capacitances at 5 mV s^{-1} of selected samples.

Table 3.4. Collected corn-derived biocarbon data for supercapacitor applications.

Table 4.1. List of experimental parameters for HTL of corn stover-derived biochar.

Table 4.2. Summary of EIS data for biocarbons.

Table 5.1 Concentration and bioconcentration factor (BCF) of Ni in WH biomass after 14 days, determined from ICP-OES.

Table 5.2. BET surface area, pore volume, pore size analysis, Raman $I_{\text{D}}:I_{\text{G}}$ ratios, and percent yield for WH biochar and biocarbon.

Table 5.3. Summary of electrochemical results.

Table 5.4 Literature results of various activated biocarbons for supercapacitor applications.

Table 6.1. Tabulated summary of presented results.

Table 6.2. Literature values of corn-derived biocarbons*

Table 7.1. Ultimate analysis of corn stover-derived biochar

Table 7.2. Descriptions of each stream represented in the Aspen plus flow diagram

Table 7.3. Equipment list, capacities, materials of construction, cost for individual units and company of manufacture.

Table 7.4. Manual calculations of costs related to pilot scale biocarbon plant with years to payoff.

List of Figures

Figure 1.1. United States primary consumption of energy by source in 2020.

Figure 1.2. Ragone plot of the four main types of energy storage technologies as a function of specific energy and specific power.

Figure 1.3. Diagram depicting various attributes of a supercapacitor.

Figure 1.4. Chemical structure of lignin, the main component of lignocellulosic biomass.

Figure 1.5. Proposed example of an integrated biorefinery.

Figure 2.1. Proposed conversion scheme for corn stover to levulinic acid and biocarbon electrode material with detailed process insets.

Figure 2.2. [A] Hysteresis loop of solid residue-P1 and solid residue-P2, and [B] pore size distribution of solid residue-P1 and solid residue-P2 biocarbons.

Figure 2.3. [A] CV curves of solid residue-P1 and solid residue-P2 at 5 mV s^{-1} , [B] CV curves of solid residue-P2 at various scan rates between 5 and 100 mV s^{-1} , [C] CD curves of solid residue-P1 and solid residue-P2 at 0.05 A g^{-1} .

Figure 3.1. Schematic of simplified integrated biorefinery processes with emphasis on biocarbon synthesis, supercapacitor preparation, and electrochemical testing.

Figure 3.2. SEM images taken at two magnifications to depict [A] the distribution of particle sizes and [B] surface morphologies of UHS-SDC9 biocarbon.

Figure 3.3. Physical characterization of biocarbons: [A] BET hysteresis plot of UHS-SDC9, [B] pore size distribution of UHS-SDC2 (control) and UHS-SDC9, [C] Raman spectra, and [D] XRD spectra of UHS-SDC1, UHS-SDC2, UHS-SDC4, UHS-SDC8, and UHS-SDC9.

Figure 3.4. Electrochemical characterization of the biocarbons: [A] CV overlays at 5 mV s^{-1} , [B] stacked CV curves of material UHS-SDC9 from $5\text{--}100 \text{ mV s}^{-1}$, [C] CD overlays at 0.05 A g^{-1} , [D] CD stacked curves of UHS-SDC9 from $0.05\text{--}5 \text{ A g}^{-1}$.

Figure 3.5 [A] Specific capacitance plotted with respect to current density obtained from CD for UHS-SDC9 biocarbon and [B] capacitance retention at 1 A g^{-1} for 2500 CD cycles for UHS-SDC9 with each point representing every 10^{th} cycle.

Figure 3.6 Least squares regression model for the effect of [A] HTL parameters and [B] physical characteristics of biocarbons on specific capacitance (CV at 5 mV s^{-1}). Surface contour plots for the prediction profile of [C] mass to water ratios and reaction time, and [D] pore volume and degree of graphitization as a function of specific capacitance (CV at 5 mV s^{-1}).

Figure 4.1. Cyclic voltammetry curves of prepared biocarbons at 5 mV s^{-1} .

Figure 4.2. Charge-discharge curves for prepared biocarbons at 0.1 A g^{-1} .

Figure 4.3. Electrochemical impedance spectroscopy of prepared biocarbons.

Figure 5.1. Process flow diagram for proposed phytoremediation of Ni to biocarbon product.

Figure 5.2. SEM images of WH-5 [A, C] biochar and [B, D] biocarbon, where [C] and [D] are reference images collected from the EDS analysis. Elemental maps of [C] and [D] show C, O, K, and Ni; and C, O, Al, and Si for WH-0 and WH-5, respectively.

Figure 5.3. BET pore size distribution and hysteresis plot of WH-0, WH-5, and WH-10 biocarbons.

Figure 5.4. ATR-FTIR spectra of WH-0, WH-5, WH-10, WH-25 [A] biomass, [B] biochar, and [C] biocarbon. Raman spectra of WH-0, WH-5, WH-10, WH-25 [D] biochar and [E] biocarbon. [F] XRD Spectra of WH-0, WH-5, WH-10, and WH-25 biocarbon.

Figure 5.5. [A] CV curves of WH-0, WH-5, WH-10, and WH-25 biocarbons at a scan rate of 5 mV s^{-1} , [B] CV curves of WH-5 biocarbon at scan rates $5 - 100 \text{ mV s}^{-1}$, [C] CD curves of WH-0, WH-5, WH-10, and WH-25 biocarbons at 0.1 A g^{-1} , [D] CD curves of WH-5 biocarbon at current densities $0.1 - 10 \text{ A g}^{-1}$ (inset: CD curves of higher current densities), [E] EIS spectra and [F] power density v. energy density for WH-0, WH-5, WH-10, and WH-25 biocarbons.

Figure 6.1. Anaerobic HTL conversion of Corn Stover to biochar and its activation via ZnCl_2 at $450 \text{ }^\circ\text{C}$.

Figure 6.2. Hypothetical molecular representation of lignin with linkages and subsequent products.

Figure 6.3. [A] Isotherms and [B] Pore size distribution of ZCNi and SDC5 biocarbons.

Figure 6.4. ATR-FTIR of ZCNi biochar and biocarbon with emphasis on wavenumbers between $1000 - 2000 \text{ cm}^{-1}$ (inset).

Figure 6.5. [A] Raman spectroscopy of ZCNi and SDC5 biochars and biocarbons. [B] XRD of ZCNi and SDC5 biocarbons.

Figure 6.6. CV graphs of ZCNi and SDC5 at 5 mV s^{-1} [A] and ZCNi at scan rates ranging $5 - 100 \text{ mV s}^{-1}$ [B]. Chronopotentiometry of ZCNi and SDC5 at 0.05 A g^{-1} [C] and ZCNi at current densities ranging $0.05 - 10 \text{ A g}^{-1}$ [D].

Figure 6.7. [A] EIS spectra of ZCNi and SDC5 biocarbon with high frequency region (inset) and [B] Stability data of ZCNi biocarbon over 10,000 cycles.

Figure 7.1. Block flow diagram of bench scale biocarbon production with process parameters and characterization details

Figure 7.2. Process flow diagram of proposed pilot scale biocarbon production plant.

Figure 7.3. Aspen Flow diagram representing the pilot plant process flow diagram as individual unit operations with modeled flow rates pre and post carbonization.

Abstract

Biomass is one of the most abundant natural resources and has been used as a source of energy for thousands of years. Biomass as a precursor for energy storage materials is still relatively novel and faces several obstacles before becoming commonly used in today's electrical devices. Currently, energy storage devices, such as batteries, capacitors, and supercapacitors, utilize petroleum-derived graphitic carbons for anodes, generating a need for more sustainable materials. Biomass, as a carbon-rich source for electrode materials, presents a viable and economically feasible alternative due to the prevalent lignocellulosic compounds: lignin, cellulose, and hemicellulose. Corn stover is an agricultural residue high in lignocellulosic components consisting of stalks, stems, leaves, husks, etc. and is produced at a rate of 1.5 dry tons per acre of harvested corn. Valorization of this crop in the form of an integrated biorefinery is detailed herein with emphasis on biocarbon production for use in electrodes.

Preliminary studies on the solid residues from the enzymatic hydrolysis of corn stover were conducted, where biocarbon synthesized via a two-step thermal activation at 375 °C followed by high temperature carbonization at 850 °C, underwent physical characterizations, such as Brunauer-Emmett-Teller (BET) and Scanning Electron Microscopy (SEM), to understand physical properties that lead to a better electrochemical performance. Electrochemical techniques such as cyclic voltammetry (CV) and chronopotentiometry (CD) were used to analyze electrode performance in aqueous electrolyte. Using the preliminary results on solid residues from the enzymatic hydrolysis of corn stover, next level optimization studies were conducted by varying hydrothermal liquefaction (HTL) parameters and converting subsequent solid residues into biocarbon for electrodes. Physical and electrochemical characterizations expand upon previous experiments to include X-ray diffraction crystallography (XRD), Raman spectroscopy, and long-

term CD performance. Statistical analyses were conducted to understand how HTL conditions and physical parameters affect electrochemical performance. Subsequent catalytic HTL studies involving $\text{Ni}(\text{NO}_3)_2$, $\text{Ni}(\text{OH})_2$, $\text{Ca}(\text{OH})_2$, K_2CO_3 , and ZnCl_2 were performed, where resulting solid residues were converted into biocarbon following the established thermal methods. Physical characterizations build on previous experiments with enhanced electrochemical performance, such as electrochemical impedance spectroscopy (EIS), were carried out.

Another exciting opportunity is in the valorization of biomass that comes out of phytoremediation of nickel containing soils, as the biomass inherently contains nickel catalyst. Enhanced catalytic methods were demonstrated through the utilization of phytoremediation techniques where hyperaccumulator species (water hyacinth) was cultivated in Ni^{2+} doped water and converted into electrode grade biocarbon through thermochemical/catalytic methods. Electrochemical results demonstrated a high specific capacitance of 541 F g^{-1} for activated carbons. Physical characterizations, such as BET and Raman spectroscopy, denoted surface areas in excess of $3000 \text{ m}^2 \text{ g}^{-1}$, pore volumes reaching $2.13 \text{ cm}^3 \text{ g}^{-1}$, and enhanced C=C formation contributing to the high specific capacitance.

Process scale-up analysis was performed on corn stover-derived biocarbon production. Aspen Plus simulations and techno-economic analyses (TEA) were conducted on the scaled methods with results indicating achievable production goals and an economically favorable process. Areas of research presented here encompass sustainable engineering, process intensification, energy storage, catalysis, phytoremediation, economics, statistical modeling, and computer simulation.

Chapter I. Introduction of Biomass-Derived Electrochemical Energy Storage Materials

1.1 Introduction of Electrochemical Energy Storage Types

1.1.1 Energy Demand

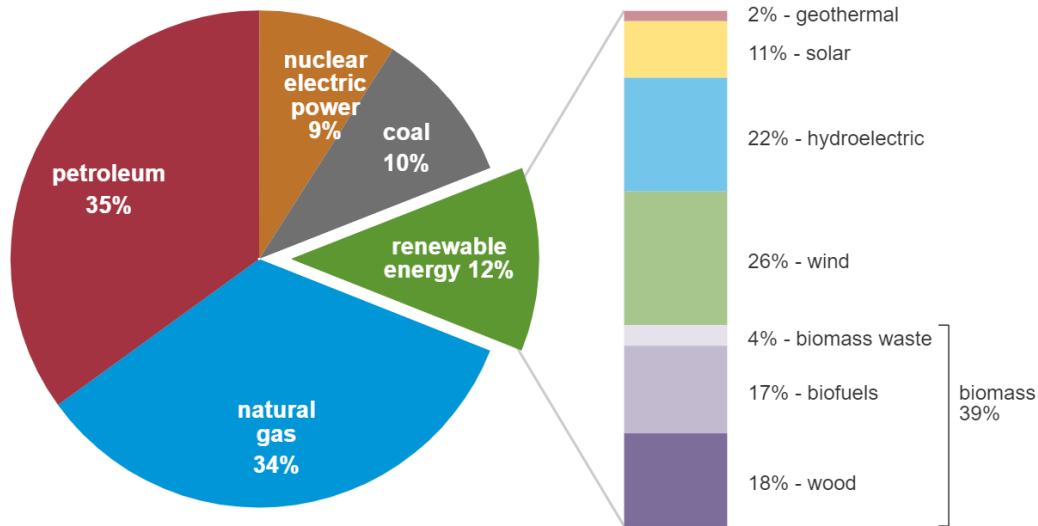
Global energy demands are foreseen to rise nearly 50% by 2050, leading to energy usage exceeding 250,000 TWh.^[1] Transportation alone is expected to increase 40% between now and 2050, particularly in Asia and countries outside the Organization for Economic Cooperation and Development (OECD).^[1] Currently, renewable sources make up 29% of the global electricity generation, a 2% increase since 2019, and is projected to increase by 3.1% each year in the future.^[2] Since 2020, bioenergy alone has increased from 40 TWh yr⁻¹ to 72 TWh yr⁻¹.^[2] This increase in renewable energy generation is due to emphases placed on reducing CO₂ and GHG emissions in an effort counteract climate and ecological detriments. It is imperative to continue developing alternative methods of energy generation and storage to further reduce our carbon footprint.

In the U.S., renewable energy comprises 12% (~3400 TWh) of the total yearly energy consumption (Figure 1.1).^[3] Of this, nearly 40% is from biomass sources such as biofuels (17%), wood/woody products (18%), and various biomass related wastes (4%).^[3] More than 700 million dry tons of biomass is readily available for use, however the U.S. only uses 68 million tons (~10%) currently.^[4] With a potential of 205 million dry tons available from biomass waste sources, it is necessary to investigate multiple methods for utilizing biomass.^[4]

U.S. primary energy consumption by energy source, 2020

total = 92.94 quadrillion
British thermal units (Btu)

total = 11.59 quadrillion Btu



Source: U.S. Energy Information Administration, *Monthly Energy Review*, Table 1.3 and 10.1, April 2021, preliminary data
 Note: Sum of components may not equal 100% because of independent rounding.

Figure 1.1. United States primary consumption of energy by source in 2020.^[3]

1.1.2 Electrochemical Energy Storage Types

There are four main types of electrochemical energy storage devices that are commercially available: capacitors, supercapacitors, batteries (Li-ion), and fuel cells. Capacitors are useful for applications that require rapid charge and discharge of energy such as microelectronics, radios, etc. Rapid charge-discharge characteristics are achieved through electrostatic interactions with higher capacitance achieved through dielectrics. Supercapacitors are relatively new in the commercial market and can hold up to a million times more energy over standard capacitors while still maintaining rapid charge and discharge characteristics. Many supercapacitors achieve this through the same principles as standard capacitors, however some research has been directed towards supercapacitors that achieve high energy storage through faradaic reactions. Batteries,

such as Li-ion, rely on faradaic redox reactions to achieve high energy storage, however charge and discharge processes are slower. This has made them suitable for longer term energy storage needs leading to their popularity. Fuel cells, similar to batteries, operate through faradaic redox reactions and can store more energy than batteries. Contrary to batteries, fuel cells must have a constant supply of fuel which makes them costlier and less compact than other forms of energy storage. Figure 1.2 compares these forms of energy storage in a Ragone plot where the x-axis and y-axis are specific energy (Wh kg^{-1}) and specific power (W kg^{-1}), respectively.

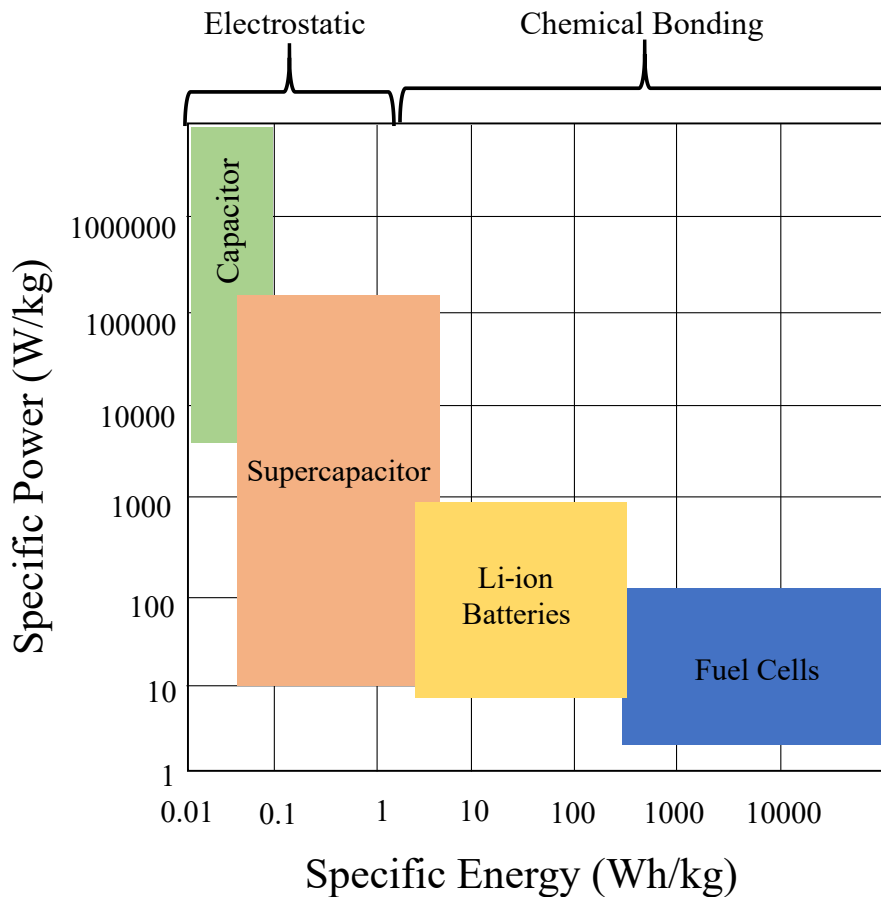


Figure 1.2. Ragone plot of the four main types of energy storage technologies as a function of specific energy and specific power.

1.1.3 Supercapacitors

Revered for their extended life, great stability and high power density, supercapacitors are gaining a great deal of attention and becoming more present commercially for use in smart grid systems and hybrid electric vehicles.^{[5],[6]} Unfortunately, electrodes for the commercial supercapacitors are currently produced via coking processes of fossil fuels, which is neither renewable nor sustainable.^[6] Meanwhile, current supercapacitor materials have lower energy densities than Li-ion batteries.^[7] This means supercapacitors do not hold as much energy as Li-ion batteries, but they can discharge orders of magnitude faster, leading to its higher power density. Enhancement of material properties via physical and chemical routes leads to a higher performance overall, generating a need for advanced energy materials research.

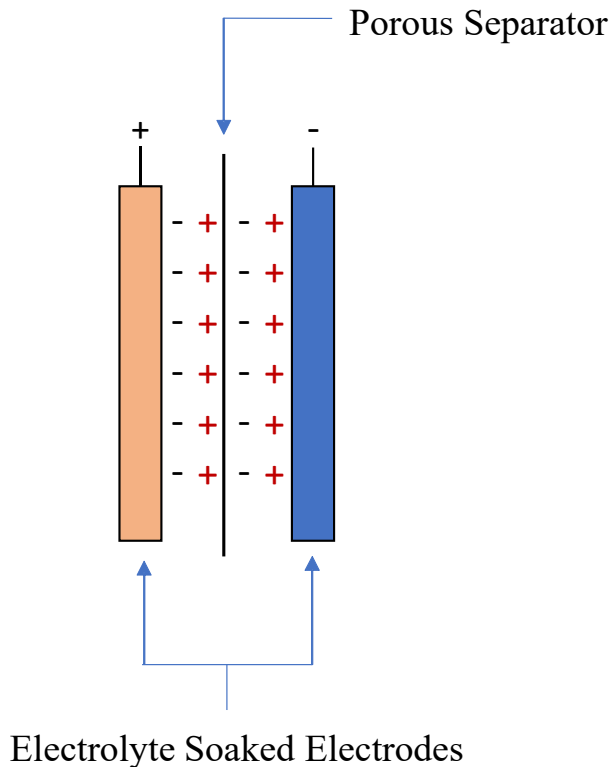


Figure 1.3. Diagram depicting various attributes of a supercapacitor.

There are two categories of supercapacitors; electrochemical double layer capacitors (EDLCs) and pseudocapacitors (PCs).^[8] Of the EDLCs, symmetrical supercapacitors are comprised of three main attributes: two identical electrodes, a semipermeable separator, and electrolyte soaked into the electrode material (Figure 1.3).^{[9],[10]} The charge storage mechanism for supercapacitors occurs when a voltage is applied to transfer ions from the electrolyte solution to cover the surface and fill pores of the electrode material.^[10] Naturally, this means higher porosity gives a higher capacitance and therefore, higher surface areas.^[11] However, there is a limiting factor to porosity where pores must be at least two-fold larger than electrolyte ions which have a hydrodynamic radius on the sub-nm scale.^[12] Most pores below 0.8 nm are not viable for ionic storage, limiting the specific capacitance of the material.^[13] Pores are classified as microporous (< 2 nm), mesoporous (2–50 nm), and macroporous (> 50 nm) with the lower end of the mesoporous range (0.8–3 nm) being ideal for proper ion mobility and adsorption.^{[14],[15]} Desired pore structures can be efficiently obtained from biomass, a prominently researched precursor materials for supercapacitors.^[16]

1.2 Biomass as an Electrode Material

1.2.1 Sources and Characteristics

There are four main types of biomasses: agricultural residues, animal wastes, fermentation wastes, and woody biomasses. Each of these offers unique characteristics suitable for production of value-added products such as those for soil amendments, high surface area materials for CO₂ capture, commodity chemicals and energy storage materials. Biomass is an abundant, low cost, and natural source for carbon that can be converted to activated biocarbon for use in EDLC supercapacitor electrodes, due to its excellent conductivity and chemical stability.^{[7],[17],[18]} Different sources of biomass offer unique characteristics corresponding to their biological features, with some offering

outstanding capabilities to withstand metal toxins, known as hyperaccumulators.^[19] In this light, it becomes more apparent that utilization of these resources and their subsequent proficiencies is necessary for growing energy demands.

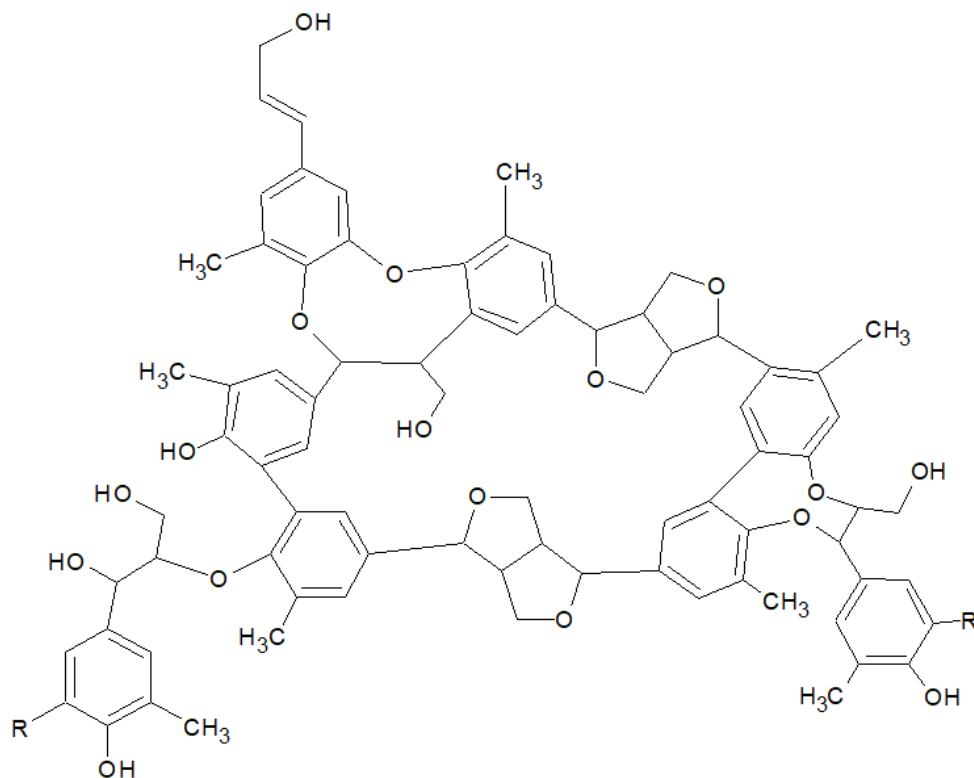


Figure 1.4. Chemical structure of lignin, the main component of lignocellulosic biomass.

Biomass is generally comprised of three main components: lignin, hemicellulose, and cellulose. While various biomasses may differ, lignin (Figure 1.4) makes up about 25% of most plants and is a biopolymer with a plethora of uses. The primarily carbon structure with numerous functional groups (-OH, -COOH, -COH) provides an excellent template for biocarbon activation with implications in energy storage. During activation, the functional groups are cleaved generating pore structures. Moreover, activation at high temperatures promotes the formation of C=C bonds and crosslinking leading to increased crystallinity.

1.2.2 Activation Techniques

Biomass can be converted to biocarbon via thermal, thermochemical, or catalytic routes. Thermal treatment increases graphitization, thus increasing conductivity, and creates graphitic structures that allow for interconnected pore networks, which leads to greater ion mobility within the framework.^{[20],[21]} Temperatures in excess of 1500 °C during activation would achieve highly ordered graphitic biocarbon and increase conductivity at the expense of pore structures and surface area. Therefore, maintaining a balance between hierarchal porous structures and graphitization is key in producing high performance biocarbon for electrochemical applications.^[22]

Thermochemical activation routes involve the addition of extremely acidic or basic compounds (i.e. KOH, H₃PO₄, etc.) in conjunction with thermal methods. This activation route typically produces biocarbons with large surface areas and microporous structures that are likely associated with disconnected pore networks and limited ion transport, respectively.^[23] In this method, it is important to increase both the crystallinity and hierarchal pore structures, in order to facilitate the generation of ion mobility networks. This is where metal catalysts may aid in the formation of such structures. Additionally, electrochemical performance may increase when utilizing thermochemical methods, however there are additional steps (addition, removal, neutralization, drying) that add cost.

Thermocatalytic activation utilizes either metal or non-metal catalysts, generally after the biomass has been harvested (post adsorbed), for aiding in functional group bond cleavage during thermal treatment. When using metal catalysts, activation temperatures can be lowered, thus saving energy.^[24] Graphitization and pore networks are generally enhanced via thermocatalytic activation routes, however the costly and/or toxic nature of some catalysts pose problems to scaling and an

environmental threat. Given this, it is crucial to develop synergistic activation methods that increase electrochemical performance, are cost effective and environmentally benign.

1.2.3 Economic Viability

The economic viability of biomass, converted to biocarbon, is increasing with the development of more efficient processes that use less energy, generate less wastes, and/or recycle waste streams. The current cost of lignocellulosic biomass is ~\$60 per metric ton (dry basis) in the U.S, where the selling price of biocarbon is \$6000 per metric ton (dry basis).^[25] Co-currently, biocarbon, as an electrode material, can be used in hybrid-electric systems, such as regenerative braking, with other uses in smart grid systems and handheld electronics giving substantial economic value and the necessity of its research. Given that feedstocks are renewable, biocarbon is a sustainable material that will help meet the worlds energy demands.

1.3 Integrated Biorefinery

An integrated biorefinery is a novel concept that generates multiple value-added products from a single feedstock. Like classical biorefineries, IBRs produce multiple products that optimize production economics and use the majority of the feedstock.^[26] However, unlike classical biorefineries, IBRs provide the possibility to obtain energy products, such as electricity, heat and biofuels in addition to multiple other bio-based products.^[26] This inherently reduces transport costs and energy consumption while creating a diverse product portfolio.^[26] Currently, standard biorefineries have difficulties in the competitive market against petroleum industry which prevents biofuels from becoming widespread.^[27] IBRs tend to be more complex which poses technical and market risks, thus it is vital to simplify and address technoeconomic factors early in order to successfully implement IBRs.^[27]

1.4 Specific Aims

This dissertation presents in depth examination of biocarbon production utilizing several different biomass feedstocks and activation methods. Physical characterizations, such as BET, ATR-FTIR, SEM, XRD, and Raman spectroscopy are utilized in the examination of surface properties of biocarbon. Electrochemical characterizations, such as CV, CD, and EIS give insight into how the material performs when fabricated into an electrode. Utilizing physical characterization results to explain electrochemical phenomena will help in answering the following scientific questions: (a) What biomass, or type of biomass, feedstock is better for biomass-derived carbons destined for electrochemical applications, particularly supercapacitors? (b) Are certain physical parameters more conducive for enhanced electrochemical performance over others? (c) How are surface areas and pore structures effected by different materials, processing parameters, and activation techniques? (d) How pre-adsorbed catalysts enhance material properties advantageous for electrochemical applications? (e) Is large scale biocarbon feasible for materials produced from an IBR? In order to sufficiently answer these questions, the dissertation will accomplish the following specific aims:

- ❖ Presentation of material processing methodologies for biocarbon production including pre and post adsorbed activation strategies.
- ❖ Analysis of surface areas, pore size distributions, average pore size, and isotherms through BET.
- ❖ Discussion of material properties pre and post activation through ATR-FTIR and Raman spectroscopy.
- ❖ Examination of morphological and topological properties of lignocellulosic biomass compounds through SEM imaging.

- ❖ Analysis of crystallinity, crystal size, and planar count of graphitic biocarbons through XRD crystallography.
- ❖ Investigation of electrochemical performance of biomass derived electrodes through CV, CD, and EIS with relation to material physical properties.
- ❖ Technoeconomic analysis and process scale-up modelling related to corn-stover derived biocarbons.

1.5 Layout of Dissertation

This dissertation was written in a chapter-section format to allow for each chapter to be read independently of each other. Given this, some introductory information, basic methods, and discussion results may be repeated. This allows the reader to refresh their knowledge of basic concepts related to biomass, supercapacitors, characterization methods, and related calculations. Below is the outline of this dissertation:

Chapter II demonstrates the viability of producing biocarbon from the solid waste streams of a pre-treatment process that co-produces levulinic acid (a biofuels precursor). Results discussed contain both physical and electrochemical characterizations that justify the utilization of waste streams for biocarbon production as part of an IBR.

Chapter III builds off the foundation provided in **Chapter II** for biocarbon production. The biocarbon source is corn stover that has undergone HTL in a design of experiments fashion. Results provided indicate HTL parameters that are conducive for enhanced electrochemical performance. Statistical analysis models HTL parameters and gives optimized conditions.

Chapter IV demonstrates the effect of various catalysts, during the HTL of UHS, on electrochemical performance with emphasis on catalysts costs for scalability.

Chapter V delivers a novel approach to thermochemical/catalytic activation of biomass utilizing hyperaccumulators. Phytoremediation techniques and their effect on physical and electrochemical results are discussed.

Chapter VI demonstrates the enhanced electrochemical performance of biocarbon produced from the catalytic HTL of corn stover utilizing nickel nitrate and zinc chloride. Results expand on knowledge gained from **Chapter III**.

Chapter VII delivers a techno-economic analysis and scaled modeling of biocarbon produced from a pilot plant facility. Energy and cost analyses are presented herein.

Chapter VIII discusses final conclusions and gives future directions that expand upon the knowledge discussed in this dissertation.

Appendices A1 – A8 details various fundamental aspects of the works presented. Supplemental materials such as computer code used for specific capacitance calculations, detailed instructions on electrode fabrication, further studies conducted on biomass feedstocks, and additional information relating to each chapter are detailed here.

Chapter II. Production of Levulinic Acid and Biocarbon Electrode Material from Corn Stover Through an Integrated Biorefinery Process

Adapted From:

Anuj Thakkar, **Katelyn M. Shell**, Martino Bertosin, Dylan D. Rodene, Vinod Amar, Alberto Bertucco, Ram B. Gupta, Rajesh Shende, and Sandeep Kumar. *Fuel Processing Technology* 213 (2021): 106644.

To overcome the inefficient biomass conversion, waste generation, and lack of co-production in biorefineries, an integrated process was proposed for the conversion of corn stover into levulinic acid and biocarbon electrode material. Corn stover was pretreated through hydrothermal process using 0.45 wt% K_2CO_3 which removed 76 wt% lignin and 85 wt% xylan while preserving 83 wt% glucan. This was followed by acid hydrolysis to produce levulinic acid at varying H_2SO_4 concentrations and reaction time in a batch reactor at 190 °C. At a reaction time of 5 min in 2 wt% H_2SO_4 , 35.8 wt% and 30 wt% glucan in raw and pretreated corn stover was converted to levulinic acid, respectively. The residue from acid hydrolysis was converted into biocarbon for supercapacitor electrodes via a two-step thermal activation process which showed a specific capacitance of 120 F g^{-1} . The proposed integrated biorefinery concept provides multiple value-added products for a greater financial and environmental sustainability.

2.1 Introduction

Despite the growing interest in bioeconomy and renewables, the biorefinery industry has struggled to achieve economic competitiveness. Some of the major bottlenecks biorefineries encounter are inefficient biomass conversion processes, waste generation, and lack of processes for co-production of value-added compounds.^{[29],[30]} To overcome these challenges, advanced approaches include integration of biofuel production with other products, which use biomass or process residues to make different co-products like biofuel, bio-chemicals, fertilizer, heat, energy, etc.^[31]

Corn stover is recognized as an important agricultural waste with many potential applications in growing bioeconomy.^[32] It is estimated that more than 100 million dry tons per annum of corn stover is produced in the USA alone.^[33] The chemical composition of various lignocellulosic

biomass differs considerably and is influenced by genetic and environmental factors.^[34] Lignocellulosic biomass like corn stover is composed of cellulose, hemicellulose, and lignin.^{[35],[36]} National Renewable Energy Laboratory (Denver, CO) reported levulinic acid as one of the top value-added chemicals produced from biomass. Levulinic acid is a member of the gamma-keto acid group which can be produced through acid-catalyzed dehydration and hydrolysis of hexose sugars.^{[37]–[39]} The most widely used method for levulinic acid production is acid catalyzed single step reaction without removing hemicellulose and lignin from the lignocellulosic biomass.^{[40]–[43]} Due to the formation of byproduct formic acid, the theoretical yield of levulinic acid from hexose is only 64.5 wt.%. Practically, the yield is even lower due to undesired side reactions.^[44] The acidic conditions also hydrolyze and hydrate pentoses in hemicellulose to furfural, which at harsher conditions, undergo further degradation.^[45] One of the major drawbacks of the lignocellulosic biomass to levulinic acid conversion process is unavoidable formation of solid byproduct, which is formed due to the decomposition of lignin, cellulose, and hemicellulose during acid catalyzed reactions to form intermediates that re-polymerize to insoluble material termed humins.^{[37],[46],[47]} The loss of hemicellulose and lignin to the degraded products can be reduced by carrying out the conversion into two separate steps, where the first step removes components other than cellulose from the biomass. These recovered hemicellulose and lignin derived components can be used to produce furfural, carbon microspheres, levulinic acid and other bio-based materials using suitable reaction conditions.^{[35],[39],[45],[48]} The most common first pretreatment step for the production of levulinic acid from biomass uses acidic conditions which sufficiently removes hemicellulose but not lignin.^{[45],[49]–[51]} Disposal issues and higher costs associated with the use of acids and alkalis for pretreatment also bring in additional economic and environmental challenges.^{[52]–[55]}

The first step using moderate alkaline hydrothermal condition has potential to pretreat biomass efficiently and economically. Hydrothermal reactions use water as reaction media which is environmentally benign and inexpensive. If not regulated, the pH of the hydrolysate produced during hydrothermal pretreatment decreases due to formation of organic acids. The use of potassium carbonate (K_2CO_3) to regulate pH of the reaction media is advantageous compared to pretreatment using acidic catalyst as there is no cost associated with acid recovery and handling.^[35] The pH range of 4–7 and a flow through reactor setup (described in section 2.1), minimizes the formation of degradation products that can catalyze hydrolysis of the cellulosic material during pretreatment.^{[56]–[62]} The reactive and soluble lignin fractions need to be rapidly removed from the system before they recondense and become part of biomass solid.^{[63],[64]} Liquid hydrolysate generated from the pretreatment of lignocellulosic biomass using K_2CO_3 in a flow through reactor, contains 25–45% of the initial biomass carbon, mostly in the form of sugars from hemicelluloses, degradation products such as furfural, lignin derived phenolic compounds, and carboxylic acids.^[35] In addition, literature suggests biomass is an excellent precursor material for energy storage devices, such as supercapacitors. In supercapacitors, the energy storage mechanism is created from an applied voltage, whereby ions are stored electrostatically on the surface and within the pores of the material.^[10] Currently, carbons from petroleum coking processes are utilized in the commercial production of supercapacitors, generating a need for more sustainable approaches for supercapacitor fabrication.^[6] Biomass is an excellent alternative electrode material due to its renewability, abundance, and the potential for high surface areas post activation. Corn derived biocarbons for energy storage applications has been previously reported with capacitances reaching higher than 300 F g^{-1} , with chemical or catalytic activation techniques.^{[65]–[69]} However,

the use of solid waste streams from the production of biofuel precursors in energy storage devices is a novel idea within the field of biomass derived energy storage devices.

In this work, the hydrothermal pretreatment (i.e., the first step) of corn stover was conducted in a flow through reactor using K_2CO_3 solution followed by batch acid hydrolysis (i.e., the second step) of pretreated biomass to produce levulinic acid using sulfuric acid (H_2SO_4). The solid residue produced during the acid hydrolysis was used as a starting material for the synthesis of electrode material for energy storage applications such as batteries and supercapacitors. To the best of our knowledge, biocarbon derived from solid residue has yet to be reported for its application as an energy storage material.

2.2 Experimental

Potassium carbonate (K_2CO_3), sulfuric acid (H_2SO_4), hydrochloric acid (HCl), ethanol (C_2H_5OH), and analytical grade standards were purchased from Fisher Scientific. Polytetrafluoroethylene (PTFE) and carbon black (Super P conductive, 99+ %) were purchased from Alfa Aesar. Nickel foam cathode material was purchased from MTI corp. Henkel Loctite EA 9462 Epoxy was purchased from Ellsworth adhesives. De-ionized water was used for all the experiments unless otherwise specified.

2.2.1 Synthesis of biocarbon electrode material from solid residue

Biocarbon derived from the solid residue was produced through a facile two-step thermal activation process (P2) without the use of catalysts or chemical activation agents. A standard acid washing process was utilized to clean the solid residue, where 1.0 g of solid residue was washed with 1.0 M HCl, sonicated for 10 min, centrifuged, and then decanted. This process was repeated to ensure a complete removal of impurities. The washed solid residue was neutralized with double

distilled water (18.2 M Ω) and then dried in a vacuum oven overnight at 50 °C. Next, the solid residue underwent thermal annealing in a horizontal tube furnace at 375 °C (ramp rate of 5 °C min⁻¹) for 2 h under argon flow. Samples were allowed to cool naturally, weighed, and then carbonized in a tube furnace at 850 °C (ramp rate of 5 °C min⁻¹) for 3 h under argon flow. The samples were cooled naturally and then prepared into electrodes. Electrode inks were prepared as a slurry consisting of an 8:1:1 ratio of solid residue, Super P, and PTFE respectively. Inks were spread evenly onto a 3 cm² nickel foam substrate. Electrodes were vacuum dried overnight at 50 °C. Next, the electrodes were templated and insulated using chemical resistant epoxy. A one-step activation process (P1) generated samples in a similar manner without performing the low temperature annealing step. Active areas were found prior to electrochemical testing. To find the active areas, a mass ratio technique was utilized where untemplated and templated loaded Ni foam supports were imaged, printed, and weighed.

Surface area characterizations were conducted via N₂ adsorption/desorption in a Quantichrome NOVA 2400e analyzer. All samples were degassed at 150 °C for 15 h prior to adsorption experiments. A Hitachi Model FE-SEM Su-70 scanning electron microscope (SEM) was utilized to examine surface morphology of the biocarbon. A flat aluminum specimen holder with double-sided carbon tape (Ted Pella Inc.) was used to analyze the samples.

An electrochemical workstation (CH Instruments, CHI 660E) was utilized for all electrochemical measurements in 2 M KOH. A conventional three electrode cell consisting of biocarbon electrodes, a platinum (Pt) wire, and an Ag/AgCl (sat. KCl) were used as the working, counter and reference electrodes, respectively. Cyclic voltammetry (CV) and chronopotentiometry as galvanostatic charge-discharge (CD) testing were used to find the specific capacitance of activated solid residue electrodes. The CV method was performed at scan rates of 5, 20, 50, and 100 mV s⁻¹. The CD

method was performed at 0.05 Ag^{-1} . The specific capacitances for the solid residue electrodes were determined for both CV and CD methods using Eqs. (2.1), (2.2), respectively.

$$C_s = \frac{\int_{V_1}^{V_2} I dV}{mv(V_2 - V_1)} \quad (2.1)$$

$$C_s = \frac{It}{m(V_2 - V_1)} \quad (2.2)$$

2.3 Results and Discussion

Figure 2.1 depicts the proposed conversion scheme for corn stover to levulinic acid and biocarbon electrode material with detailed process insets. All experiments were performed in duplicate and the reported results are averages of two values. The deviation associated with all the results was less than 5% except for the capacitance values which deviated up to 12%.

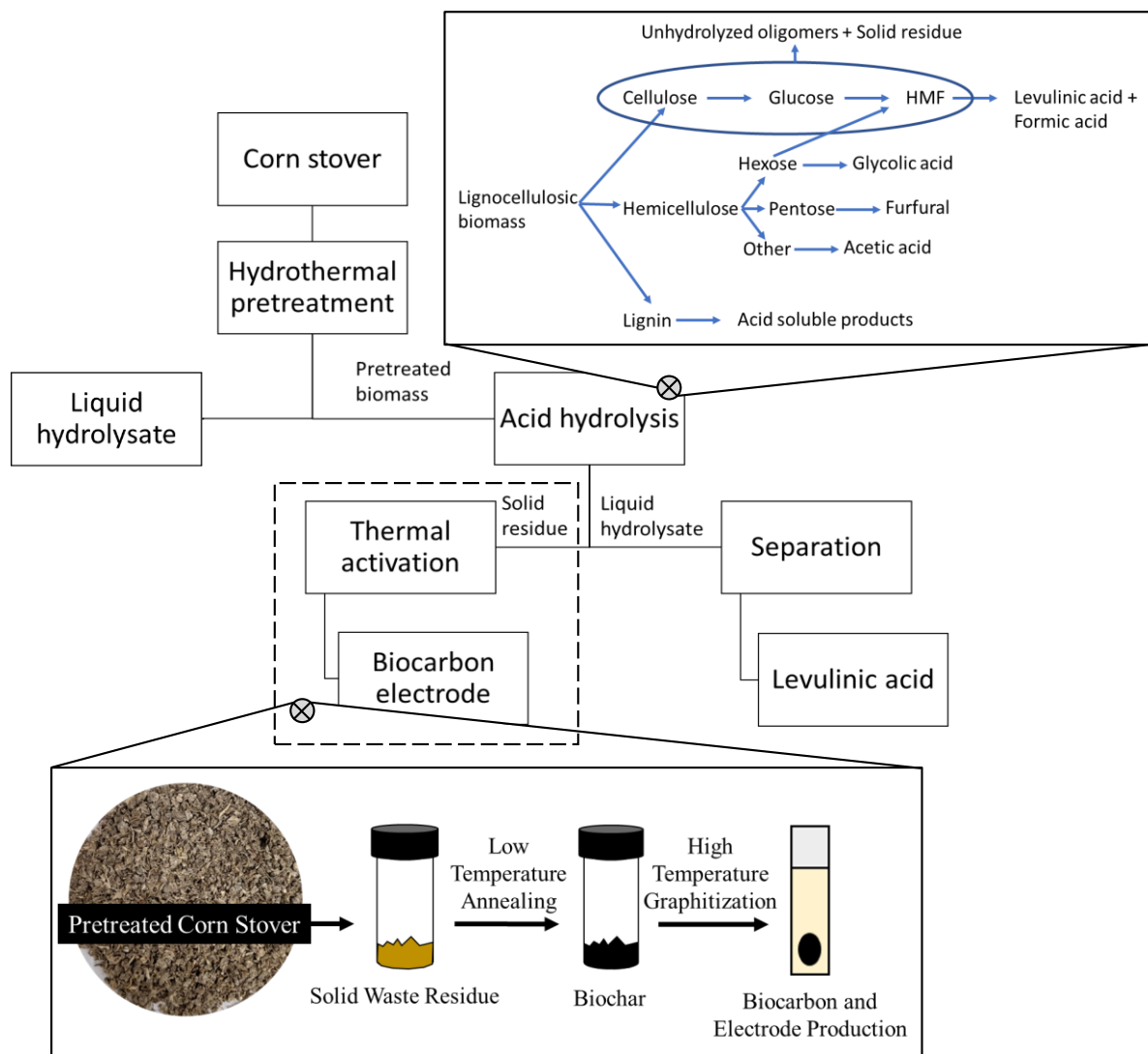


Figure 2.1. Proposed conversion scheme for corn stover to levulinic acid and biocarbon electrode material with detailed process insets.

2.3.1 Analysis of biocarbon produced from solid residue

A facile two-step thermal activation processes was found to increase sp^2 bonding, porosity and crystallinity, which in turn, increases specific capacitance, rate capabilities, and ion transport. Furthermore, materials with high hybridization, conductivity, ion transport, porosity, and surface area are desirable for supercapacitor applications. Before activation, the solid residue was cleaned via an acid washing process to remove any impurities, including metal contaminants and other

inorganic compounds. The low temperature step of the activation process is thought to remove excess volatile compounds, which was expected to enable the cleaving of functional groups at higher temperatures and therefore enhance the pore structure characteristics of the biocarbon. Additionally, the improved high temperature cleaving promotes graphitization while helping to generate interconnected pore networks for superior ion transport.^[20] The high temperature only process produced solid residue-P1 and the low temperature annealing coupled with high temperature graphitization produced solid residue-P2 biocarbon with yields of 43 and 41 wt%, respectively.

SEM images were collected after thermal activation to visually observe the pore and topological characteristics of the biocarbon, such as particle size and porosity. Both solid residue-P1 and solid residue-P2 exhibited porous structures and globular nanoparticle topography. However, solid residue-P2 appears to contain a more ordered edge characteristic of a higher degree of graphitization.

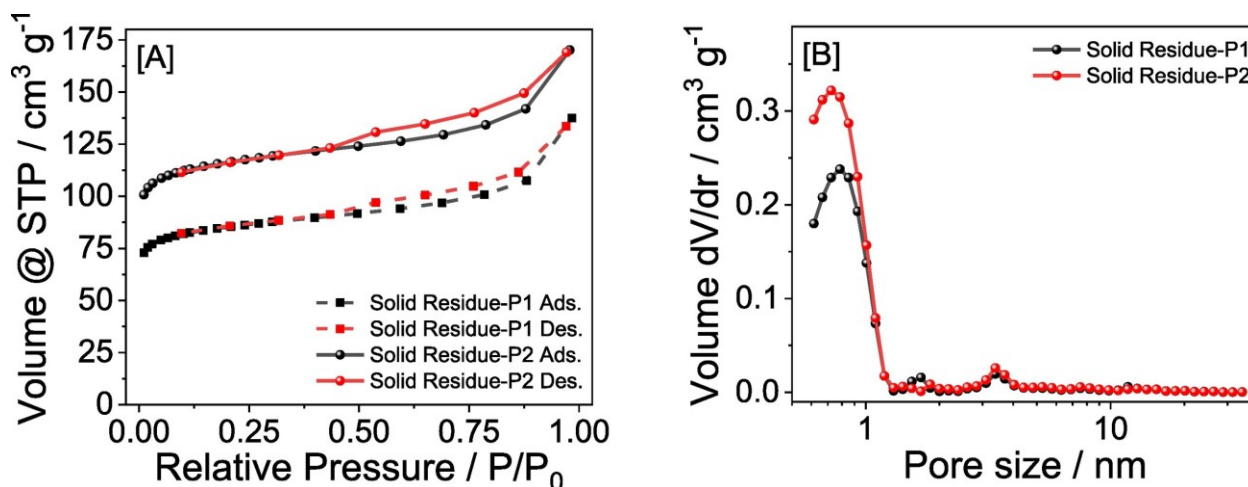


Figure 2.2. [A] Hysteresis loop of solid residue-P1 and solid residue-P2, and [B] pore size distribution of solid residue-P1 and solid residue-P2 biocarbons.

To gain a better understanding of the pore structures observed with the SEM images, a nitrogen adsorption/desorption analysis was conducted to determine differences in surface area and porosity characteristics between the two processes. The two-step process material (solid residue-P2) resulted in a hysteresis loop where a rise in low relative pressure (P/P_0) ratios indicates the presence of micropore structures (Fig. 2.2A) and mesopores are suggested at higher P/P_0 ratios, which is confirmed by the pore size distribution (Fig. 2.2B). The pore size distribution also shows that both processes produce materials with pore widths less than 1.0 nm, which indicates a predominately microporous structure. The solid residue-P2 material was found to have a S_{BET} of $466 \text{ m}^2 \text{ g}^{-1}$ and pore volume of $0.24 \text{ cm}^3 \text{ g}^{-1}$. These results fared better than solid residue-P1 which obtained an S_{BET} of $327 \text{ m}^2 \text{ g}^{-1}$ and pore volume of $0.19 \text{ cm}^3 \text{ g}^{-1}$. Therefore, the inclusion of a simple low temperature annealing step increased the S_{BET} and pore volume by 30% and 20%, respectively.

Table 2.1. Summary of conditions and results for solid residue-P1 and solid residue-P2.

Material	Method °C	Specific Capacitance, CV F g^{-1}	Specific Capacitance, CD F g^{-1}	S_{BET} $\text{m}^2 \text{ g}^{-1}$	Pore Volume $\text{cm}^3 \text{ g}^{-1}$	Yield wt.%
Solid residue-P1	1-Step: 850 (3 h)	77	58	327	0.19	43
Solid residue-P2	2-Step: 375 (2 h), 850 (3 h)	120	116	466	0.24	41

2.3.2 Electrochemical Performance

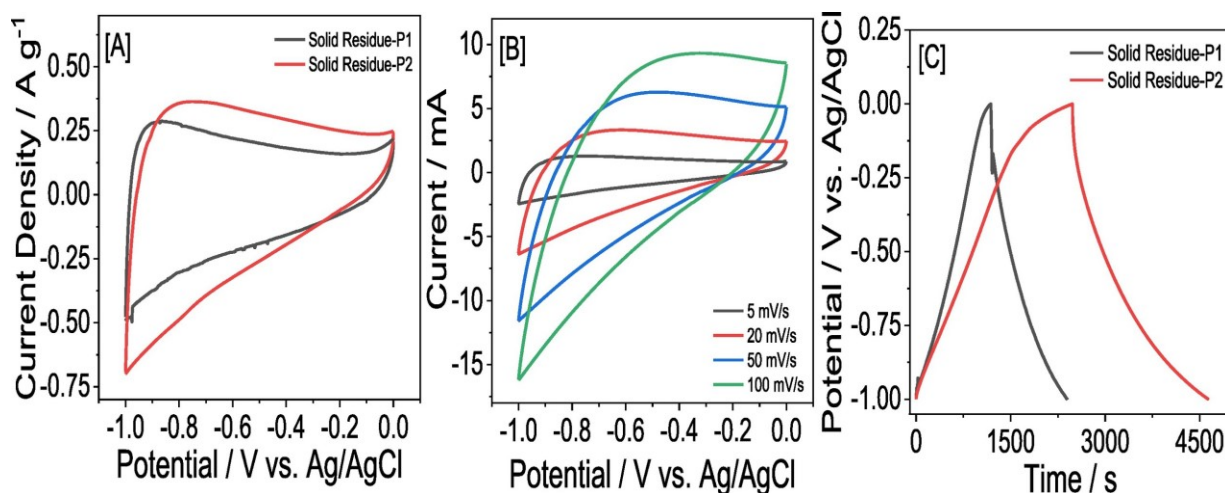


Figure 2.3. [A] CV curves of solid residue-P1 and solid residue-P2 at 5 mV s⁻¹, [B] CV curves of solid residue-P2 at various scan rates between 5 and 100 mV s⁻¹, [C] CD curves of solid residue-P1 and solid residue-P2 at 0.05 Ag⁻¹.

Electrochemical performance was conducted using CV and CD methods via a 3-electrode system in 2 M KOH. The CV method was based off of amps reported at various scan rates, where CD method was based off of time elapsed. The one-step samples were utilized as a control material to validate the necessity of a low temperature activation step. Both samples were studied via the CV method at scan rates of 5, 20, 50, and 100 mV s⁻¹ in a potential window from 0.0 to 1.0 V vs Ag/AgCl. Smooth sweeps with no reversible /irreversible redox reaction peaks were reported for the cyclic voltammograms, indicative of an electric double-layer capacitor (EDLCs). For supercapacitors, this characteristic is typically observed at lower scan rates and classified as an ideal box shape. Fig. 2.3A demonstrates the higher capacitance of solid residue-P2 compared to solid residue-P1 at 5 mV s⁻¹, indicated by the larger integrated area determined by analyzing the plotted CV data. The solid residue-P2 achieved a specific capacitance of 120 F g⁻¹, while only 77 F g⁻¹ was obtained from solid residue-P1 at 5 mV s⁻¹. An ideal box shape was preserved for

solid residue-P2 at higher scan rates (Fig. 2.3B), with specific capacitances of 78, 54, and 36 F g⁻¹ for scan rates 20, 50, and 100, respectively. Concurrently, the CD method, performed at a current density of 0.05 Ag⁻¹ (Fig. 2.3C), demonstrated ideal ion absorption/desorption characteristics, confirmed by smooth and symmetric segments. Solid residue-P2 achieved twice the capacitance at 116 F g⁻¹ over solid residue-P1. The CV and CD methods were presented as a preliminary study to assess the viability of solid residue as electrode materials. The physical and electrochemical properties of the biocarbon samples are summarized in Table 2.1, where the increased physical and electrochemical characteristics of solid residue-P2 were likely to be attributed to the lower temperature activation step, promoting graphitization at higher temperatures and the interconnection of pores, facilitating ion transport.^[20] The literature values for corn starch exhibited a surface area of 1167 m² g⁻¹, pore volume of 1.80 cm³ g⁻¹, and max capacitance of 162 F g⁻¹.^[65] In comparison, the solid residue-P2 derived biocarbon had a S_{BET} of 466 m² g⁻¹, pore volume of 0.24 cm³ g⁻¹, and a specific capacitance of 120 F g⁻¹. Although the corn starch biocarbon from literature was found to have slightly enhanced properties, the activation process to produce the solid residue-P2 samples were competitive. The activation process for the solid residue-based materials has the potential to be further optimized through the use of CO₂, KOH, or metal catalysts during thermal treatment, where the capacitance may exceed 200 F g⁻¹.^[70] Therefore, future solid residue derived biocarbon remains viable for energy storage applications.

2.4 Conclusions

Overall, an integrated biorefinery process was successfully demonstrated, whereby raw corn stover was fractionated using 0.45 wt% K₂CO₃ at 190 °C, extracting 76% of lignin and 85% of xylan while preserving 83% of glucan. During acid hydrolysis, 2 wt% H₂SO₄ produced the highest levulinic acid yields while all other H₂SO₄ concentrations resulted in higher solid residue yields.

A low-cost, sustainable two-step facile thermal annealing and activation process produced biocarbon (solid residue-P2) with a specific capacitance of 120 F g^{-1} , S_{BET} of $466 \text{ m}^2 \text{ g}^{-1}$, and pore volume of $0.24 \text{ cm}^3 \text{ g}^{-1}$, comparable to biocarbon from corn starch.

Chapter III. Supercapacitor Performance of Corn Stover-Derived Biocarbon Produced from the Solid Co-products of a Hydrothermal Liquefaction Process

Adapted From:

Katelyn M. Shell, Dylan D. Rodene, Vinod Amar, Anuj Thakkar, Bharathkiran Maddipudi, Sandeep Kumar, Rajesh Shende, and Ram B. Gupta. *Bioresource Technology Reports* 13 (2021): 100625.

Biocarbon is obtained by the graphitization of biochar, a co-product in a novel integrated biorefinery concept that simultaneously produces C1–C3 acids, phenol, bio-oil, and biochar. The unhydrolyzed solids from the IBR are hydrothermally liquefied to obtain bio-oil and biochar coproducts. The biochar samples obtained from the HTL of UHS at different process conditions were low temperature thermally treated to remove volatile compounds, followed by a facile high temperature graphitization to biocarbon. Physical analyses showed the degree of graphitization directly effects pore volume. The UHS-SDC9 biochar produced at 275 °C, 40 psig, and 1 h of hydrothermal treatment exhibited the biocarbon with the best electrochemical performance having specific capacitance of 242 F g⁻¹ at a scan rate of 5 mV s⁻¹ and an energy density of 9.9 W h kg⁻¹. Statistical analysis was performed to correlate the IBR processing parameters to physical and electrochemical characteristics of the biocarbon obtained.

3.1 Introduction

The demand for alternative and sustainable materials in energy storage devices, such as batteries and supercapacitors, is rapidly increasing. Production of these devices is dependent on the availability of feedstock materials and suitable methods.^[5] Unfortunately current commercial supercapacitors and batteries utilize carbons from coking of fossil fuels, which is neither renewable nor sustainable.^[6] Biomass is an immensely abundant, low cost, and environmentally-benign source for biocarbon suitable for supercapacitor electrodes.^[17] Recent studies conducted on corn stover, as a biomass source, have reported an extraction of both biofuels and biochar as part of a biorefinery concept.^[66] In this work we demonstrate an integrated process where multiple product streams and derivatives are utilized to generate value-added products to lower overall costs. Specifically, agricultural waste, as a source of biomass, can be used to renewably produce (1) bio-oil, (2) C1–C3 acids, (3) phenols, and (4) biocarbon suitable for supercapacitor applications. The

focus for the IBR concept is on the overall optimization of various products, where here, emphasis is on the production of suitable biocarbon for supercapacitors.

An integrated biorefinery concept is a novel and economical methodology for the co-generation of multiple products from one feedstock. This form of process intensification allows for the reduction of waste and overall costs. The global market for graphitic carbons in batteries and supercapacitors is expected to exceed \$99 billion by 2025, with a demand of more than 0.6 million tons per year.^{[71],[72]} Currently, graphitic carbon, from petroleum coking processes, sells for about \$20,000 ton⁻¹, therefore, solid residues from biomass feedstocks are foreseen to become economically competitive.^[73] Additionally, other co-produced materials further add to the significance and profitability of the IBR concept. Other co-products from an IBR are C1–C3 acids. These are commonly known as short chain fatty acids with fewer than six carbon atoms, such as formic acid, acetic acid, propionic acid, and lactic acid. Among these, lactic acid produced from hydrothermal liquefaction process is of high commercial interest for producing polylactide biodegradable polymer. To commercially obtain such value-added products along with biofuels, biochar, phenols, and biomass resources such as corn stover can be processed hydrothermally via IBR. This provides a holistic approach, offering multiple opportunities to integrate processing of different waste streams to generate value-added products that can help offset the biofuel cost.

Supercapacitors are increasingly being used for commercial applications, such as smart grid systems and hybrid electric vehicles, where the demand is projected to rise significantly, owing to excellent cyclability, great stability and a good power density.^[74] However, current supercapacitor materials have lower energy densities (0.1–10 W h kg⁻¹) than Li-ion batteries (10–100 W h kg⁻¹).^[75] To increase the energy density of supercapacitors, knowledge of the energy storage mechanism is necessary. Carbon-based materials are specifically utilized in

electrochemical double layer capacitors (EDLCs), one type of supercapacitor. For EDLCs, energy is stored as ions on the surface and pores of the electrode material via an applied voltage, electrostatically creating a charge separation.^[75] When an increase in viable pores are present, the material can adsorb more ions, thus increasing capacitance. Once the applied voltage is removed, ions desorb from the electrode surface and effectively discharges the supercapacitor. Hence, an increase in conductivity, porosity, and surface area can increase specific capacitance.^[75] However, an increase in porosity does not directly correlate to higher specific capacitances. Typically, the pores must be two-fold larger than electrolyte ions, which have a hydrodynamic radius on the sub-nanometer scale.^[12] For example, most pores below 0.8 nm are not viable for ionic storage.^[13] Pores are classified as microporous (< 2 nm), mesoporous (2–50 nm), and macroporous (> 50 nm), where the lower end of the mesoporous range (0.8–3 nm) is more ideal for proper ion mobility and adsorption.^[14] Therefore, desired pore structures are being controlled via physical and chemical routes to improve the energy densities of biocarbon-based materials for supercapacitors electrode.^[16]

Different sources of biomass can offer unique characteristics corresponding to their biochemical composition. Corn stover (i.e. stems, stalks, leaves, etc.) has received increased attention as a biomass source for multiple processes due to a high content of lignin, cellulose and hemicellulose, as well as its prevalence as a highly abundant harvested waste.^[75] These compounds are carbon rich molecules suitable for biocarbon production, however the complex chemical composition of lignocellulosic biomass makes pretreatment, through enzymatic hydrolysis, necessary for biomass conversion.^[76] Enzymatic hydrolysis separates lignin and hemicellulose from biomass and alters the physical parameters of the unhydrolyzed solids observed after formation of biocarbon, such as

crystallinity, pore size, surface area and the degree of polymerization.^{[59],[77],[78]} More information on enzymatic hydrolysis with reaction scheme is in the Appendix A6 (Fig. A6.1).

To obtain biochar, thermochemical conversion, among other biomass processing techniques such as biochemical and mechanical/physical routes, are utilized to cleave chemical bonds within the biomass and form a high yield/quality product.^[79] Hydrothermal liquefaction (HTL) is a preferred thermochemical conversion technique that facilitates thermal depolymerization of corn stover.^{[80]–}^[82] It is also ideal for biomass feedstocks containing a high moisture content to convert biomass into value-added products.^[83] In addition, the carbon yield of the biochar obtained from an HTL process is higher when compared to pyrolysis and gasification. Due to the moderate operating conditions and direct conversion of biomass, the HTL process has an exceptional economic viability to produce biochar.^[84] More information pertaining to prior works on HTL utilizing various biomass feedstocks can be viewed in Table A6.1.

Biochar can be activated through thermal and/or thermochemical routes to produce biocarbon.^[85] Activation treatments are necessary to control important material characteristics for supercapacitor applications. Similar to pretreatment, pore size, surface area, crystallinity, and the degree of hybridization are significantly affected by activation processes. Thermal treatment increases graphitization, thus increasing conductivity, and creates graphitic structures that allow for interconnected pore networks, leading to greater ion mobility within the framework.^{[20],[21]} Thermochemical routes often use highly corrosive reagents and multiple process steps which negatively affect recyclability of waste streams and scale-up.^[86] Therefore, a thermal activation process was chosen to form the desirable physical characteristics of the biocarbon.

For a rational scale-up and production of biocarbon for supercapacitors, it is imperative to study the performance of solid residues (biochar) obtained from the lignin-rich biomass converted at

different operating conditions of HTL processes. In this work, corn stover biomass underwent enzymatic hydrolysis prior to HTL processing. The biocarbon, obtained from biochar at various HTL processing conditions, was used to identify HTL processing conditions that lead to higher specific capacitance values. Furthermore, to form the biocarbon samples (UHS-SDC#s), a low cost, facile one-step carbonization process of the biochar samples was performed. Nano-characterization techniques were employed to examine and quantify the structural and chemical attributes of the biocarbon samples. Lastly, statistical analyses were performed to determine the weighted impacts of HTL parameters on biocarbon performance. These insights, coupled with the electrochemical performance are advantageous in determining suitable HTL process parameters for biocarbon production from an IBR targeting supercapacitor applications, are reported herein for the first time.

3.2 Experimental

3.2.1 Materials

Commercially available unhydrolyzed solids (UHS), from an ammonia fiber expansion process (AFEX) followed by enzymatic hydrolysis of corn stover, were obtained from Glydia Biotech (TX, USA). Hydrochloric acid (HCl, 1 M) and ethanol (C₂H₅OH, 95 wt.%) were purchased as analytical grade from Fisher Scientific (MA, USA). Polytetrafluoroethylene (PTFE, 60 wt.% dispersed in water) and potassium hydroxide (KOH, 90 wt.%) were purchased from Sigma-Aldrich (MO, USA). Carbon black (Super P conductive, 99+ wt.%) was purchased from Alfa Aesar (MA, USA). Ultra-high purity (grade 5.0) argon was purchased from Airgas (PA, USA). Milli-Q (18.2 MΩ) water was obtained from an on-demand Barnstat filtration system. Nickel foam substrates were

purchased from MTI Corporation (CA, USA). Henkel Loctite Hysol 9462 epoxy adhesive was purchased from Ellsworth Adhesives (WI, USA).

3.2.1 Production of Biochar via Hydrothermal Liquefaction

The HTL process was used to convert UHS to biochar in a Parr reactor at the South Dakota School of Mines and Technology (SDSMT) under various processing conditions (Table 3.1). As-received UHS were used as a lignin-rich biomass source for the HTL reaction at high temperature (200–300 °C) and high-pressure (0–150 psig) in a non-catalytic environment. Operational and technical details of the Parr reactor are given by Jaswal et al. (2019).^[54] During the HTL, effects of operating conditions such as temperature, initial reactor purge pressure, reaction time and UHS to solvent ratios were investigated. Throughout the studies, the stir rate was fixed to 1300 rpm and the initial N₂ purging was performed for 20 min. All experiments were conducted in 150 mL of deionized water. The contents were cooled using an internal recirculating loop within the reaction vessel for all experiments. Slurries were recovered through a series of filtration and extraction steps where the biocrude, bio-oil and solid-residue (biochar) were separated at individual steps. Thus, obtained solid residue was washed to attain a neutral pH and dried in a conventional oven at 65 °C. Following this step, thermal annealing of solid residues was carried out in a horizontal tubular furnace at 400 °C with a continuous flow of N₂ at flow rate of 85 SCCM for 2 h to generate the biochar. The governing equations for the extraction of both biofuels and biochar yields during hydrothermal liquefaction (HTL) of biomass are given in our recent publication on HTL.^[87]

Table 3.1. Hydrothermal liquefaction (HTL) parameters for received biochar

Sample Name*	Parameters			
	Biomass to Solvent	Temperature	Initial Pressure	Reaction Time
	Mass Ratio / g:g	/ °C	/ psig	/ h
UHS-SDC1	1:10	250	40	1
UHS-SDC2	1:10	275	40	1
UHS-SDC3	1:10	300	40	1
UHS-SDC4	1:10	275	0	1
UHS-SDC5	1:10	275	100	1
UHS-SDC6	1:10	275	150	1
UHS-SDC7	1:10	275	40	0.5
UHS-SDC8	1:10	275	40	2
UHS-SDC9	1:30	275	40	1
UHS-SDC10	1:6	275	40	1

*Naming convention refers to original material (UHS), institution of preparation (SDSMT) at and biocarbon sample number (UHS-SDC#)

3.2.2 Facile one-step carbonization process

Biocarbon samples were prepared through a facile thermal activation process without the use of any chemical reagents or catalysts. For a typical synthesis, UHS biochar underwent a standard acid washing process, whereby, 1.0 M HCl was added to ca. 1.0 g of biochar followed by sonication for 10 min. The resulting suspension was centrifuged at 3000 RPM for 4 min, and decanted. The acid washing process was repeated twice to ensure removal of any metal/inorganic contaminants. The biochar was further washed using double distilled water (18.2 M Ω) and then dried in a vacuum oven (60 °C, -60 kPa) for 16 h. Once dried, the biochars were placed in a porcelain boat and carbonized in a Carbolite tube furnace at 850 °C under Ar flow for 3 h (ramp rate of 5 °C min⁻¹),

then left to cool naturally. Carbonized products (biocarbons) were recovered for electrode preparation.

3.2.3 Physical characterization

Surface morphology was examined using a Hitachi Model FE-SEM Su-70 scanning electron microscope (SEM) operating at 20 keV with an in-situ EDAX detector. The samples were prepared on a flat aluminum specimen holder with double-sided carbon tape (Ted Pella, Inc.). The surface areas (S_{BET}) and pore size distributions were determined by nitrogen adsorption-desorption measurements using the Brunauer–Emmett–Teller (BET) method with a Quantichrome NOVA 2400e analyzer and software. Prior to the adsorption measurements, all samples were degassed under vacuum at 150 °C for 15 h. Attenuated total reflectance Fourier-transform infrared (ATR-FTIR) spectroscopy was carried out using a Thermo Fisher Scientific Nicolet iS10 infrared spectrometer with a total of 8 scans per sample. Raman spectroscopy was performed on a LabRam HR Evolution Raman spectrometer (532 nm, 25% power) with sampling range of 800 to 2100 cm^{-1} . Crystallinity of the selected biocarbon samples was examined by X-ray diffraction (XRD) on select samples and was performed using a Rigaku MiniFlex II X-ray diffractometer with a Cu $K\alpha$ radiation source. All XRD spectra were collected at a scan speed of 1.0° min^{-1} , sampling width of 0.01°, a voltage of 30 kV at 15 mA, and wavelength of 1.54 Å.

3.2.4 Electrochemical measurements

All electrochemical measurements were performed on an electrochemical workstation (CH Instruments, CHI 660E). To prepare working electrodes, mixtures containing biocarbon, Super P, and PTFE were prepared with a mass ratio of 8:1:1, respectively. A limited amount of water (18.2 M Ω) was added to the mixtures to obtain viscous slurries. The slurries were evenly coated onto reduced nickel foam substrates (ca. 1.0 × 3.0 cm) and dried overnight at 50 °C in a vacuum

oven. Prior, the nickel foam substrates were cleaned by reducing surface oxides in 1 M HCl, followed by H₂O (18.2 MΩ), and ethanol washes, while sonicating for 10 min during each step. The coated substrates were templated and insulated using a chemical resistant epoxy to form the working electrodes. The active mass for each electrode was determined by ratioing the geometric areas before and after templating, where digital images were analyzed by ImageJ software.

A traditional three electrode (3-cell) setup was utilized for cyclic voltammetry (CV), galvanostatic charge-discharge (CD) whereby, a platinum (Pt) wire and an Ag/AgCl (sat. KCl) were used as the counter and reference electrodes, respectively. All measurements were performed in 2 M KOH. Specific capacitances were calculated following Equations. (3.1), (3.2) for CV and CD, respectively.

$$C_{CV} = \frac{\int_{V_1}^{V_2} I dV}{m v \Delta V} \quad (3.1)$$

$$C_{CD} = \frac{I t}{m \Delta V} \quad (3.2)$$

where, V_1 and V_2 are the endpoints to the potential window in volts, I is the recorded current in amps, m is the active mass in grams, v is the scan rate in mV s⁻¹, ΔV is the difference between V_1 and V_2 , and t is the time to complete one charging segment in s.

A two electrode (2-cell) setup was utilized to obtain energy densities of each material. Here, two identical electrodes acted as the working and reference/counter electrodes, respectively, with a semipermeable membrane between the electrodes. Specific capacitance of the 2-cell supercapacitor and subsequent energy and power densities were calculated following Eqs. (3.3), (3.4), (3.5), respectively.

$$C_{2cell} = \frac{I t}{m \Delta V} \quad (3.3)$$

$$E = \frac{C_{2cell} \Delta V^2}{2 * 3.6} \quad (3.4)$$

$$P = \frac{E}{t} \quad (3.5)$$

3.2.5 Statistical analysis

All statistical analyses were performed using JMP Pro 15 software to give context for electrochemical trends and biocarbon characteristics. A standard least squares regression was performed for specific capacitance ($F g^{-1}$) as a function of the HTL processing parameters. The resulting design space was constructed for the HTL parameters, including the polynomial terms to the second degree. The prediction profiler tools and validity of the fits were associated and based upon outputted p-values and correlation coefficients (R^2).

3.3 Results and Discussion

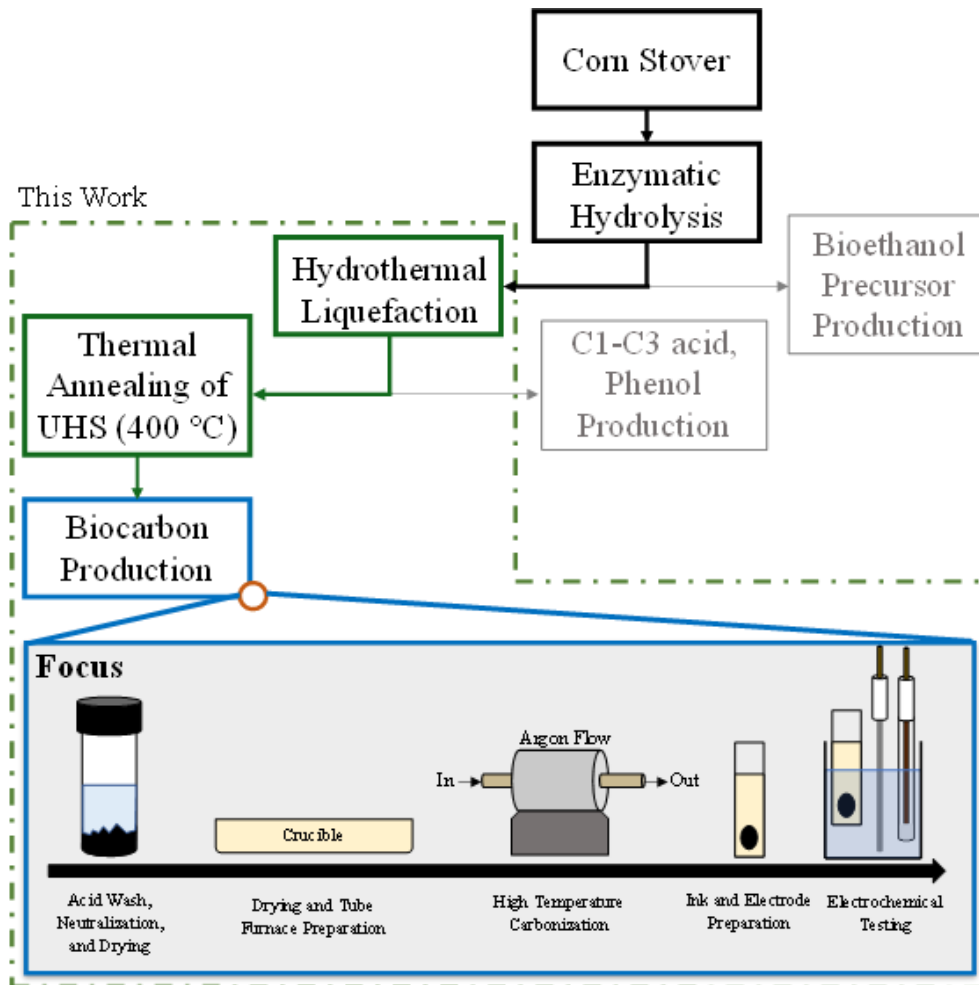


Figure 3.1. Schematic of simplified integrated biorefinery processes with emphasis on biocarbon synthesis, supercapacitor preparation, and electrochemical testing.

3.3.1 Physical characterizations

An integrated biorefinery (IBR) concept is shown to have been successful in the conversion of biomass into multiple value-added products. Focus was on improving the biochar quality, for biocarbon production, by varying the reaction temperature, pressure, biomass loading and time following a design of experiments approach (Table 3.1). The lignin rich biomass conversion

process resulted in C1–C3 acids, phenols, and biochar, where biochar exhibited a yield of ~29 wt%, with respect to HTL loading. A low temperature thermal annealing step was performed at 400 °C for 2 h (in the presence of N₂) to remove any organic volatile impurities present (-C=O, -COOH, -OH) in the biochar. The presence of excess volatile compounds in the biochar was proven to limit the cleaving of functional groups at higher temperatures, which prevents optimal pore structure formation. Biocarbon was produced from the UHS derived biochar via a facile high temperature one-step thermal activation. The simplified IBR and activation scheme used to produce biocarbon supercapacitor electrodes from UHS-biochar are illustrated in Fig. 3.1. The facile high temperature activation step was performed to aid in enhancing specific capacitance, rate capabilities, and ion transport of the supercapacitor materials. Furthermore, thermal activation increases the degree of hybridization to aid in sp² bonding, which positively influences the crystallinity and ohmic conductivity of the biocarbon.

The mechanism for graphitization was first described by Murty et al. (1969) whereby graphitization is denoted as a growth process, not nucleation.^[88] Energy is supplied in the form of heat (i.e. 850 °C or higher) to overcome the activation energy of graphitization (~230 kcal mol⁻¹). This theory states that a vacancy mechanism or point-defect mechanism is responsible for the formation of graphitized carbons. Here, there is enough energy for bonds to break and rearrange, filling defects or holes within the carbon framework.^[88] This mechanism was proposed utilizing data from experiments on petroleum cokes, however the mechanism can be applied to biomass derived carbons as well since the formation of graphite still occurs and is visible in XRD and Raman spectra, though not to the extent of petroleum coke derived graphite.

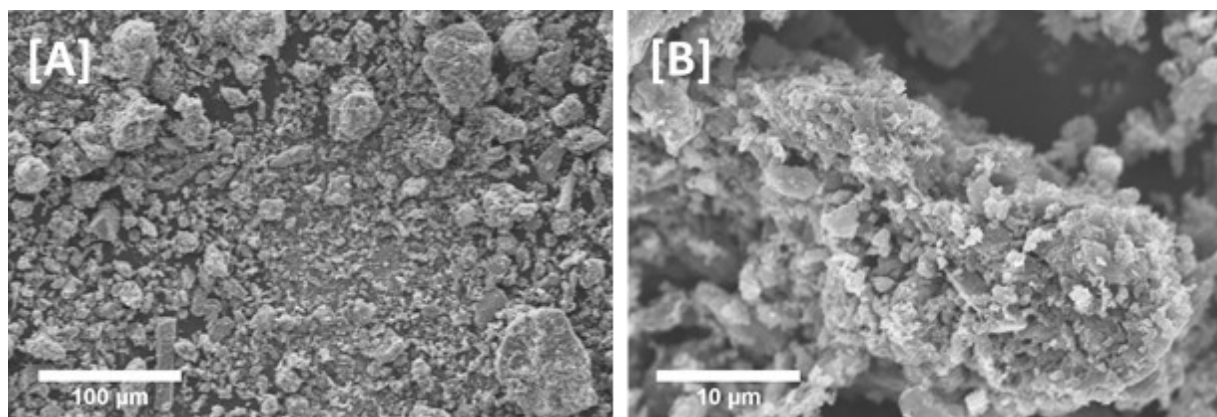


Figure 3.2. SEM images taken at two magnifications to depict [A] the distribution of particle sizes and [B] surface morphologies of UHS-SDC9 biocarbon.

The surface pore structures were observed after the high temperature activation. The SEM images show a wide distribution of particle sizes (Fig. 3.2A) and surface topographies (Fig. 3.2B) for the activated UHS-SDC9 biocarbon. Nitrogen adsorption-desorption measurements were conducted on select biocarbons from each parameter to examine pore size distributions and determine pore structures. For UHS-SDC9, the rise at low P/P_0 indicates the presence of micropores on the hysteresis plot (Fig. 3.3A) and the hysteresis loop at higher P/P_0 suggests the presence of mesopores. The reversible isotherm contains Type II features representing unrestricted monolayer and multilayer adsorption characteristics of macroporous adsorbent. Similarly, from the same plot, pore structures are defined as H4 signifying slit-like pores and irregular cavities of varying sizes. Total pore volume for all of the materials were between 0.03 and $0.12 \text{ cm}^3 \text{ g}^{-1}$. The pore size distribution plot (Fig. 3.3B) illustrates the comparison of UHS-SDC2 (the control) and UHS-SDC9. Peaks from the pore size distribution can be seen at ~ 7 nm and ~ 9 nm for UHS-SDC2 (control) and ~ 6 nm, 20 nm, and 60 nm for UHS-SDC9 (Fig. 3.3B). UHS-SDC9 demonstrated the largest differential pore volume at the lowest pore diameter, as well as hierarchical porous structures. Optimal pore size has been described to be between 0.8 and 3 nm with pore structures

that allow for rapid adsorption and desorption of ions. It is important to note that each pore type (micro-, meso-, macropores) offers its own benefit. Macropores allow rapid wettability and micropores significantly increase capacitance at low scan rates or current densities, therefore the presence of both are desirable.

The S_{BET} of HTL biochar is typically low ($1\text{--}5\text{ m}^2\text{ g}^{-1}$), however samples produced from these experiments were greater than $10\text{ m}^2\text{ g}^{-1}$. S_{BET} areas of the select biocarbon samples were 272, 240, 80, 211, and $215\text{ m}^2\text{ g}^{-1}$ for UHS-SDC1, UHS-SDC2, UHS-SDC4, UHS-SDC8 and UHS-SDC9, respectively (Table 3.2). Lower surface areas are likely attributed to the breakdown of large complex carbonaceous compounds during the HTL processing. Differences in electrochemical performance of the complex carbonaceous compounds are attributed to the varying degrees of graphitization during processing. In general, as graphitization (and therefore crystallinity) increases, the specific surface area (SSA) decreases for thermally activated biocarbons.^[89]

Table 3.2 S_{BET} parameters for selected samples calculated from N_2 adsorption-desorption isotherms.

Sample	$S_{\text{BET}}\text{ SSA} / \text{m}^2\text{ g}^{-1}$		Pore Volume / $\text{cm}^3\text{ g}^{-1}$
	S_{char}	S_{meso}	V_{meso}
UHS-SDC1	16.1	272	0.12
UHS-SDC2	36.2	240	0.09
UHS-SDC4	30.0	80	0.03
UHS-SDC8	25.4	211	0.08
UHS-SDC9	10.6	215	0.12

The high temperature carbonization led to the cleaving of C–OH and C=O bonds to form more ordered –C–C–, –C=C–, and –C–O–C– chemical structures.^{[90],[91]} The formation of these structures leads to a more conductive, graphitized, and crystalline material with interconnected pore networks, ideal for energy storage electrode materials. The ATR-FTIR analysis further supports the theory of bond cleaving and graphitization, where the newly formed chemical

structures exhibited a broad peak over the fingerprint region at $\sim 1100\text{ cm}^{-1}$ for all samples (Appendix A6, Fig. A6.2). The broad peak at $\sim 1100\text{ cm}^{-1}$ denotes C–O stretching associated with esters and C–C bonding. A small peak at $\sim 1580\text{ cm}^{-1}$ correlates to C=C bonding, characteristic of thermally treated samples.^[92] The absence of any other peaks indicates that all functional ketone or alcohol groups have been eliminated, further resulting in a primarily carbonaceous structure.

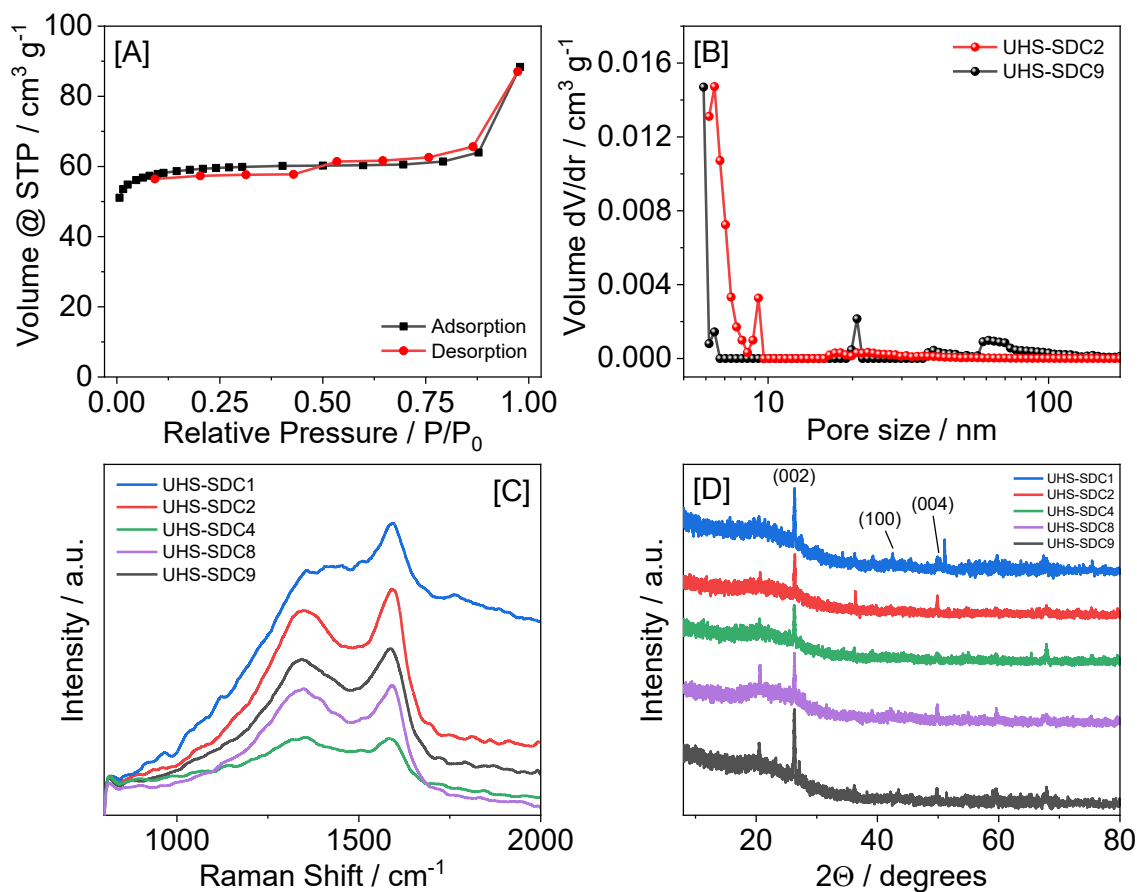


Figure 3.3. Physical characterization of biocarbons: [A] BET hysteresis plot of UHS-SDC9, [B] pore size distribution of UHS-SDC2 (control) and UHS-SDC9, [C] Raman spectra, and [D] XRD spectra of UHS-SDC1, UHS-SDC2, UHS-SDC4, UHS-SDC8, and UHS-SDC9.

The Raman spectra contained two characteristic peaks at 1345 and 1590 cm^{-1} that correspond to the D and G bands, respectively. In order to determine the degrees of graphitization, a ratio of the

D and G band intensities are taken ($I_D I_G^{-1}$). The UHS-SDC1, UHS-SDC2, UHS-SDC4, UHS-SDC8, and UHS-SDC9 biocarbons gave ratios of 1.17, 1.11, 0.98, 1.03, and 1.07, respectively. Calculated ratios for all of the samples are listed in the Appendix (Appendix A6, Table A6.1), where UHS-SDC4 exhibited the highest degree of graphitization. Degree of graphitization is a physio characteristic parameter used to assess disorder or defects within the biocarbon. Lower $I_D:I_G$ ratios indicate less disorder and a more graphitized carbonaceous material. The D band ($\sim 1340 \text{ cm}^{-1}$) is indicative of the disorder aspect of the biocarbon while the G band ($\sim 1590 \text{ cm}^{-1}$) corresponds to sp^2 bonded carbon.^[93] A shift towards higher G band intensity means more graphite crystals are present. Graphitic carbons are more desirable over amorphous due to higher conductive properties.^[94] In supercapacitors, higher conductivity leads to higher capacitance due to lower resistance losses.

UHS-SDC1 contained two super positioned peaks, one broad peak spanning from $2\Theta=20\text{--}30^\circ$ and one sharp peak at $2\Theta=26^\circ$ with another minute peak downrange at $2\Theta=43^\circ$. The broad peak from $2\Theta=20\text{--}30^\circ$ and the peak at $2\Theta=43^\circ$ correspond to reflections of the graphite basal (002) and perpendicular (100) planes, typically associated with disordered graphitic carbon.^[22] The sharp peak overlapping the broad peak at $2\Theta=26^\circ$ suggests the formation of highly ordered graphitic carbon, indicating the post processed material contains some mixture of graphitic and amorphous carbon. EDAX analysis reported carbon and oxygen at $\sim 73 \text{ at.}\%$ and $\sim 20 \text{ at.}\%$, with low amounts of silicon ($\sim 7 \text{ at.}\%$), respectively (Appendix A6, Fig. A6.1). Silicon would result in a peak at $2\Theta=26^\circ$ as well, however the increased $2\Theta=26^\circ$ peak intensity in biocarbon UHS-SDC9 is indicative of larger graphitic carbon crystallite sizes. The control (UHS-SDC2) and UHS-SDC4 contained the same general super positioned peaks as UHS-SDC1, at $2\Theta=20\text{--}30^\circ$ and $2\Theta=26^\circ$, but appear to have peaks at $2\Theta=38^\circ$ and $2\Theta=51^\circ$, with the latter corresponding to the 004 graphitic

peak. UHS-SDC8 contains the same broad and sharp peaks at $2\Theta=20-30^\circ$ and $2\Theta=26^\circ$, respectively, with a sharp peak appearing at $2\theta = 21^\circ$ and a minute peak at $2\Theta=51^\circ$ (004), indicating the formation of a more crystalline structure. UHS-SDC9 material maintains the peaks seen in the UHS-SDC8 spectra, however, the peak intensity at $2\Theta=26^\circ$ increased, suggesting a slightly enhanced graphitic structure. Overall, when compared to purely crystalline graphite, these results propose the formation of turbostratic crystallites.^[95] Highly ordered graphitic biocarbons are achieved through activation temperatures in excess of 1500 °C where an increase conductivity would likely be observed at the expense of pore structures and surface area, resulting in reduced ion storage. This theory was demonstrated by Yu et al. (2018) where pore structures were negatively affected due to carbon structure rearrangement at temperatures of 2400 °C.^[96] Therefore, maintaining a balance between hierarchal porous structures and graphitization is key in producing high performance biocarbon for electrochemical applications.^[22]

3.3.2 Electrochemical Characterizations

Fig. 3.4B shows cyclic voltammograms for UHS-SDC9 at 5, 20, 50, and 100 mV s^{-1} between a potential window of 0 and -1 V vs Ag/AgCl (sat.). The cyclic voltammograms exhibited no irreversible reactions, indicated by smooth lines with no peaks and demonstrated desirable electrochemical double-layer capacitance. Moreover, the CV curves maintained a rectangular appearance resulting from good adsorption and desorption of electrolyte ions permeating into the biocarbon porous structures; a characteristic of ideal capacitive behavior.^[97] Material UHS-SDC9 attained capacitances of 242, 173, 127, and 88 F g^{-1} for the respective scan rates. Top performing materials UHS-SDC1, UHS-SDC2, UHS-SDC4, UHS-SDC8, and UHS-SDC9, shown as stacked CV curves at 5 mV s^{-1} in Fig. 3.4A, which further show the desired curve characteristics resulting from optimal biocarbon post C1–C3 acids and phenol conversion. Specific capacitances for UHS-

SDC1, UHS-SDC2, UHS-SDC4 and UHS-SDC8 at 5 mV s^{-1} were 173, 154, 180, and 207 F g^{-1} , respectively. Galvanostatic charge-discharge (CD) of material UHS-SDC9, performed at current densities of 0.05, 0.1, 1, and 5 A g^{-1} , can be noted in Fig. 3.4C. The CD curves demonstrate ideal sawtooth shape with nearly symmetrical halves signifying reversable capabilities and ideal capacitive behavior. Stacked CD results of UHS-SDC9 (Fig. 3.4D) illustrate the symmetrical nature of curves at higher current densities, further indicating ideal EDLC behavior.^[97] Specific capacitances from CD for materials UHS-SDC1, UHS-SDC2, UHS-SDC4, UHS-SDC8, and UHS-SDC9 were 119, 104, 125, 160, and 190 F g^{-1} , respectively.

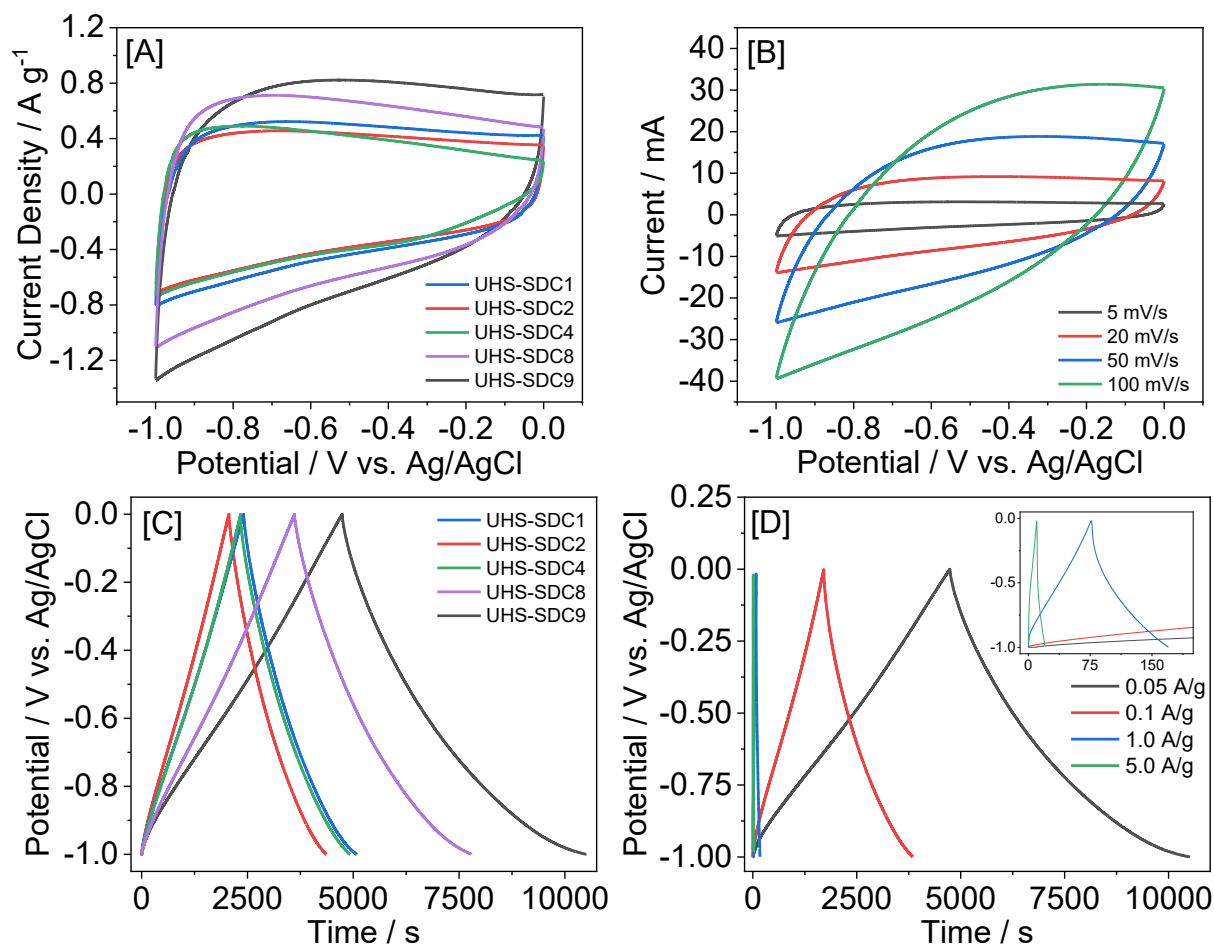


Figure 3.4. Electrochemical characterization of the biocarbons: [A] CV overlays at 5 mV s^{-1} , [B] stacked CV curves of material UHS-SDC9 from $5\text{--}100 \text{ mV s}^{-1}$, [C] CD overlays at 0.05 A g^{-1} , [D] CD stacked curves of UHS-SDC9 from $0.05\text{--}5 \text{ A g}^{-1}$.

The specific capacitance versus current density is shown in Fig. 3.5A for the best performing electrode material. A maximum specific capacitance was observed for UHS-SDC9 was 242 F g^{-1} at 0.05 A g^{-1} . At higher current densities ($1, 5 \text{ A g}^{-1}$) there is a significant reduction in specific capacitances, which is typical, due to limited ion diffusivity where fast ion mobility prevents pore penetration. This is most likely attributed to a lower penetrable surface area. The specific capacitance versus current density plot is a viable method to observe how the pore structures of a

material affect the charge storage mechanism. A linear characteristic would be observed for both a macroporous material and material without a pore structure network. Contrary, parabolic/exponential trends would indicate micro- and mesoporous (i.e. hierarchal) structures. Differentiating between these two scenarios is dependent on the magnitude of change and can be compared with BET analysis. For UHS-SDC9, the BET pore structure was found to have hierarchal characteristics, where mesopores were dominant, in agreement with the trend shown in Fig. 3.5A, where true ionic charge separation is only observed at lower current densities. In addition, at 5 A g^{-1} , the specific capacitance has been reduced to $\sim 50 \text{ F g}^{-1}$, further supporting that ion penetration and mobility has been inhibited. The capacitance retention plot (Fig. 3.5B) indicates that specific capacitance retained 92% of the original value after the 2500-cycle period at 1 A g^{-1} . Notable dips in the retention plot are a direct result from the addition of 2 M KOH to counteract fluctuations of the electrolyte during extended testing.

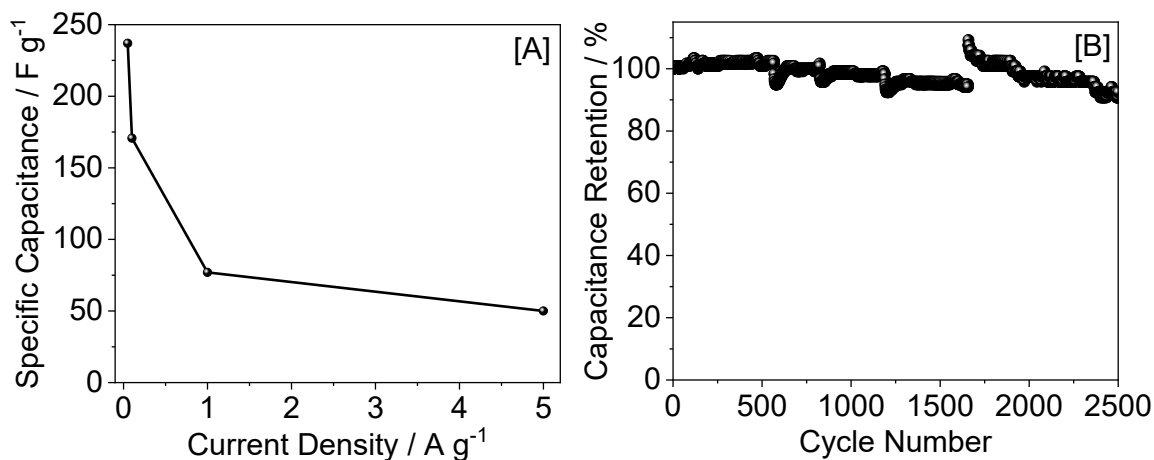


Figure 3.5 [A] Specific capacitance plotted with respect to current density obtained from CD for UHS-SDC9 biocarbon and [B] capacitance retention at 1 A g^{-1} for 2500 CD cycles for UHS-SDC9 with each point representing every 10th cycle.

Two symmetrical electrodes underwent galvanostatic charge-discharge to determine energy and power densities. Eqs. (3.4), (3.5) were utilized to calculate the energy and power densities, where biocarbon UHS-SDC9 obtained the highest energy and power densities of 9.9 Wh kg^{-1} and 2.5 kW kg^{-1} , respectively. Biocarbons UHS-SDC1, UHS-SDC2, UHS-SDC4, and UHS-SDC8 obtained calculated energy densities of 2.8, 7.8, 8.35, and 5.15 Wh kg^{-1} , respectively. Current literature reports energy densities ranging from 4.4 to 33.4 Wh kg^{-1} in aqueous electrolyte for corn-derived biocarbons, where UHS-SDC9 fits into this range.^{[67],[76],[93]}

Table 3.3 Crystallite size, interplanar distance, and specific capacitances at 5 mV s^{-1} of selected samples.

Sample	Scherrer's Equation Crystallite size, nm	Bragg's law Interplanar distance, nm	Specific capacitances at 5 mV s^{-1} , F g^{-1}
UHS-SDC1	0.39	0.135	173
UHS-SDC2	0.63	0.123	154
UHS-SDC4	0.39	0.137	180
UHS-SDC8	0.44	0.115	207
UHS-SDC9	0.80	0.137	242

The mean crystallite size and the interplanar distance of the selected biochar samples (UHS-SDC1, UHS-SDC2, UHS-SDC4, UHS-SDC8 and UHS-SDC9) were obtained from analyzing the peak broadening of the graphite basal (002) plane via the Scherrer equation and Bragg's law, respectively (Picard et al., 2020). The results are tabulated in Table 3.3. Biocarbons UHS-SDC1, UHS-SDC4, and UHS-SDC9 have interplanar distances (0.135–0.137 nm) that correlate to C=C bonding in the crystal lattice, while biocarbons UHS-SDC2 and UHS-SDC8 have interplanar distances (0.115–0.123 nm) that correspond to C≡C. The best electrochemical performance was obtained from UHS-SDC9 where the crystallite size was the highest, indicating enhanced

graphitization. Furthermore, the general trend of increasing specific capacitance agrees with increasing crystallite size, except for the case of UHS-SDC2. The lower capacitance for UHS-SDC2 can be explained by triple bonding characteristics, where low interplanar distances prevent ion penetration into the carbonous architectures (Table 3.3). To produce high performance biocarbon for electrochemical applications, optimal porous structures and graphitization are necessary. Although UHS-SDC9 had a lower S_{BET} , the highest specific capacitance of the reported biocarbons is attributed to increased crystallinity and pore volume. Jin et al. (2014) reports a corn stover-derived biocarbon with a higher S_{BET} ($1433 \text{ m}^2 \text{ g}^{-1}$) and pore volume ($0.76 \text{ cm}^3 \text{ g}^{-1}$), compared to our IBR processed material ($215 \text{ m}^2 \text{ g}^{-1}$, $0.12 \text{ cm}^3 \text{ g}^{-1}$).^[66] Despite the large differences in surface area and pore volume, the literature reports a similar specific capacitance of 246 F g^{-1} , whereas this work reports 242 F g^{-1} , attributed to higher crystallinity and enhanced hierarchal pore networks.^[66] The specific capacitance, physical characterization and preparation data for this and several recently reported corn-derived biomass electrode materials are compared in Table 3.4.

Table 3.4. Comparison of corn-derived biocarbon data for supercapacitor applications.

Material	Activation Technique	Specific Capacitance F g^{-1}	Surface Area $\text{m}^2 \text{g}^{-1}$	Pore Volume $\text{cm}^3 \text{g}^{-1}$	Retention %	Reported Cycles	Reference
Corn Stover	Facile Thermal Carbonization	242	215	0.12	92	2500	This Work
Corn Stover	Microwave Pyrolysis, KOH	246	1433	0.76	N/A	N/A	[66]
Corn Stem	KOH	232	1420	N/A	N/A	10000	[98]
Corn Straw	Hydrothermal Carbonization KOH,	222	1771	1.85	94	5000	[99]
Corn Husk	Thermal Carbonization	356	867	0.51	95	2500	[69]
Corn Stalk	KOH, Ni Catalyst	323	2495	1.23	98	1000	[100]
Corn Stalk	Fe Catalyst, Pyrolysis	213	540	0.48	99	6000	[67]

3.3.3 Optimization statistical analysis

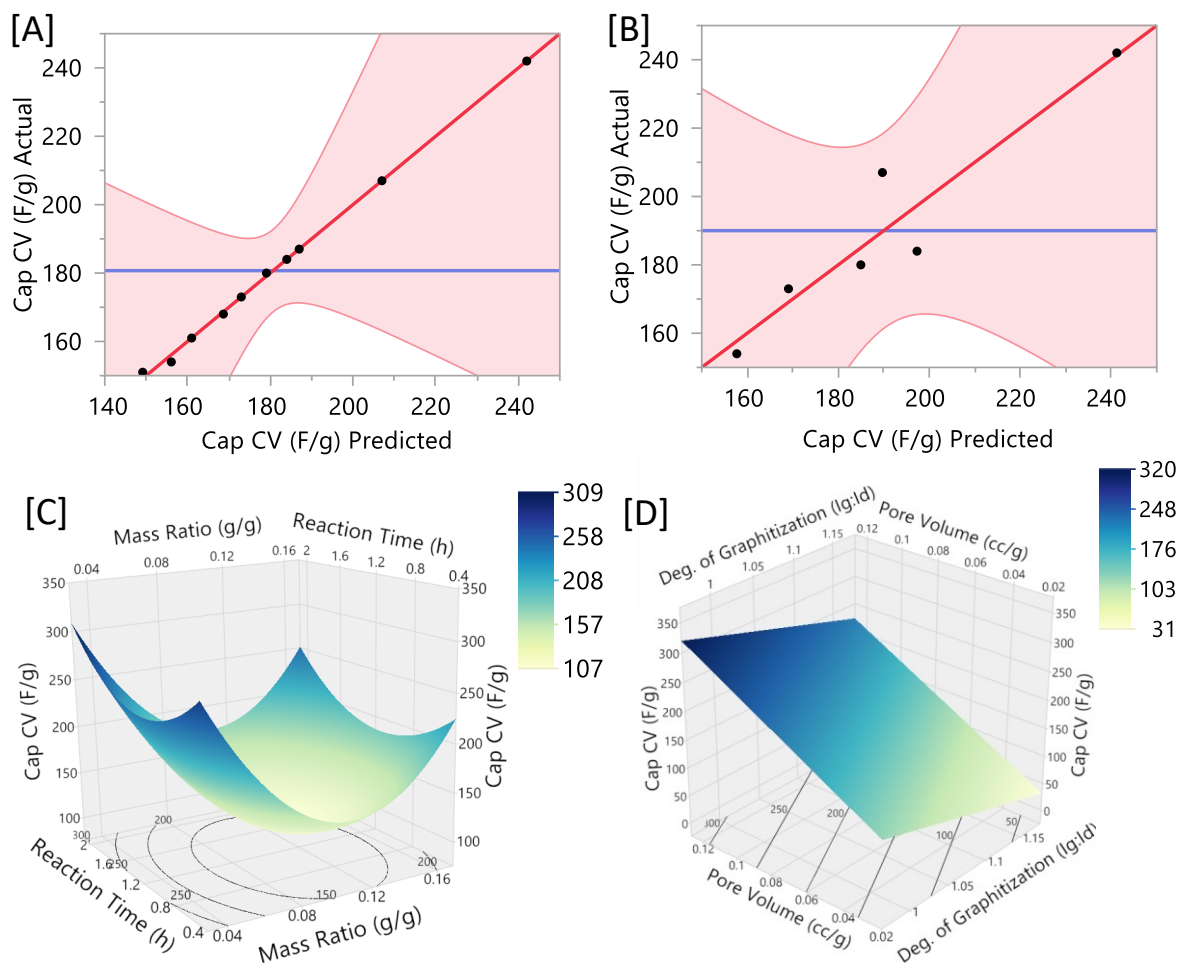


Figure 3.6 Least squares regression model for the effect of [A] HTL parameters and [B] physical characteristics of biocarbons on specific capacitance (CV at 5 mV s⁻¹). Surface contour plots for the prediction profile of [C] mass to water ratios and reaction time, and [D] pore volume and degree of graphitization as a function of specific capacitance (CV at 5 mV s⁻¹).

JMP software was employed to perform statistical analyses on the effect of HTL processing conditions and physical characteristics pertaining to electrochemical performance. The least squares regression analysis of specific capacitance (CV, 5 mV s⁻¹) as a function of the HTL processing parameters (i.e., temperature, pressure, biomass to water ratio, and reaction time)

displayed a linear trend with an R^2 of 0.99, signifying a highly correlated model (Figure 3.6A).

The governing equation for this model is described by Equations 2.6 – 2.10:

$$C_{theoretical} = 348.639 - M_E - T_E - P_E - R_E \quad (2.6)$$

$$M_E = 1567.115 \cdot M \left((M - 0.0733) \cdot ((M - 0.0733) \cdot 21649.030) \right) \quad (2.7)$$

$$T_E = 0.240 \cdot T \left((T - 275) \cdot ((T - 275) \cdot 0.017) \right) \quad (2.8)$$

$$P_E = 0.272 \cdot P \left((P - 53) \cdot ((P - 53) \cdot 0.005) \right) \quad (2.9)$$

$$R_E = 13.131 \cdot R \left((R - 1.05) \cdot ((R - 1.05) \cdot 71.160) \right) \quad (2.10)$$

where, $C_{theoretical}$ is the theoretical specific capacitance with respect to given variable inputs, M_E is the cumulative mass term for the effects of biomass to water ratio, T_E is the cumulative temperature term for the effects of temperature, P_E is the cumulative pressure term for the effects of pressure, R_E is the cumulative time term for the effects of reaction time, M is the biomass to water ratio, T is the reaction temperature in °C, P is pressure in psig, and R is reaction time in h.

This analysis further dictates that the biomass to water ratio (g:g) and reaction time (h) held the greatest significance on electrochemical performance for the HTL processing parameters, with p -values of 0.0279 and 0.0555 (h^2), respectively. A surface contour plot for this model displays the two most significant HTL parameters, where overall, a lower biomass to water ratio and longer reaction times are predicted to give the highest specific capacitances (Fig. 3.6C). The prediction profiler in JMP further determined that the optimized parameters for the given model and data set would achieve a theoretical maximum specific capacitance of 333 $F g^{-1}$ at a temperature, initial pressure, reaction time, and biomass to water ratio of 250 °C, 0 psig, 2 h, and 1:30 (g:g),

respectively. In agreement with the higher theoretical capacitances, when producing biomass residues (subsequent biochars), the lower biomass to water ratios and longer reaction times allow for the re-polymerization of organic compounds, which generates desirable biochars.^[101] Similarly, for the HTL of biocarbons, these parameters affect the yields of bio-crude (C1–C3 acids, etc.), where lower biomass to water ratios produce higher bio-crude yields.^[102] Experimental conditions similar to those described by the model were previously performed by Tungal and Shende (2014) which described possible chemical pathways that led to favorable yields of C1–C3 acids.^[102] An investigation into the effect of physical characteristics on electrochemical performance was also examined. The modeling software determined that the degree of graphitization and pore volume were the two most significant physical characteristics that affect the electrochemical performance of the biocarbons for this data set (Fig. 3.6B and 3.D). Therefore, an examination into the IBR processing parameters that affect the degree of graphitization and pore volume was conducted. Pressure was the most significant term in modeling pore volume (p-value of 0.0368), while temperature held the greatest effect on the degree of graphitization (p-value of 0.0682). An intuitive explanation for the positive effects of pressure and temperature during the HTL processing step is suggested by literature, where lower pressures result in the incomplete conversion of biomass to bio-crude and higher temperatures promote the re-polymerization of higher molecular weight compounds.^[101] Subsequently, this changes the composition of the solid residues to promote an increase in pore volume and higher degrees of graphitization for the electrode material. In summary, the model suggests the significance of the individual IBR processing parameters and physical characteristics that affect electrochemical performance, which intuitively agrees with literature and scientific understandings for biomass-derived electrode materials.

3.3.4 Perspectives

Production and research of quality biocarbon for electrochemical applications has remained at the bench scale. This may be attributed to the use of additional chemical/catalytic activation routes to increase surface areas and therefore capacitance. At the production scale, the costs associated with these activators significantly increase due to expenses that come with reagent and waste handling, plant operation (electricity, leasing, insurance), and labor. Presented in this work is a method for sustainably and effectively producing biocarbon suitable for supercapacitor production while maintaining scalable cost-effective practices. The model equations discussed are fundamental and may be applied at any scale in order to tailor physical parameters to specific applications of the biocarbon. The basis of these equations and methodology can be used for guiding researchers in predicting weighted parameter effects on biomass and subsequent biochar for application areas outside of energy storage as well, such as wastewater treatment or soil management, enhancing market viability. Pilot scale IBR derived biofuel precursors and biocarbon is projected for future works.

3.4 Conclusions

Pretreated biochar underwent a facile thermal activation process at 850 °C to produce biocarbon. The highest performing biocarbon was generated from the HTL of UHS at parameters of 275 °C, 40 psig, 1 h, and 1:30 ($\text{g}_{\text{biomass}}:\text{g}_{\text{water}}$). Biochar from these conditions yielded biocarbon (UHS-SDC9) with physical and electrochemical characterizations of 215 $\text{m}^2 \text{g}^{-1}$, 0.12 $\text{cm}^3 \text{g}^{-1}$, 242 F g^{-1} , and 9.9 W h kg^{-1} . Statistical analyses and modeling on the HTL conditions yielded a predicted theoretical specific capacitance of 333 F g^{-1} at 250 °C, 0 psig, 2 h, and 1:30 ($\text{g}_{\text{biomass}}:\text{g}_{\text{water}}$) for a corn stover-derived material.

Chapter IV. Production of Supercapacitor Carbon Electrodes from Corn-stover via a Facile Thermal Activation

Adapted From:

Katelyn M. Shell, Bharathkiran K. Maddipudi, Vinod S. Amar, Anuj Thakkar,
Rajesh V. Shende, Sandeep Kumar, and Ram B. Gupta. *TechConnect Briefs*. (2021).

Use of biomass is an emerging and promising alternative to produce carbon electrodes for supercapacitors. Lignin-rich unhydrolyzed solids (UHS) obtained from alkaline pretreatment of corn stover were hydrothermally liquefied (HTL) and the remaining solid after HTL was acid washed, then neutralized. Obtained biochar was converted to biocarbon using a facile one-step thermal activation process. Activation was carried out in a tubular furnace at 815 °C for 3 hours at a heating rate of 5 °C min⁻¹ under argon flow. Electrode ink was formulated by combining 80 wt.% biocarbon, 10 wt.% high conducting carbon black (Super P), and 10 wt.% polytetrafluoroethylene (PTFE, 60 wt.% in H₂O), and a reserved amount of H₂O. Slurry was applied to Ni foam, dried, pressed, then templated and insulated with chemical resistant epoxy. Electrochemical measurements were conducted using a potentiostat, where specific capacitances determined via cyclic voltammetry (CV) were found to be greater than 200 F g⁻¹. The electrodes produced were well suited for use in supercapacitors.

4.1 Introduction

Corn stover (leaves, stalks, cobs, husks and tassels) is an abundantly available biomass feedstock, typically consists of high amounts of lignin, cellulose and hemi-cellulose components, and is primarily sourced from the annual grain (corn) harvests of about 1.5 dry tons per acre.^{[103],[104]} The lignocellulosic components can be utilized for fermentation of sugars and other valuable products such as lactic acid, levulinic acid and phenols when separated from the complex cell wall of the corn stover via alkaline pretreatment and enzymatic hydrolysis processes.^{[105],[106]} The remaining solid residue which is rich in lignin can be further valorized into biochar. Among the different valorization techniques, hydrothermal liquefaction (HTL) can convert the biomass feedstock effectively compared to traditional pyrolysis and biological techniques. However, even such technology poses several technical challenges pertaining to mixing, pressurization, transport, and

pressure let down of high solid. slurries which requires an optimized process intensification step to realize its full commercial potential. [80],[107],[108]

Among the several products produced during valorization of the lignin-rich biomass feedstocks, our focus in this research work is on the hydrochar derived from the solid residue after the HTL process. Graphitic carbons for energy storage, particularly supercapacitors can be readily generated from the solid residues of HTL. Our past investigations show that the energy storage potential of such low cost biocarbon is comparable with commercial fossil graphite.^[109] Graphitic carbon derived from biomass is an inherently benign, stable, sustainable, and economically feasible product.^[17] Due to the lignocellulosic content and the structure of these compounds themselves, they provide an excellent template for generating biocarbon, even after HTL processing. The functional group rich compounds help create porous structures post thermal carbonization.^{[20],[21]} Under thermal activation, every cleaved group creates a pore which allows for ion storage, enhancing capacitance.^[110] Given this, the material is stable and capable of cycling >10,000 times when fabricated into a supercapacitor.

In this work, we explore the energy storage potential of the biocarbon derived from HTL of lignin-rich biomass feedstock under different catalytic environments and formulate a basic understanding on how the different catalysts can affect the electrochemical performance of the fabricated supercapacitors.

4.2 Experimental

4.2.1 Materials

Catalyst materials for hydrothermal processing such as Ni(NO₃)₂, Ni(OH)₂, K₂CO₃, and Ca(OH)₂ were purchased from Sigma Aldrich. Commercially available unhydrolyzed solids from an

ammonia fiber expansion process (AFEX) for the pretreatment of corn stover were obtained from Glydia Biotech.[13]–[15] Acetone (analytical grade) and HCl were purchased from Fischer Scientific. Ultra high purity Argon (> 99%) for thermal activation was purchased from Airgas. Polytetrafluoroethylene (PTFE) and carbon black (Super P conductive, 99+%) were purchased from Alfa Aesar. Nickel foam cathode material was purchased from MTI corp. Henkel Loctite EA 9462 Epoxy was purchased from Ellsworth adhesives. Double distilled water was obtained from an on-demand Barnstat filtration system.

4.2.2 Biochar synthesis

Commercial UHS obtained from alkaline pretreatment and enzymatic hydrolysis of corn stover is hydrothermally liquefied (HTL) in 300 mL bench scale PARR reactor, where the biomass components are diluted in water at a ratio of 1:10 (w:w) and the HTL conversion process was carried out at 100 psi, initial N₂ pressure, 275 °C reaction temperature for 1 hour residence time in the presence of catalyst at loading of 5 wt.%. To understand the effect of catalyst during the valorization process, a series of HTL experiments were individually carried out with catalysts such as Ni(NO₃)₂, Ni(OH)₂, K₂CO₃, and Ca(OH)₂. Following the reaction, the reactor contents were cooled down and the solid residue is separated from the aqueous liquid stream via vacuum filtration and later washed with several passes of acetone to remove the sticky bio-oil components from the hydro/biochar, which is later dried overnight at 65 °C in conventional oven and proceeded to thermal activation in the presence of inert N₂ environment at 400 °C for 2 hours. Finally, the resultant biochar is further graphitized to obtain high value biocarbon. Additional details pertaining to the alkaline pretreatment and enzymatic hydrolysis steps, HTL reactor set-up and its operation, and extraction of solid residue are provided elsewhere.^{[111],[112]}

Table 4.1. List of experimental parameters for HTL of corn stover-derived biochar.

Sample Code	Catalyst Type	Cat. w/w	Rxn. Temp. (°C)	Rxn. Time (h)	Int. Pres. (psi)
H1C	Ni(NO ₃) ₂	5%	275	1	100
H2C	Ni(OH) ₂	5%	275	1	100
H3C	K ₂ CO ₃	5%	275	1	100
H4C	Ca(OH) ₂	5%	275	1	100
H5C	Ca(OH) ₂	3%	275	1	100
H6C	Ca(OH) ₂	7%	275	1	100
H8C	Ca(OH) ₂	9%	275	1	100

4.2.3 Biocarbon Synthesis

As-received catalytic biochar underwent a standard acid wash as reported by Shell et al. (2021).^[113] Neutralized biochar was placed in the vacuum oven at 40 °C and -10 psig overnight. About 0.33 g of biochar was placed in a ceramic boat and placed in the tube furnace. The tube furnace was set to 815 °C or 3 h with a ramp rate of 5 °C min⁻¹ under slow argon flow. Biocarbons were removed and weighed after naturally cooling. All biocarbon samples follow the naming convention of the biochars denoted in Table 1.

4.2.4 Electrode Fabrication

Biocarbons were first prepared into a slurry where biocarbon, carbon black (Super P), and polytetrafluoroethylene (PTFE, 60 wt.% in H₂O) were mixed into a slurry at an 8:1:1 mass ratio. The slurry was spread evenly onto reduced Ni foam electrode (1 cm x 3 cm) then dried in a vacuum over night at 40 °C and -10 psig. Once dried, the electrodes were pressed and templated using chemical resistant epoxy. The epoxied electrodes were allowed to cure overnight. Electrode active areas were found by a ratio of geometric areas via ImageJ software. Pictures of the electrodes for active area calculations were taken prior to a post epoxying along with reference material.

Electrochemical measurements were conducted in triplicate on a CH Instruments 660E potentiostat in a 3-electrode format. A working (fabricated), counter (Pt wire), and reference (sat. Ag/AgCl) electrodes were employed for the 3-electrode system. All electrochemical measurements were conducted in 2 M KOH aqueous electrolyte solution. Cyclic voltammetry (CV), galvanostatic charge-discharge (CD), and electrochemical impedance spectroscopy (EIS) were performed to give enhanced insights into electrochemical performance. Specific capacitances from CV and CD were found utilizing Equations (4.1) and (4.2), respectively.

$$C_{CV} = \frac{\int_{V_1}^{V_2} I dV}{m v \Delta V} \quad (4.1)$$

$$C_{CD} = \frac{I t}{m \Delta V} \quad (4.2)$$

where, V_1 and V_2 are the voltage window endpoints in V, I is the current in A, m is the active mass in g, v is the scan rate in mV s^{-1} , ΔV is $V_1 - V_2$, and t is the time to charge in s.

4.3 Results and Discussion

Each catalyst presented in this study offers unique characteristics that are beneficial during the HTL of corn stover. Nickel homogeneous catalysts drastically lower the activation energy needed to cleave the internal linkages of the lignin molecule present in biomass. The cleavage of such bonds produces H_2 gas, opening reductive pathways for the deconstruction of lignocellulosic compounds.^{[114],[115]} To this regard, the general presence of nickel reduces tar formation and char yield. In this study two types of Ni-catalyst were used, the nitrate and hydroxide forms. In

literature, hydroxides tend to neutralize connecting molecules formed during char polymerization.^[116] During thermal activation these groups are effectively cleaved generating increased pore structures. This positively effects the production of bio-oil and enhances the material properties biocarbon produced from biochar. Much like nickel, K_2CO_3 reduces the activation energy needed to cleave internal lignin linkages and has demonstrated its capability to increase bio-oil yield which suppresses biochar formation.^[116] This is due to a water-gas shift reaction that occurs under the presence of K_2CO_3 .^[116] Calcium hydroxide is deemed an inexpensive and effective catalyst during HTL. Calcium in its dissociated form demonstrates higher catalytic activity at lower temperatures versus other metal-catalysts presented, thus a suitable choice for HTL.^[117] A detailed description on the catalytic depolymerization/deconstruction reaction pathways of lignocellulosic compounds is detailed by Lu et al. 2020.^[117] While the focus of these experiments was to study the effect of the various catalysts on electrochemical performance, it is important to note that utilizing a catalyst that enhances both the liquid and solid co-products is most desired.

Cyclic voltammetry was performed on all samples in 2 M KOH with a voltage window from -1 to 0 V vs Ag/AgCl (sat.). Cyclic voltammograms shown in Figure 4.1 demonstrate smooth CV curves with no reversible or irreversible reactions, indicating ideal capacitive behavior.^[118] Biocarbon H1C demonstrated the highest capacitance among all the samples as confirmed by the largest area in Figure 1. Biocarbon H1C reached a specific capacitance of 203 F g^{-1} at 5 mV s^{-1} ($\pm 12\%$), while all others were below 190 F g^{-1} ($\pm 15\%$), signifying improved ion transport within the carbonaceous framework. This increase in electrochemical performance can be attributed to the $Ni(NO_3)_2$ utilized during the HTL synthesis of hydrochar and subsequent biochar. Ni has been cited in literature to give improved bio-oil and decreased char yields during the HTL of biomass.^[115] In

turn, this could have a positive effect on biocarbon characteristics, such as decreased O, N, and H presence, post carbonization. Biocarbon H2C held similar, but decreased capacitance values at lower scan rates (5-20 mV s^{-1}) when compared to H1C biocarbon. Interestingly, H2C biocarbon showed a higher capacitance value at faster scan rates over H1C biocarbon. H2C achieved a specific capacitance of 107 and 72 F g^{-1} ($\pm 15\%$) versus H1C which only achieved 95 and 59 F g^{-1} for scan rates 50 – 100 mV s^{-1} . Nickel hydroxide was utilized during the HTL of H2C material and suggests that Ni containing reagents offer enhanced pore structures when compared to other catalysts in this sample set.

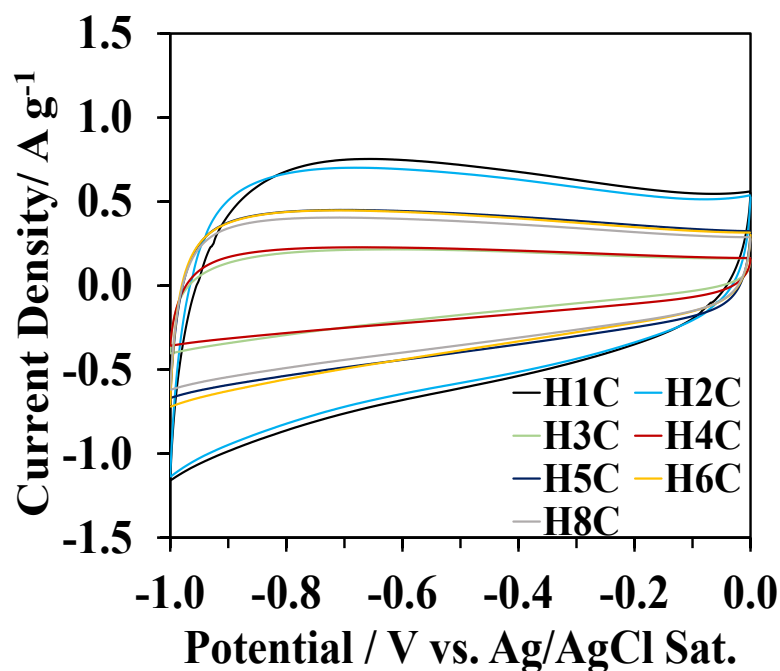


Figure 4.1. Cyclic voltammetry curves of various prepared biocarbons at 5 mV s^{-1} .

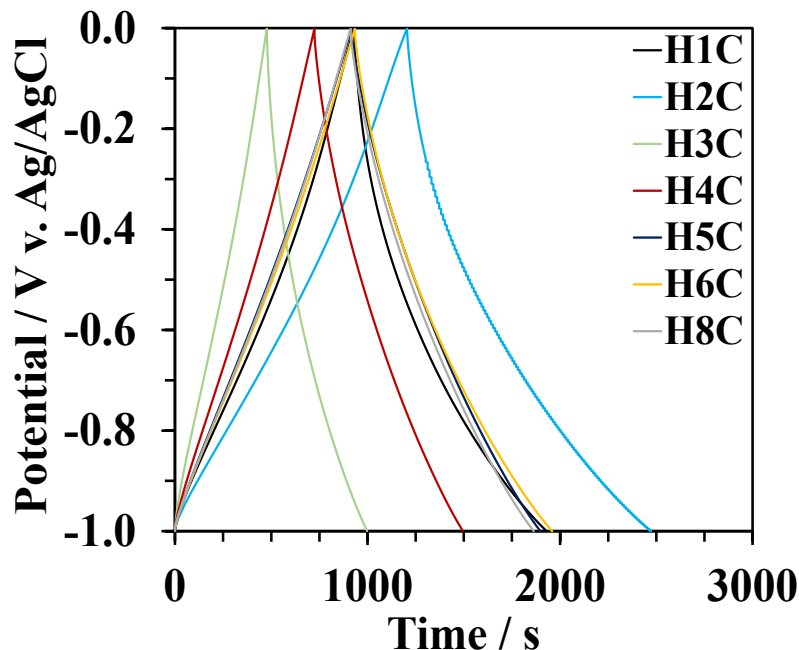


Figure 4.2. Charge-discharge curves for various prepared biocarbons at 0.1 A g⁻¹.

All samples underwent galvanostatic CD to give further insights into electrochemical behavior. For supercapacitors, CD gives pseudo real world performance characteristics. Figure 4.2 illustrates all CD curves catalytic samples at 0.1 A g⁻¹. All curves demonstrated smooth sawtooth-like curves indicating sufficient charge separation and ideal EDLC behavior.^[110] Biocarbon H2C demonstrated a significantly longer charge and discharge time over all other samples with a specific capacitance of 93 F g⁻¹ ($\pm 25\%$) at 0.1 A g⁻¹ and increased retention of specific capacitance at higher current densities (1 – 10 A g⁻¹). Apparent in Figure 4.2 are three CD curves that are strikingly similar. Biocarbons H1C, H6C, and H8C held specific capacitances within 10 F g⁻¹ of each other, however their catalyst and catalyst loading (Table 4.1) were significantly different. Materials H1C, H6C and H8C were prepared with catalyst loading of 5 wt.% Ni(NO₂)₃, 7 wt.% Ca(OH)₂, and 9 wt.% Ca(OH)₂, respectively. This suggests that a higher calcium hydroxide loading during HTL could achieve similar electrochemical performance. If scaled, this could

significantly reduce costs as $\text{Ca}(\text{OH})_2$ cost is $\$5\text{-}30 \text{ ton}^{-1}$ whereas nickel nitrate costs about $\$ 4,000 \text{ ton}^{-1}$.^{[119],[120]}

Further electrochemical characterizations were performed though EIS to understand internal electrode properties such as internal resistances and ion transfer characteristics. Figure 4.3 depicts each material's capabilities in three distinctive regions: high frequency (semi-circle), medium frequency (intermediate), and at low frequency. The high frequency region denotes interfacial charge transfer resistance where a smaller region is desired.^[19] The medium, or intermediate, region signifies the ion diffusion from electrolyte to electrode surface, where a slope of 1 is desired and represents the Warburg resistance.^[121] The low frequency region corresponds to ideal capacitive behavior.^[122] An angle of 90° (i.e., slope ∞) is desired, however when comparing within a sample set, the highest slope is taken as most ideal.

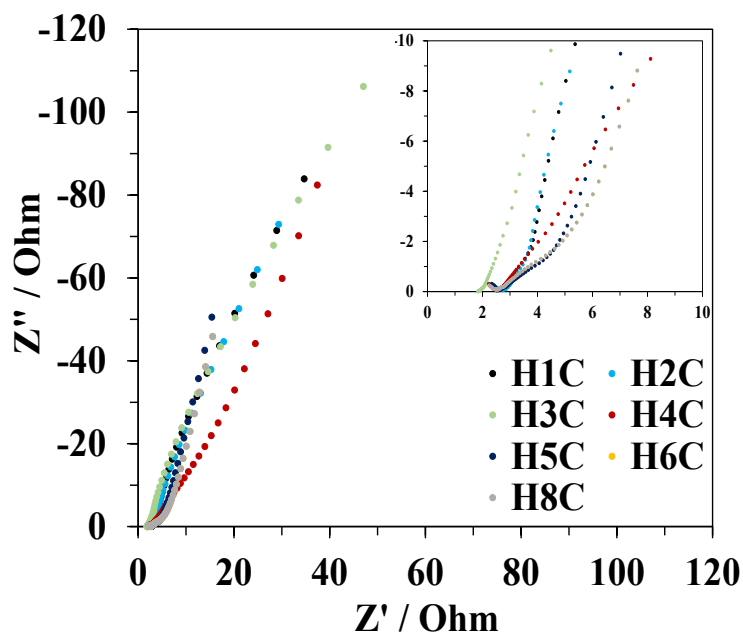


Figure 4.3. Electrochemical impedance spectroscopy of prepared biocarbons.

Table 4.2. Summary of EIS data for biocarbons.

Sample	R_b / Ω	S_i	S_L
H1C	2.54	1.72	2.65
H2C	2.72	2.14	2.73
H3C	1.91	2.75	2.16
H4C	2.56	1.39	2.32
H5C	2.59	0.98	4.73
H6C	2.72	1.04	4.20
H8C	2.54	0.92	4.44

Due to the incomplete semi-circle region for all samples, only the bulk solution resistance (R_b) could be determined from the high frequency region. Biocarbon H3C achieved the lowest R_b at 1.91 Ω . In the medium frequency region H5C held a slope (S_i) of 0.98, the closest to the ideal slope of 1. H5C also held the highest slope (S_L) (4.73) in the low frequency region. Interestingly, all samples where Ca catalyst was used during HTL achieved an S_i closer to 1 versus Ni catalyst samples. This is due to Ca having enhanced catalytic activity on biomass at lower temperatures.^[117] Here, biomass underwent HTL processing at 275 °C and 100 psi, therefore graphitic precursors are probable from material produced using $\text{Ca}(\text{OH})_2$. All EIS data is summarized in Table 4.2.

4.4 Conclusions

Corn stover biomass underwent HTL in the presence of various catalysts followed by low temperature annealing of biochar at 400 °C for 1 h. Subsequently biochar underwent thermal activation at 850 °C (815 °C actual) for 3 h. The resulting biocarbons were fabricated into electrodes where electrochemical characterizations were performed. Biocarbon H1C (prepared using $\text{Ni}(\text{NO}_3)_2$ catalyst achieved the highest specific capacitance (203 F g^{-1}) with H2C (prepared using $\text{Ni}(\text{OH})_2$ catalyst) maintained higher capacitances at faster scan rates and current densities,

indicating the enhanced electrochemical performance of Ni-based catalysts during HTL processing. Materials derived from HTL using $\text{Ca}(\text{OH})_2$ may offer a cheaper alternative with similar electrochemical performance and enhanced charge transfer kinetics over nickel-based catalyst samples.

Chapter V. Phytoremediation of Nickel via Water Hyacinth for Biocarbon-derived Supercapacitor Applications

Adapted From:

Shell, K.M., Vohra, S.Y., Rodene, D.D. and Gupta, R.B. (2021), Phytoremediation of Nickel via Water Hyacinth for Biocarbon-Derived Supercapacitor Applications.

Energy Technol. 2100130

Water hyacinth (*Eichhornia crassipes*, WH) was cultivated in a hydroponic system containing various concentrations of Ni^{2+} to demonstrate phytoremediation techniques as a facile, low-cost, and sustainable method for synthesizing high performance biocarbon electrode materials. A high specific capacitance of 541 F g^{-1} in 2 M KOH was achieved for WH-5 biocarbon with an energy density of 30.5 W h kg^{-1} . Materials were assembled into a coin cell supercapacitor capable of lasting 10,000 cycles with 100% capacitance retention. Surface area characterizations supported these results with an S_{BET} of $3429 \text{ m}^2 \text{ g}^{-1}$, V_{BET} of $2.13 \text{ cm}^3 \text{ g}^{-1}$, and an S_p avg of 2.5 nm indicating enhanced pore formation and functional group cleaving. Raman spectroscopy, ATR-FTIR, and XRD give further insight into physical characteristics of the biocarbon that lead to improved electrochemical performance. This work describes an optimal concentration of preabsorbed Ni^{2+} catalyst (5 ppm in H_2O) capable of achieving 98% of theoretical capacitance and value-added environmental cleanup associated with synergistic remedial techniques.

5.1 Introduction

The U.S. generates approximately two billion tons of mining waste annually, leading to inorganic heavy metal contaminants such as Cd^{2+} , Cr^{3+} , Pb^{2+} , Ni^{2+} , Zn^{2+} , Se^{2+} , Cu^{2+} and Co^{2+} deposited into surrounding ecosystems at toxic levels.^{[123],[124]} Remediating these sites involves costly, invasive, detrimental, and labor-intensive methods that can leave ecosystems damaged for decades.^[125] Across the world, developing countries are unable to adopt these remediation practices due to these factors, generating a need for sustainable low-cost methods to remediate mining sites. Phytoremediation is the practice of utilizing plants in water or soil to degrade, transfer, or bioaccumulate pollutants. This method offers an environmentally benign, nondestructive, simple, inexpensive, and effective way to remediate ecosystems that have been destroyed by urbanization and industrialization.^{[124],[126]} Phytoremediation of metal mining pollutants has been prominently

examined as a strategy for treating contaminated mining sites for decades, however, current phytoremediation strategies generate unused biomass that can create value-added products (phytoproducts), such as reclaimed-metals, biofuels and energy storage materials.^[127]

Plants that are able to uptake and retain heavy metals without any detrimental effects are known as hyperaccumulators. One plant of high interest as a hyperaccumulator is *Eichhornia crassipes*, commonly known as water hyacinth (WH). This rapidly colonizing plant has demonstrated its ability to uptake elements such as Ni^{2+} , Cu^{2+} , N, and P, with removal efficiencies up to 82% for industrial wastewater treatment applications.^{[128]–[131]} Many of these contaminants play a vital role in biological processes such as the enzymatic activity glyoxalase-I and urease for nitrogen metabolism, however large quantities cause damage to DNA, creating mutagenic effects in both plants and animals.^{[132],[133]} Nickel in particular is the second most absorbed metal in plant roots and third in shoots, indicating readily available uptake capabilities of plants.^[132] Here, amino acids such as histidine regulate Ni^{2+} uptake and act as chelators in the form of complexes. Initial uptake of Ni-H₂O complexes by root systems gives way to Ni-amino acid multiplexes during natural biological processes.^[132] WH's viability as a hyperaccumulator comes from its ability to upregulate and downregulate specific proteins to manage toxins.^[134] WH also contains shock proteins that have certain antioxidative properties allowing them to handle free radicals species generated from metal ions.^[134] These intrinsic and adaptive capabilities of WH provide an excellent basis as a biomass precursor for applications in the area of energy storage, particularly biocarbon supercapacitors.

Biomass as a precursor material for supercapacitors offers many desirable characteristics, such as high abundance, low cost, and is environmentally benign.^[17] Meanwhile, commercial supercapacitors and batteries utilize carbons derived from petroleum-based coking processes,

which are not sustainable for future progressions.^[6] Biomass offers a carbon-rich framework suitable for electrochemical applications that can be activated and graphitized into a highly porous, stable, and versatile materials.^[113] Currently, biomass activation into biocarbon requires the use of metal catalysts, particularly Ni. This method, though effective, introduces additional steps in biocarbon production which can negatively affect process scale up.^[113] The benefits of embedded catalysts from phytoremediation eliminates the necessity for post treatment, provides a low-cost catalyst source, and generates an enhanced carbon framework advantageous for supercapacitor applications.

Supercapacitors are considered as highly versatile electrochemical devices that are rapidly increasing in commercial prevalence. Currently, these devices are heavily used for regenerative braking systems in hybrid-electric vehicles. They have acceptable power densities, high cyclability, and are known for being extremely stable at various environmental conditions.^{[74],[135]} Current supercapacitors have lower energy densities ($0.1\text{--}10\text{ W h kg}^{-1}$) than Li-ion batteries ($10\text{--}100\text{ W h kg}^{-1}$), therefore increasing the energy density while maintaining power density of these devices is desired.^[75] Electrochemical double layer capacitors (EDLCs) store ions on the surface and in the pores of the electrodes when a voltage is applied, creating an electrostatic charge separation.^[75] Therefore, an increase in viable pores ($> 0.8\text{ nm}$) can significantly increase specific capacitance, thus increasing energy density.^{[13],[75]} Activation through thermochemical methods increases cleavage of functional groups within the lignocellulosic framework of biomass, which can generate desired pore structures.^[136] Utilizing pre-absorbed, naturally embedded Ni through phytoremediation techniques offers a low-cost, facile, sustainable, and synergistic method of introducing catalysts that effectively enhance the physical properties conducive to energy storage

applications. The biomass harvested from hyperaccumulators for environmental remediation are postulated to be utilized as a value-added precursor material for energy storage applications.

The effect of embedded Ni within the cellular tissue of WH and its preliminary significance on electrochemical performance was previously investigated by Sima et al. (2019).^[19] However, the study presented herein details further examination of Ni²⁺ uptake by WH and application in supercapacitors where various concentrations of embedded Ni and its effect are studied. Fundamental understanding of the materials obtained are derived from physical characterizations including ICP, SEM, BET, ATR-FTIR, Raman spectroscopy, and XRD analyses. Electrochemical performance is studied using CV, CD, EIS, and a cyclability analyses. Experiments are carried out to find if there is an optimum Ni concentration for enhanced electrochemical performance. This study aims to valorize a natural environmental cleanup strategy further enabling sustainable phytoremediation efforts.

5.2 Materials and Methods

5.2.1 Materials

Water Hyacinths (*Eichhornia crassipes*) were purchased from AquariumPlants.com. FlouroDuo hydroponic plant nutrient solution was purchased from General Hydroponics (WV, USA). Analytical grade nickel nitrate (Ni(NO₃)₂·6H₂O, >99 wt.%), hydrochloric acid (HCl, 1 M) and ethanol (C₂H₅OH, 95 wt.%) were purchased from Fisher Scientific (MA, USA). Polytetrafluoroethylene (PTFE, 60 wt.% dispersed in water) and potassium hydroxide (KOH, flakes, 90 wt.%) were purchased from Sigma-Aldrich (MO, USA). Carbon black (Super P conductive, >99 wt.%) was purchased from Alfa Aesar (MA, USA). Ultra-high purity (grade 5.0) argon was purchased from Airgas (PA, USA). Double distilled (18.2 MΩ) water was obtained

from an on-demand Barnstat filtration system. Nickel foam substrates were purchased from MTI Corporation (CA, USA). Henkel Loctite Hysol 9462 epoxy adhesive was purchased from Ellsworth Adhesives (WI, USA).

5.2.2 Water Hyacinth Cultivation and Harvesting

As-received Water Hyacinths (WHs) were cultivated in a hydroponic system (Figure S1) with 0, 5, 10, and 25 ppm of Ni²⁺ from nickel nitrate for 14 days. WH were grown under full spectrum lighting with 12 h on/off cycles and 16 ml of FlouroDuo plant nutrient solution to supplement each tank (4 L). Received WH plants were weighed prior to and post the growth period. On day seven of the growth cycle, water with respective concentrations of Ni²⁺ were added to each tank to account for evaporation and plant uptake losses. After the growth period, plants were harvested and dried at 110 °C for 7 days under vacuum. WH were ground and particles were fractionated into two groups: above and below 150 µm.

5.2.3 Production of Biocarbon

Ground WH biomass (~2 g, ≤ 150 µm) was thermally annealed in a tube furnace at 500 °C (ramp rate 3 °C min⁻¹) under argon for 1 h. Following thermal annealing, potassium hydroxide at a 4:1 mass ratio (KOH : biochar) was ground with WH biochar until homogenous. The mixture was then placed in the tube furnace for high temperature activation at 800 °C (ramp rate 3 °C min⁻¹) under inert atmosphere for 1 h. A standard acid wash procedure was conducted post activation whereby 1.0 M HCl was added to the recovered KOH-biocarbon complex followed by sonication for 10 min. The suspension was centrifuged at 3000 RPM for 4 min, then decanted. This process was repeated once more before neutralization. A few drops of 0.5 M NaOH were added to the WH biochar followed by generous washing with double distilled water (18.2 MΩ). The neutralized WH biocarbons were dried in a vacuum oven at -10 psig and 50 °C.

5.2.4 Physical Characterizations

Nickel content in WH biomass was measured by inductively coupled plasma optical emission spectroscopy ICP-OES using Agilent Technologies 5110 ICP-OES analyzer operated in axial mode. Here, 100 mg of biomass was prepared in 5 vol.% HNO₃ solution with a 10 ppm Al³⁺ internal standard. Topological morphology was examined by scanning electron microscopy (SEM) utilizing a Hitachi Model FESEM Su-70 operating at 20 keV coupled with an electron dispersive X-ray (EDX) detector. Samples for SEM were prepared by adhering powdered biocarbon to double-sided carbon tape (Ted Pella, Inc.) on an aluminum specimen holder. Multipoint Brunner-Emmet-Teller surface area (SBET) characterizations were performed on a Quantichrome Nova 2400e analyzer. Degassing was conducted prior to BET experiments for 15 h at 150 °C. Attenuated total reflectance Fourier transform infrared spectroscopy (ATR-FTIR) was performed on a Thermo Fisher Scientific Nicolet iS10 infrared spectrometer to assess WH functional groups throughout thermal processing. A total of 8 scans were performed for each sample. A LabRam HR Evolution Raman spectrometer (532 nm, 25% power) with sampling range of 800 to 2100 cm⁻¹ utilized for Raman spectroscopy. X-ray diffraction crystallography was performed on all biocarbon samples by operating a Rigaku MiniFlex II x-ray diffractometer with a Cu K α radiation source at a scan speed of 1.0 ° min⁻¹, from 15 to 80 °, and a sampling width of 0.01 °. A constant voltage of 30 kV at 15 mA and wavelength of 1.54 Å were employed.

5.2.5 Electrochemical Characterizations

Recovered WH biocarbon was fabricated into supercapacitor electrodes through a standard technique.^[113] Electrode ink was prepared by mixing WH biocarbon with Super P and PTFE in an 8:1:1 mass ratio. A few drops of water were added to form a viscous slurry which was evenly spread on reduced nickel foam substrate (1 cm × 3 cm). All electrodes were dried in a vacuum

oven at -10 psig and 50 °C for 16 h. The dried electrodes were pressed, templated and insulated using chemical resistant epoxy. Due to resistances attributed to multiple layers of biocarbon, a monolayer of WH biocarbon ink was applied to each electrode. All electrodes were 0.14 mm post pressing with negligible thickness from biocarbon ink and fabricated in triplicate.

Active area calculations were performed by ratioing geometric areas prior to and after templating and insulating electrodes from digital images with reference material present. These images were analyzed by ImageJ software and calculated using following equation (5.1).

$$A_m = \frac{A_{PrN}}{A_{PoN}} \cdot \frac{A_{PoB}}{A_{PrB}} \cdot (0.8 m_B) \quad (5.1)$$

Where A_m is the active mass of the electrode and m_B is the total mass of dried material on the electrode. A_{PrN} and A_{PoN} is the pixel area of the reference pre- and post-templated, respectively. A_{PoB} and A_{PrB} is the pixel area of the biocarbon material in the post- and pre-templated image, respectively. Since the biocarbon slurry is 80 wt.% biocarbon, the total dried mass was multiplied by 0.8.

Electrochemical characterizations were performed on a CHI 660e electrochemical workstation in 2 M KOH where a standard 3-electrode (3-cell) system (Figure S2A), consisting of a working, Pt counter, and sat. Ag/AgCl reference electrodes, was utilized for cyclic voltammetry (CV), galvanostatic charge-discharge (CD), and electrochemical impedance spectroscopy (EIS). A two electrode (2-cell) system (Figure A2.2B), comprised of two identical electrodes for the working and reference/counter, was employed for CD to obtain energy and power density calculations. Specific capacitance from 3-cell CV and CD are described by equations (5.2) and (5.3) while 2-cell specific capacitance, energy density and power density calculations are described by equations (5.4), (5.5), and (5.6), respectively.

$$C_{CV} = \frac{\int_{V_2}^{V_1} i dV}{m \eta \Delta V} \quad (5.2)$$

$$C_{CD} = \frac{i t}{m \Delta V} \quad (5.3)$$

$$C_{2cell} = \frac{i t^*}{m \Delta V} \quad (5.4)$$

$$E = \frac{C_{2cell} \Delta V^2}{7.2} \quad (5.5)$$

$$P = \frac{E}{t^*} \quad (5.6)$$

V_1 and V_2 describe the voltage window limits in volts, i is the current in amps, m is the active mass of the working electrode in grams, η is the scan rate in mV s^{-1} , ΔV is $V_1 - V_2$ in volts, t is the time to charge in seconds and t^* is the time to discharge in seconds.

5.3 Results and Discussion

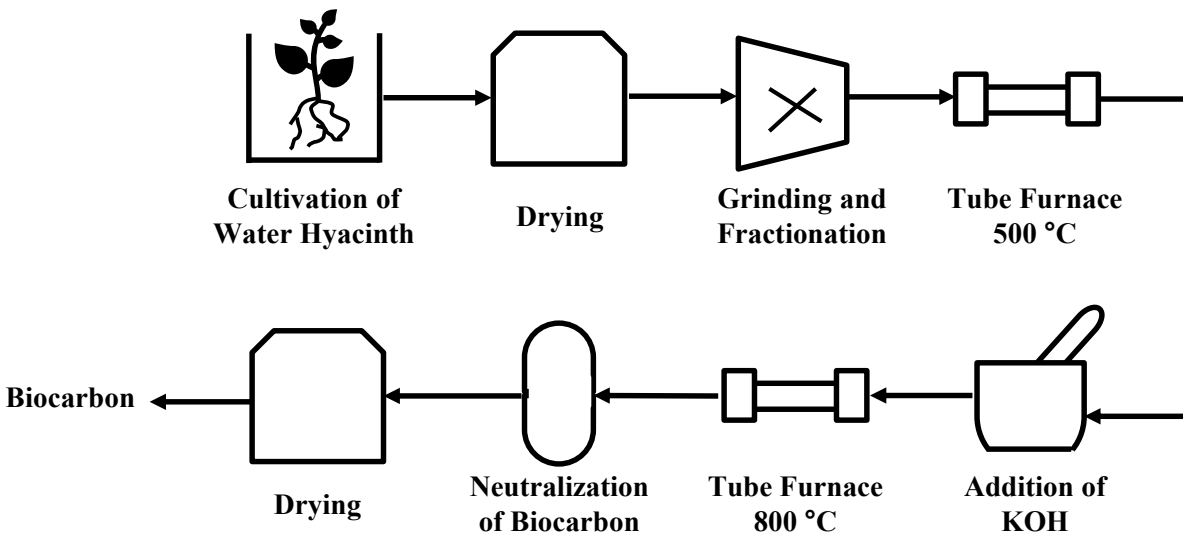


Figure 5.1. Process flow diagram for proposed phytoremediation of Ni to biocarbon product.

Biocarbon synthesis utilizing WH biomass from the phytoremediation of Ni^{2+} and effect of different embedded Ni concentrations was successfully demonstrated. Nickel nitrate was first added to the hydroponic systems, where it dissociates into Ni^{2+} and NO_3^- . The water hyacinth then uptakes Ni^{2+} ions to form ionic complexes within cellular tissues.^[137] Nickel is reported in the cited work to exist within the cellular tissue as Ni^{2+} prior to and post thermal treatment. The cultivation of WH in Ni^{2+} doped water provides a low-cost, naturally embedded source of catalyst which lowers the activation energy needed for the bond cleavage of functional groups during low-temperature thermal annealing and high temperature thermochemical/catalytic activation. Potassium hydroxide further assists in bond cleavage, leading to the formation of micro and mesopores which are desirable for electrochemical activity. In general, a higher KOH mass ratio gives lower biocarbon yields due to the enhanced functional group cleaving, lowering the mass of the biocarbon. Percent yields for the presented biocarbons were 5.0, 6.3, 3.1, and 4.7 wt.% for WH-0, WH-5, WH-10 and WH-25, respectively (Table 5.2). The post-activation removal of Ni ensures a neutral material without any pseudocapacitance during the electrochemical operation of the supercapacitors.

5.3.1 Physical Characterizations

Table 5.1 Concentration and bioconcentration factor (BCF) of Ni in WH biomass after 14 days, determined from ICP-OES.

Sample	Initial Ni ²⁺ conc. of the water	Ni content of the biomass	BCF
	[ppm]	[ppm]	[L kg ⁻¹]
WH-0	0	0	-
WH-5	5	53,500	10,710
WH-10	10	106,300	10,630
WH-25	25	568,000	22,720

The determination of Ni content was performed utilizing ICP-OES to examine Ni uptake (post-growth stage) as shown in Table 5.1. ICP-OES results sufficiently demonstrated the capabilities of water hyacinth (WH) as a hyperaccumulator, where Ni concentrations were found to be orders of magnitude higher within the WHs than in the water. This indicates that the plants actively up took the metal and that the presence was not just a result from being at equilibrium with bulk water. Increasing Ni²⁺ content in the system lead to an exponential increase of Ni with the biomass samples as shown in Figure A7.3. Ni concentration of as high as 568,000 ppm was reported, further supporting the high capability of WH as a hyperaccumulator. The bioconcentration factor (BCF) was calculated for each sample set which offers a quantifiable method for assessing the plant's ability to uptake heavy metals. The BCF is the ratio of metal in the biomass divided by the concentration of metal in the solution (water or soil) and is denoted as L kg⁻¹. The WH biomass exhibited strong BCFs ranging from 10,700 to 22,720 L kg⁻¹ for water concentrations from 5 to 25 ppm Ni²⁺, respectively. Substances with a BCF greater than 5,000 are classified as “very bio-accumulative” (vB) for aquatic species, thus the WH is denoted as such.^[138]

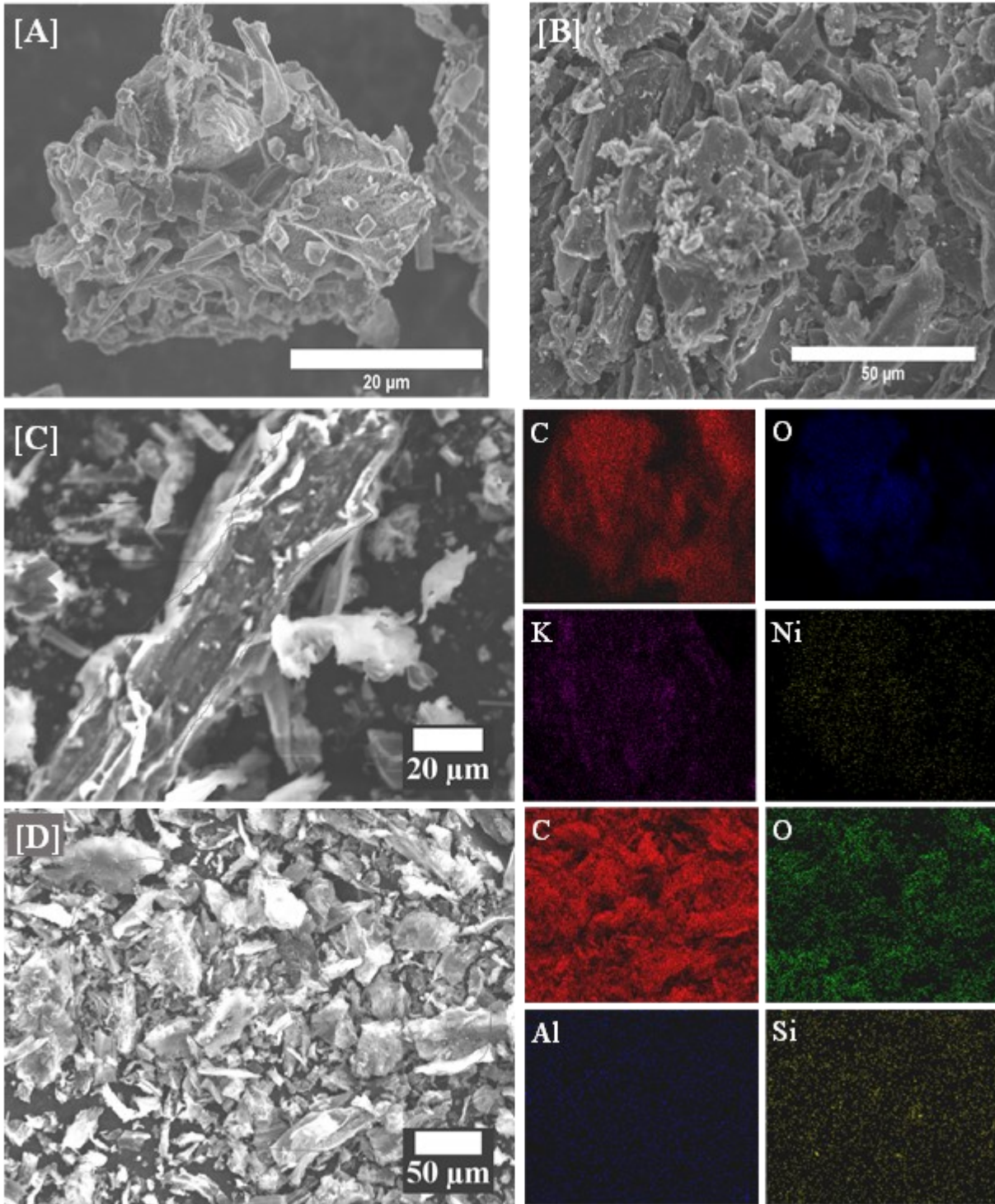


Figure 5.2. SEM images of WH-5 [A, C] biochar and [B, D] biocarbon, where [C] and [D] are reference images collected from the EDS analysis. Elemental maps of [C] and [D] show C, O, K, and Ni; and C, O, Al, and Si for WH-0 and WH-5, respectively.

SEM images of WH-5 biochar (Figure 5.2A) demonstrate the complex morphology of WH-derived biochars. Observed in the same image are bonded metals, such as potassium, on the surface of the WH-5 biochar. The elemental mapping from Figure 5.2C confirms the presence of K and low Ni prevalence of 0.51 wt. %. A lower Ni concentration from EDS is attributed to the method's ability to detect only surface elements. This further confirms WH's aptitude to embed Ni within the cellular structure of the plant. Conversion of biochar into biocarbon further removes remaining volatile compounds and converts metal-bound sites into pores. Figure 5.2B illustrates these features in a topological format, where intricate regions significantly increase the surface area of the biocarbon. Large macropores are observed on the surface of the WH-5 biocarbon, which increases the transport of ions into the biocarbon's framework. EDS imaging of the WH-5 biocarbon in Figure 5.2D denotes a primarily carbonaceous material (89.7 wt.%) with low O content (8.3 wt.%) and trace elements such as Si (0.51 wt.%) and Al (0.3 wt.%). After activation, nickel was not detected from EDS as a result of the acid washing procedure.

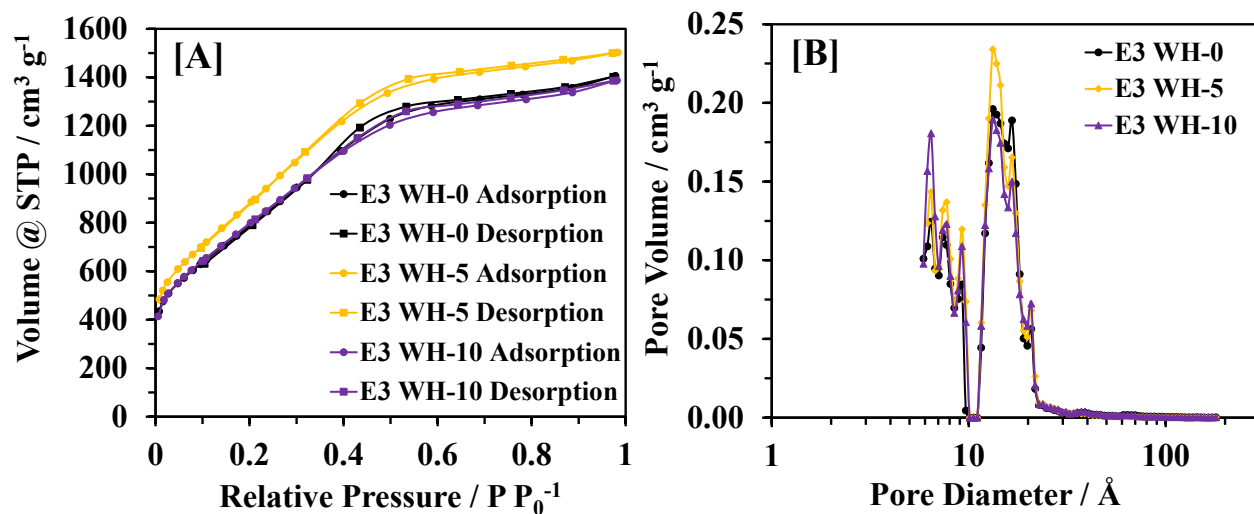


Figure 5.3. BET pore size distribution and hysteresis plot of WH-0, WH-5, and WH-10 biocarbons.

Assessment of the surface area, pore sizing, and pore volume were conducted via a N₂ nitrogen adsorption/desorption analysis. Multipoint BET methods and micropore analysis via Quantichrome software were utilized for surface area and pore size distribution calculations. BET physisorption plots (Figure 5.3A) demonstrated type IV isotherms characteristic of mesoporous adsorbents where pore networks are relatively disconnected.^[19] Mono- and multi-layer adsorption of N₂ leads to pore condensation corresponding to the final plateau detected in Figure 5.3A.^[139] Isotherms presented resemble similar characteristics to a study conducted by Sima et al (2020) where embedded Ni and N doped biocarbon was investigated for electrochemical applications.^[19] The surface areas of WH-0, WH-5, and WH-10 biocarbon were determined to be 3031, 3429, and 3062 m² g⁻¹, respectively. These large surface areas are attributed to the pre-formed hierarchical structure of the plant tissue.^[140] In WHs, vascular tissue structures, such as veins, remain in a preserved carbonized form after activation, creating macro pores.^[141] Nanometer scale structures that resemble capillaries collapse during activation and reform into new structures.^[141] It is evident that the surface area of the WH-5 biocarbon is significantly increased over other presented samples suggesting an optimized Ni loading for bio-based carbon materials. Increased surface areas are highly desirable for biocarbon electrode materials due to the increased electrode-electrolyte interfacial area which can lessen the overall resistivity of the electrode.^[19] An increase in pore volume for WH-5 biocarbon (2.13 cm³ g⁻¹) over WH-0 and WH-10 biocarbon (1.99 cm³ g⁻¹, 1.97 cm³ g⁻¹) was observed due to an increase in porosity. The pore size distribution in Figure 5.3B demonstrates micro and mesopores pores ranging from about 0.7 – 7 nm with an average pore size ($S_{p\text{ avg}}$) of 2.6, 2.5, and 2.6 for WH-0, WH-5, and WH-10 biocarbon, respectively. The majority of pore volume comes from pores ranging from 0.8 – 3 nm, which is described as ideal for biocarbon based materials.^[113] A summary of BET results is described in Table 5.2.

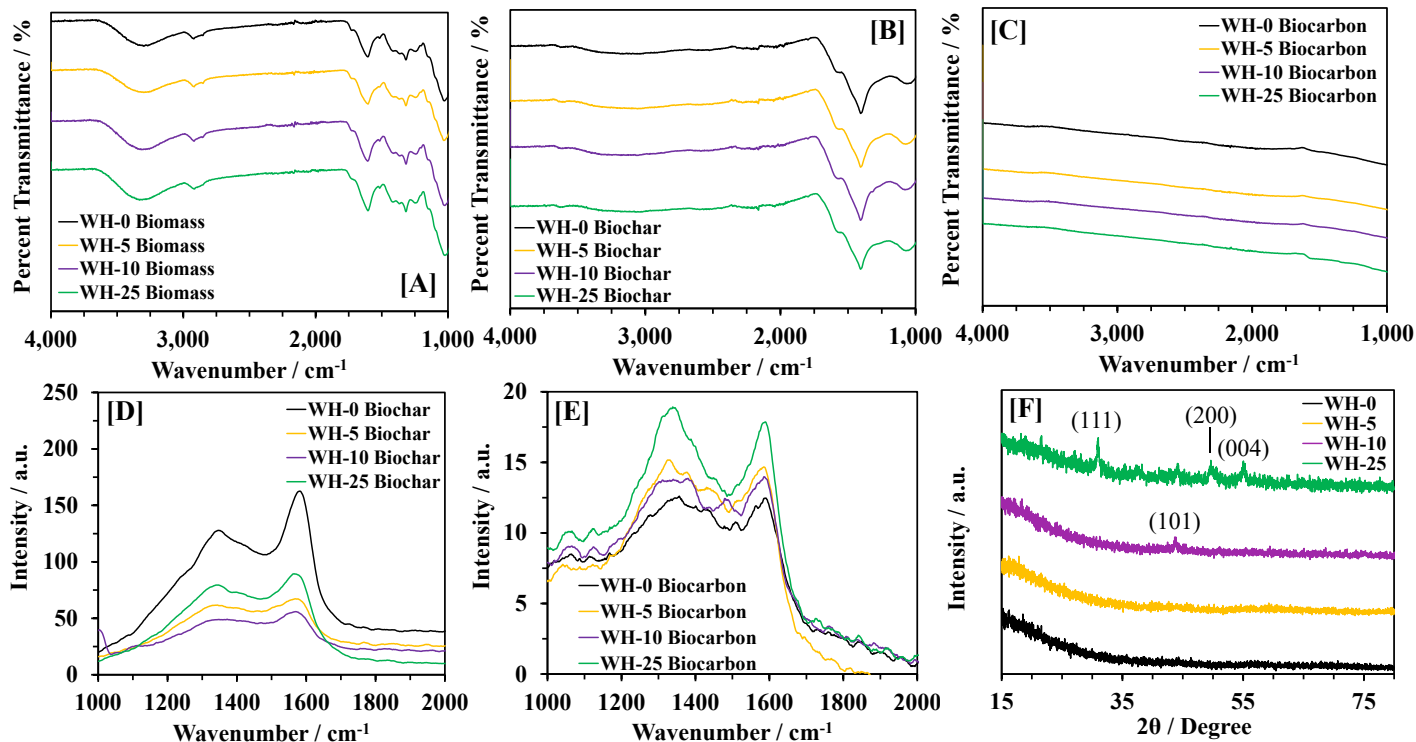


Figure 5.4. ATR-FTIR spectra of WH-0, WH-5, WH-10, WH-25 [A] biomass, [B] biochar, and [C] biocarbon. Raman spectra of WH-C, WH-5, WH-10, WH-25 [D] biochar and [E] biocarbon. [F] XRD Spectra of WH-0, WH-5, WH-10, and WH-25 biocarbon.

The WH biomass, biochar and biocarbon underwent ATR-FTIR spectroscopy (Figures 5.4A, 5.4B, 5.4C) yielding similar internal molecular results. WH biomass contained several characteristic alcohol peaks including those related to O-H stretching at $\sim 2900 \text{ cm}^{-1}$ correlating to intramolecular bonding as well as O-H bending at $\sim 1360 \text{ cm}^{-1}$. Carboxylic acid related O-H bonding is observed at ~ 3320 and $\sim 1410 \text{ cm}^{-1}$, representing O-H stretching and bending, respectively. Ketone and aldehyde related C=O stretching ($\sim 1720 \text{ cm}^{-1}$) was detected from the shoulder of the C=C (aromatic/straight chain) peak located at $\sim 1600 \text{ cm}^{-1}$. Alkyl aryl ether C-O stretching was detected at $\sim 1240 \text{ cm}^{-1}$. Described C, O, and H bonding of WH biomass is characteristic of lignocellulosic biomass where cyclic and aromatic compounds are frequently bonded to functional groups O-H,

COOH, R-C-O-C-R, C=O for lignin, hemicellulose, and cellulose. After thermal annealing at 500 °C, ATR-FTIR spectra patterns change significantly. All O-H compounds including bonded alcohols and carboxylic acids have been gasified and removed from the solid product. Instead, a pronounced shoulder, off of the S=O related sulfate peak ($\sim 1400\text{ cm}^{-1}$), is observed at ~ 1560 correlating to an increase in aromatic C=C stretching. Biocarbon resulting from the high temperature thermochemical and catalytic activation of WH biochar demonstrated cleavage of all functional groups leaving a primarily carbon structure. A weak peak at $\sim 1550\text{ cm}^{-1}$ indicates some C=C stretching involving aromatics or cyclic alkenes.

Raman spectroscopy was employed to examine the degree of graphitization for WH biochar and biocarbon samples. Raman spectra of WH biochar in Figure 5.4D and WH biocarbon in Figure 5.4E display two characteristic peaks at wavenumbers 1343 and 1574 cm^{-1} corresponding to the D and G bands, respectively. Here, the D band indicates defects within the graphitized layers of the biochar or biocarbon while the G band corresponds to ordered sp^2 hybridized -C=C- bonding within crystal lattice.^[93] By taking the ratio of intensities matching the D and G bands ($I_D:I_G$), determination of degree of graphitization, a physio-characteristic parameter, can be performed. A lower ratio indicates a higher degree of graphitization correlating to higher conductivity within the material framework. WH-0 biochar exhibited the lowest $I_D:I_G$ post thermal annealing (0.80), however WH-5 and WH-10 biocarbon exhibited the lowest $I_D:I_G$ post activation (1.00 and 1.01, respectively). All $I_D:I_G$ for biochar and biocarbon samples presented are listed in Table 5.2. When the Raman spectra is examined for molecular scale characteristics, these peaks help elucidate features such as aromatic ring bonding. D band molecular features for WH-0 biochar include alkyl ether, aryl, and para-aromatics due to the presence of the peak shoulder between 1200 and 1250 cm^{-1} , C-C bonding between aromatic rings of 6 or more which is designated by the increase of

peak intensity at 1300 cm^{-1} , and the presence of amorphous carbon structures as indicated by the peak broadening to 1465 cm^{-1} . WH-0 G band features include 3-5 bonded aromatic rings and the presence of graphitic aromatics, indicated by wavelengths of 1540 and 1590 , respectively.^[92] Alternatively, WH-10 biochar Raman spectra, which has a marked decrease in peak intensity and broader peaks, represents more amorphous bio-carbonaceous features. Attributes associated with WH-0 biochar indicate that lignocellulosic features remained intact during thermal annealing at $500\text{ }^{\circ}\text{C}$. All samples containing embedded Ni catalyst demonstrated increased amorphous structures signifying the breakdown of large complex lignocellulosic molecules during thermal annealing. Post chemical/catalytic activation at $800\text{ }^{\circ}\text{C}$, WH-5 biocarbon's Raman spectra demonstrated well defined D and G band peaks with reduced peak broadening when compared with the other biocarbon samples presented. Analysis of the D band reveals the presence of highly ordered carbonaceous molecular structures at 1300 cm^{-1} and breathing of aromatic rings at 1380 cm^{-1} . Aromatics of 3-5 rings at 1540 cm^{-1} and characteristic graphitic aromatics at 1590 cm^{-1} are observed in the G band. Raman active compounds contained within other presented biocarbon samples post 1700 cm^{-1} remain absent in WH-5 biocarbon.

Powder XRD crystallography was performed on all biocarbon samples to determine WH micro-characteristics as a result of embedded Ni. First insights into biocarbon analysis are to identify the graphitic (002) peak at $2\theta = 26^{\circ}$, representing a reflection in the graphite basal plane. In the presented samples, WH-0 and WH-5 demonstrate gaussian broad bands extending to $2\theta = \sim 35^{\circ}$, indicating the presence of amorphous carbonaceous compounds. Both of these spectra contain an absence of all other peaks, further supporting the amorphous nature of these biocarbons. Biocarbon WH-10 contained a broad gaussian peak similar to those in WH-0 and WH-5 samples, however, two small peaks became present at $2\theta = 44^{\circ}$ and 51° , corresponding to graphitic carbon (101) and

NiO (200), respectively. The (101) graphitic peak indicates a minute presence of 2H-hexagonal graphite, where the layers are stacked in an alternating ABABAB pattern.^[142] This small presence suggests a commencement to the formation of graphitic biocarbon. The NiO (200) peak in the WH-10 biocarbon sample corresponds to a face centered cubic (FCC) structure characteristic of elemental Ni.^[143] Biocarbon sample WH-25 demonstrated an abundance of peaks within the XRD spectra correlating to the presence of NaCl, NiO, Ni, and graphitic carbon. The peak located at $2\theta = 31^\circ$ directly relates to the (200) reflection of NaCl, a commonly existing compound in bio-related samples and further detailed in the presented EDS imagery. A peak at $2\theta = 38^\circ$ correlates to (111) in NiO, a common compound due to the inevitable oxidation of Ni in the presence of atmospheric conditions. Peaks denoted at $2\theta = 44^\circ$ and 55° correspond to the graphitic (101) and (004), respectively, suggesting a higher prevalence of graphitic carbon compared to previously presented samples. Similar to the WH-10 biocarbon, WH-25 demonstrates an elemental Ni (200) peak at $2\theta = 51^\circ$. The abundance of peaks presented in WH-25 biocarbon can mainly be attributed to the higher concentration of embedded Ni, described from ICP analysis, however a greater presence of Ni does not necessarily correlate to higher surface areas or pore volumes, as demonstrated from the BET analysis. Contrarily, the increased Ni content appears to have contributed to the depolymerization of lignin instead of the enhanced functional group cleaving demonstrated in lower Ni content samples, supported by Raman analysis.

Table 5.2. BET surface area, pore volume, pore size analysis, Raman I_D:I_G ratios, and percent yield for WH biochar and biocarbon.

Sample	S _{BET}	V _{BET}	S _{p avg} *	Biochar	Biocarbon	Percent Yield wt. %
	[m ² g ⁻¹]	[cm ³ g ⁻¹]	[nm]	I _D :I _G		
WH-0	3031	1.99	2.6	0.80	1.06	5.0
WH-5	3429	2.13	2.5	0.92	1.01	6.3
WH-10	3062	1.97	2.6	0.88	1.00	3.1
WH-25 [†]	-	-	-	0.90	1.07	4.7

* S_{p avg} was calculated utilizing the following equation $S_{p avg} = \frac{4V_{BET}}{S_{BET}}$

[†] Conversion process did not yield enough material for physisorption analysis

5.3.2 Electrochemical Characterization

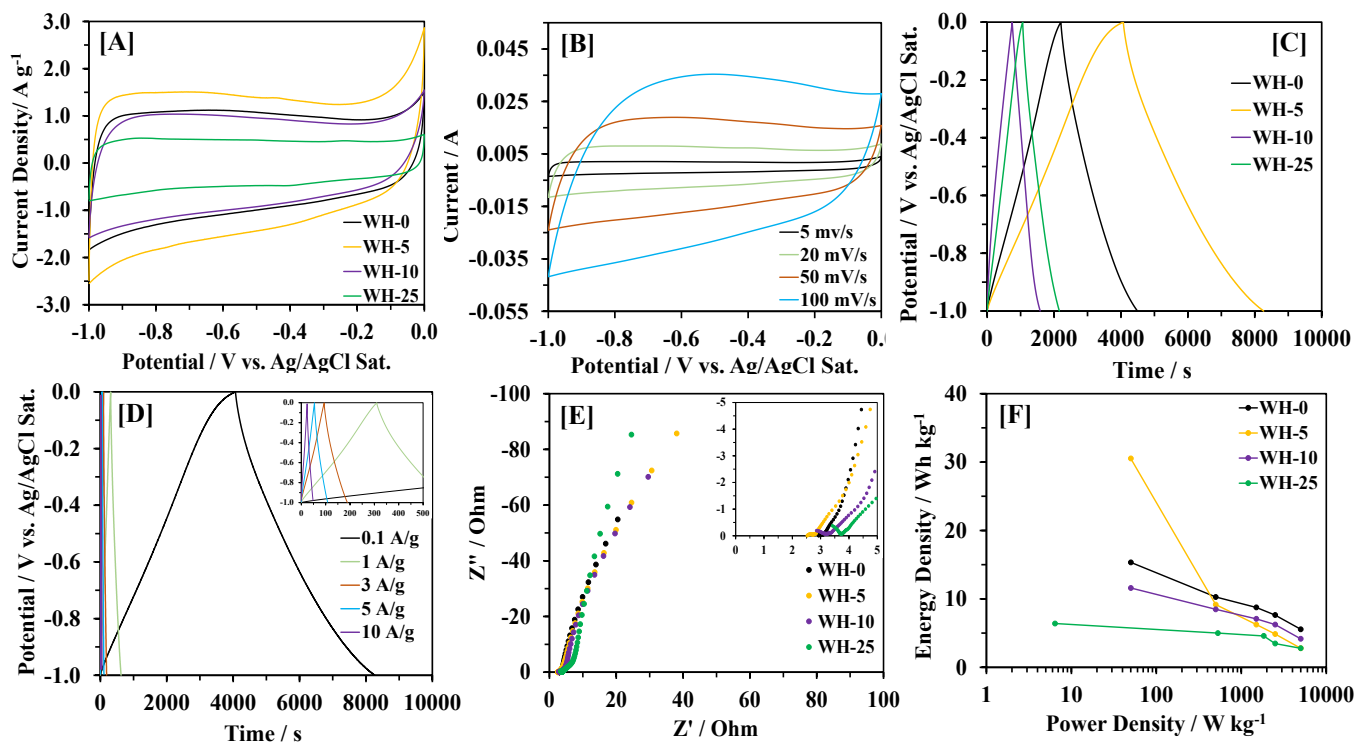


Figure 5.5. [A] CV curves of WH-0, WH-5, WH-10, and WH-25 biocarbons at a scan rate of 5 mV s⁻¹, [B] CV curves of WH-5 biocarbon at scan rates 5 – 100 mV s⁻¹, [C] CD curves of WH-0, WH-5, WH-10, and WH-25 biocarbons at 0.1 A g⁻¹, [D] CD curves of WH-5 biocarbon at current densities 0.1 – 10 A g⁻¹ (inset: CD curves of higher current densities), [E] EIS spectra and [F] power density v. energy density for WH-0, WH-5, WH-10, and WH-25 biocarbons.

Cyclic voltammetry (CV) was performed on all biocarbon samples fabricated into supercapacitor electrodes where experiments were conducted in 2 M KOH between –1 to 0 V vs Ag/AgCl (sat.). Cyclic voltammograms displayed in Figure 5.5A demonstrate smooth curves with an absence of notable peaks signifying no observable reversible or irreversible reactions, a characteristic of ideal EDLC behavior.^[118] It was observed that WH-5 biocarbon held a significantly larger area, and therefore capacitance, than all other presented samples. This is indicative of a high overall

electrochemical performance suggesting better charge transport, a high ion storage, and a low internal resistance as the main contributors. A pseudo-rectangular shape is maintained at higher scan rates (20-100 mV s^{-1}) for WH-5 biocarbon, displayed in Figure 5.5B. Preserving this shape while maintaining minimal specific capacitance loss at higher scan rates denotes ions have increased mobility within the material framework. Specific capacitance of WH biocarbon at 5 mV s^{-1} for WH-0, WH-5, WH-10, and WH-25 reached 356, 541, 264, and 159 F g^{-1} , respectively. WH-5 biocarbon reached a significantly higher specific capacitance over all other samples. In effect, the lower Ni content is beneficial for electrochemical applications due to the increased pore volumes for the WH-5 biocarbon. Moreover, a statistical analysis performed on biocarbon materials by Shell et al. (2021) demonstrated that pore volume bears one of the greatest effects on electrochemical performance, further supporting these results.^[113] The theoretical specific capacitance of activated porous carbons is 550 F g^{-1} .^[21] These results reached 98.4% of this value in a lower molarity electrolyte indicating an enhanced biocarbon structure suitable for high performance electrochemical applications. WH-5 biocarbon was able to maintain elevated specific capacitances at higher scan rates with values of 472, 400 and 336 F g^{-1} for scan rates 20, 50, and 100 mV s^{-1} , respectively. Maintaining high specific capacitance values at high scan rates is difficult and often unachievable due to decreased penetration and diffusion of ions within the material framework.^[19] Here, WH-5's specific capacitance values remained higher than many reported biocarbon derived resources, further highlighting the high performance of WH-derived materials. WH-derived biocarbons underwent further electrochemical analysis through galvanostatic charge-discharge (CD) in a three-cell system to analyze ion adsorption-desorption characteristics. CD curves displayed in Figure 5.5C demonstrated ideal 'sawtooth' shape at a current density of 0.1 A g^{-1} indicating no chemical reactions which further demonstrates EDLC ideal charge separation.

Biocarbon WH-5 achieved a significantly longer charge-discharge time correlating to a significantly higher specific capacitance of 334 F g^{-1} versus all other presented samples, agreeing with presented CV results. WH-0, WH-10, and WH-25 achieved specific capacitances of 217, 166, and 92 at the same current density. WH-5 biocarbon's CD performance was investigated at current densities ranging $1 - 10 \text{ A g}^{-1}$ (Figure 5.5D), where the specific capacitance was reduced to 203 F g^{-1} at a current density of 10 A g^{-1} . Similar principles of decreased ion penetration and diffusion discussed for CV are applicable for CD experiments. All specific capacitances are listed in Table A6.1 of Appendix A6.

EIS experiments were conducted in 2 M KOH in an open circuit potential format to gain insight into electrode resistances and characteristics associated with the electrode to electrolyte interface, charge transfer, and overall ideal capacitive behavior. The Nyquist plot is presented in Figure 5.5E and Figure 5E inset where there are three characteristic regions. The high frequency semicircle region denotes interfacial charge transfer resistance where a smaller semicircle indicates better electrical conductivity of the electrode.^[19] Here, the bulk solution resistance (R_{bsr}) and charge transfer resistance (R_{ctr}) can be calculated. The medium frequency region denotes the ion diffusion from the electrolyte to the electrode surface and is called the Warburg resistance.^[121] A slope of 1 or a 45° degree angle (S_{wi}) is ideal for supercapacitor applications. The low frequency region corresponds to ideal capacitive behavior where a 90° angle or large slope (S_i) is desired.^[122] Interestingly, despite WH-5 biocarbon's excellent electrochemical performance, it was not superlative over other presented materials. For WH-5 biocarbon, the R_{bsr} was the lowest at 2.53Ω , whereas for WH-C, the R_{ctr} was the lowest at 0.16Ω . WH-5, WH-10, and WH-25 biocarbon attained an R_{ctr} value of $0.21, 0.37, 0.37 \Omega$, respectively. WH-10 biocarbon's Warburg impedance was the 0.99 , the closest of all samples to 1, corresponding to enhanced ion diffusion within the

material framework. Biocarbon WH-25 was found to have the highest slope in the low frequency region at 3.53 denoting ideal capacitive behavior. All denoted resistances and slopes are presented in Table 3. EIS analysis signifies excellent charge transfer and conductivity of WH biocarbon materials within fabricated electrodes.

Table 5.3. Summary of electrochemical results.

Sample	Specific Capacitance	R _{bsr}	R _{ctr}	S _{wi}	S _i	Energy Density
	[F g ⁻¹]	[Ω]	[Ω]	-	-	[Wh kg ⁻¹]
WH-0	356	2.93	0.16	1.64	3.39	15.3
WH-5	541	2.53	0.21	1.45	2.61	30.5
WH-10	264	2.86	0.37	0.99	2.92	11.6
WH-25	159	3.42	0.31	1.10	3.53	6.4

Energy storage capabilities are shown in Figure 5.5F in the form of energy density versus power density. WH-5 biocarbon achieved a high energy density of 30.5 W h kg⁻¹ at a power density of 50 W kg⁻¹. As the current density increases to 10 A g⁻¹, the energy density of WH-5 biocarbon diminishes significantly to 2.78 W h kg⁻¹, however, the power density increases 10-fold to 5000 W kg⁻¹, which can be attributed to the high transport of ions which limits diffusivity into the material. Stability studies were conducted on WH-5 biocarbon where the material was fabricated into a coin cell supercapacitor (CR2032) and CD was performed for 10,000 cycles at a current density of 2 A g⁻¹. A capacitance retention of 100 % was calculated and cycles are denoted in the Appendix (Figure A7.4). These results indicate that WH-5 biocarbon achieved high electrochemical performance with supporting physical characteristics desirable for supercapacitor applications. A comparison of results from this study to literature is provided in Table 5.4.

Table 5.4 Comparison of various activated biocarbons for supercapacitor applications.

Material	Activation Method	SSA m ² g ⁻¹	Pore Volume cm ³ g ⁻¹	Specific Capacitance F g ⁻¹	Rate	Electrolyte	Reference
Water Hyacinth	Phytoremediation /KOH	3429	2.13	541	5 mV s ⁻¹	2 M KOH	This work
Water Hyacinth	Phytoremediation /KOH	2755	2.07	552	5 mV s ⁻¹	6 M KOH	[19]
Corn Stover	Thermal	215	0.12	242	5 mV s ⁻¹	2 M KOH	[113]
Chinese Dates	Thermal/KOH	1941	0.85	518	0.5 A g ⁻¹	6 M KOH	[144]
Bamboo	Thermal/KOH	2221	1.24	293	0.5 A g ⁻¹	3 M KOH	[145]
Pea Protein	KOH	3500	1.76	413	1 A g ⁻¹	1 M KOH	[146]
Kelp	Thermal/NH ₃	400	0.62	440	0.5 A g ⁻¹	6 M KOH	[147]
Coconut Shell	FeCl ₃ /ZnCl ₂	1874	1.21	268	1 A g ⁻¹	6 M KOH	[148]
Corn Cob	Thermal/KOH	3054	1.50	328	0.5 A g ⁻¹	6 M KOH	[149]
Algae	Thermal/KOH	1338	0.60	353	1 A g ⁻¹	2 M KOH	[150]

5.4 Conclusions

Water hyacinth was cultivated in a hydroponic system with various concentrations of Ni²⁺ to assess the impacts of bio-absorbed nickel on biocarbon for supercapacitor applications. ICP-OES revealed a strong presence of bio-absorbed nickel in the biomass. The bioconcentration factor indicates strong bioaccumulation of WH grown in Ni-doped aqueous media. WH-5 biocarbon demonstrated the highest electrochemical performance of presented samples with a specific capacitance of 541 F g⁻¹ and 100% capacitance retention over 10,000 cycles. The high electrochemical performance of this material is attributed to the large S_{BET} of 3429 m² g⁻¹, high V_{BET} of 2.13 cm³ g⁻¹, and optimal pore structure with S_{p avg} of 2.5 nm. Raman and XRD analyses revealed that the inclusion of molecularly embedded nickel promotes increased bond cleaving and

facilitates the depolymerization of lignocellulosic components within the biomass during the thermal treatment. The organic composition of water hyacinth, hyperaccumulated nickel, and catalytic/chemical activation techniques presented herein have enabled the identification of one of the most efficient and sustainable biocarbon precursors available. This work provides a sustainable low-cost method of synthesizing high quality biocarbon capable of achieving 98% of theoretical capacitance.

Chapter VI. Graphitized Biocarbon Derived from Hydrothermally Liquefied Low Ash Content Corn Stover

Katelyn M. Shell, Vinod S. Amar, Julian A. Bobb, Sergio Hernandez, Rajesh V. Shende, and Ram B. Gupta.

Abstract

Graphitized biocarbon can be utilized for energy storage applications such as supercapacitors. The scientific community has geared its attention to obtain such value-added product from abundantly available and low-cost biomass feedstock agricultural residues such as corn stover. Lignocellulosic components embedded within the cell wall of biomass substrates can provide a fine template for enhanced ion storage, transport, and rate capabilities, desirable for electrochemical storage. Presented is the utilization of homogenized low ash content corn stover milled and sieved to desired specifications, which underwent catalytic hydrothermal liquefaction in the presence of $\text{Ni}(\text{NO}_3)_2$ at 275 °C. The hydrochar obtained by solid residue extracted from the reaction slurry was washed to acid neutral and subjected to chemical activation using ZnCl_2 , followed by thermal annealing at 400 °C for morphological and pore enhancement. Thermal carbonization was performed on acid neutralized hydrochar at 815 °C to further enhance pore structures and increase graphitization for improved conductivity. Catalytic materials exhibited a specific capacitance of 316 F g^{-1} and held a 100% retention beyond 10,000 cycles. BET, Raman, XRD, cyclic voltammetry, chronopotentiometry, and EIS analyses of the material are discussed herein.

Keywords: hydrochar, biocarbon, graphitization, hydrothermal liquefaction, supercapacitors.

6.1 Introduction

To satisfy the proliferating global energy demands, there is an imperative need to explore advanced energy storage materials from renewable and sustainable sources, such as agricultural residues, and fabricate them into electrochemical devices such as supercapacitors. Due to their excellent cyclability ($> 10,000$ cycles), great stability, and good power density ($10^2 - 10^5 \text{ W kg}^{-1}$), these unique devices are capable of facilitating rapid adsorption/desorption of ions which in turn is a major attribute for prevalence to commercial applications such as regenerative braking.^{[10],[74]} Electrochemical double layer capacitors (EDLCs) are one type of supercapacitor consisting of two identical electrodes with a permeable membrane in between. Capacitance occurs when ions are stored on the surface through an applied voltage, creating an electrostatic charge separation.^[75] Material surface area and porosity play an important role in the capacitive nature of EDLCs. Micropores ($< 2 \text{ nm}$) below 0.7 nm are generally not viable for ion storage, but increases surface areas considerably. The lower end of the mesopore range ($2 - 50 \text{ nm}$) contributes significantly to overall capacitance, while the ideal average pore size (P_{avg}) is described to be between ($0.8 - 3 \text{ nm}$). Macropores ($> 50 \text{ nm}$) increase wettability, decreasing resistances at the electrode-electrolyte interface. Inclusion of all of these aspects generate high performance and desirable materials for supercapacitor applications.

Agricultural residues such as corn stover are abundantly available which can be readily processed into value added carbonaceous products such as hydrochar. Corn stover is comprised of several components of the corn plant, such as stalks, stems, leaves, cobs, and husks, and contains higher concentrations of lignocellulosic compounds such as lignin, cellulose and hemi-cellulose which serves as an excellent template for biomass-derived biocarbons, suitable for electrochemical applications.^[151] This is due to the abundance of functional groups, such as amines, alcohols,

esters, carboxylic acids etc., that when cleaved, form the desired pore structures discussed earlier. The complex polymeric nature of corn stover makes acidic or alkaline pretreatment processes, followed enzymatic hydrolysis for bioethanol production, necessary to expose and cleave the desired lignin, cellulose, and hemicellulose components.^[87]

Following pretreatment, the biomass feedstock can be thermochemically treated to obtain biochar via pyrolysis, gasification or hydrothermal liquefaction.^{[102],[152]–[154]} During pyrolysis the biomass feedstock is rapidly heated in the absence of air to temperatures ranging from 400 to 600 °C and can produce bio-oil which is mainly composed of oxygenated hydrocarbons and can be used as a biofuel additive and solid-carbonous residue charcoal has a high content of fixed carbon (>75%).^{[155]–[157]} During the biomass gasification, the biomass feedstock is gasified at high temperatures of 500-1400 °C to produce syngas (comprising CO, H₂, CH₄ and light hydrocarbons carbon monoxide, hydrogen and carbon dioxide), tar and char.^[158] Since biomass naturally occurs in wet residue form, hydrothermal processing is a favored technique to process the moist agricultural residues, such as corn stover. The biomass is further diluted with water and/or organic solvent and the reaction is hydrothermally carried out at moderate temperatures (300 – 350 °C) and sufficiently high pressures (15.9 – 20.7 MPa).^{[159]–[161]} Technical challenges associated with this technology include mixing, pressurization, transport, and pressure decrease of high solid slurries, but also understanding the relationship between crude oil product properties and feedstock composition.^{[80],[107],[108]} Other challenges include optimization of the liquefaction process variables; demonstration of separation techniques; and demonstration of bio-oil upgrading processes to produce a product with marketable commercial value.^{[101],[162]–[165]}

In the recent decade, significant efforts have been made to introduce carbonate/hydroxide type catalysts in HTL processing to increase the conversion of biomass. However, homogeneous

transition metal catalysts have been less explored for HTL compared with carbonate or hydroxide catalysts. Song et al. performed HTL of corn stalk in the absence or in the presence of 1 wt.% Na_2CO_3 at 276 °C, 25 MPa, and observed bio-oil yield increase from 33.4 wt.% to 47.2 wt.%.^[166] Karagoz et al. tested a series of homogeneous catalyst for HTL of pinewood sawdust at 280 °C for 15 min and showed the liquefaction of biomass followed the trend $\text{K}_2\text{CO}_3 > \text{KOH} > \text{Na}_2\text{CO}_3 > \text{NaOH}$ with maximum of 96 wt.% conversion.^[162] The use of 10 wt.% of Rb_2CO_3 and $\text{Ba}(\text{OH})_2$ for HTL of sawdust and cornstalks was found to significantly increase both phenolic oil (53 wt.%) and gas yield (25 wt.%).^[167] It is also believed the homogeneous catalysts can promote H_2 production by water-gas shift fraction.^[168] Influence of K_2CO_3 on gasification of glucose has been reported indicating significant effect on water-gas shift fraction.^[169] Transition metal homogeneous catalyst such as $\text{Co}(\text{NO}_3)_2$, $\text{Ni}(\text{NO}_3)_2$ and $\text{Fe}(\text{NO}_3)_2$ used for hydrothermal liquefaction was only reported by our research group. The HTL of pinewood at 225 -300 °C, using $\text{Ni}(\text{NO}_3)_2$ as catalyst, achieved a maximum of 12.26 mol % of H_2 at 275 °C and the highest biocrude production (55 wt.%) was obtained at 250 °C.^[102] HTL derived biochar/hydrochar is generally amorphous and require high temperature thermal processing (> 500 °C) in order to form graphitized layers. These graphitized layers provide enhanced charge-transfer capabilities by reducing ohmic resistances within the material framework.^[113] Post-processing, the resulting graphitized, porous and conductive biocarbon is suitable for electrochemical applications.

Due to the commercial prominence of biocarbon for energy storage applications, in this research we focus on obtaining biochar derived from hydrothermal liquefaction (HTL) and uniquely improving its morphological properties via hybrid chemical/catalytic and thermal activation process. As obtained corn stover is converted to hydrochar via catalytic hydrothermal liquefaction in the presence of $\text{Ni}(\text{NO}_3)_2$ catalyst at 275°C and its morphological properties such as surface

area, pore volume and diameter were enhanced in the presence of ZnCl_2 , followed by thermal activation. Biochar underwent thermal carbonization to enhance pore structures and graphitization, conducive for electrochemical applications. Physical and electrochemical characterizations, such as BET, ATR-FTIR, Raman, XRD, cyclic voltammetry and chronopotentiometry, will be discussed to give fundamental insights into biocarbon enhancement and effect on electrochemical performance.

6.2 Materials and Methods

6.2.1. Materials

Milled Corn stover was sourced from Story County, Iowa using a multi-pass harvest technique in the fall of 2015 and was shipped to Idaho National Laboratory (INL) for pre-processing in INL's Biomass Feedstock National User Facility. Acetone, hydrochloric acid (HCl, 1 M) and ethanol ($\text{C}_2\text{H}_5\text{OH}$, 95 wt.%) were purchased as analytical grade from Fisher Scientific (MA, USA). Polytetrafluoroethylene (PTFE, 60 wt.% dispersed in water) and potassium hydroxide (KOH, 90 wt.%) were purchased from Sigma-Aldrich (MO, USA). ACS grade (99.99%) nickel (II) nitrate hexahydrate ($\text{Ni}(\text{NO}_3)_2 \cdot 6\text{H}_2\text{O}$), and reagent grade (> 98 %) zinc chloride (ZnCl_2) were purchased from Sigma Aldrich (MO, USA). Carbon black (Super P conductive, 99+ wt.%) were purchased from Alfa Aesar (MA, USA). Ultra-high purity (grade 5.0) argon was purchased from Airgas (PA, USA). Milli-Q (18.2 M Ω) water was obtained from an on-demand Barnstat filtration system. N_2 gas with minimum purity of 99 % was purchased from A & B Welding Company (SD, USA). Distilled de-ionized (DI) water was used to prepare the biomass slurry. Nickel foam substrates and coin cells (CR2032) were purchased from MTI Corporation (CA, USA). Henkel Loctite Hysol 9462 epoxy adhesive was purchased from Ellsworth Adhesives (WI, USA).

6.2.2 Corn Stover pre-processing

Corn stover bales were milled into two stages using a Vermeer HG200 diesel hammer grinder equipped with a 25 mm screen for the first stage and a Bliss ED-4424-TF electric hammermill equipped with a 6 mm screen for the second stage. The nominal processing rate of the combined drying and grinding operations was approximately 1.0 ton hr⁻¹.

6.2.3 Conversion of corn stover to biochar via HTL

A hydrothermal liquefaction (HTL) process was used to convert the low-ash content corn stover to value added products such as biochar, biooil, lactic acid and phenol in a Parr reactor. Details of the conversion process were given elsewhere (cite our HTL papers).^{[54],[170],[171]} The HTL reaction was carried out at a temperature of 275 °C, initial N₂ pressure of 100 psig., 2 hours reaction time, 1:10 biomass to solvent (water) mass ratio in the presence of Ni(NO₃)₂ catalyst at 5 wt.% (by dry mass) concentration. Throughout the conversion process, anaerobicity in the reaction chamber is maintained by continually purging the contents in the reactor with industrial grade N₂ for 20 min and the stirring rate of the Parr reactor was fixed to 1300 rpm. Following the reaction, the contents in the reactor were cooled using an inbuilt internal recirculating loop within the reaction vessel for all experiments. The biocrude slurry was recovered through a series of filtration and extraction steps where the biocrude, bio-oil and solid-residue (biochar) were separated at individual steps. Thus, obtained biochar was washed to a neutral pH and dried in a conventional oven at 65 °C.

6.2.4 Catalytic and thermal activation of biochar

The morphological properties of the pH neutralized biochar particles derived from HTL of corn stover can be improved by activating the reactive sites with ZnCl₂ catalyst and improving specific surface area via thermal activation. As obtained pH-neutral biochar from HTL of corn stover is

mixed with H₂O and ZnCl₂ catalyst in 1:6:1 ratio by mass and the mixture is stirred at 100 °C for 4 h followed by thermal activation at 450 °C for 2 h. The resultant biochar is treated with dilute HCl for removing the residual catalyst and impurities. Thus, obtained biochar is used for biocarbon synthesis via graphitization process as explained in Section 2.5. The schematic of the biomass conversion process followed by catalytic and thermal treatment of biochar is shown in the Figure 6.1.

6.2.5 Biocarbon Synthesis and Electrode Fabrication

As received biochar underwent a standard acid wash procedure detailed by Shell et al. (2021) prior to thermal carbonization where 1.0 M HCl was employed to remove metal contaminants.^[113] Once dried, biochar samples were carbonized at 815 °C under inert atmosphere for 3 h at a ramp rate of 5 °C min⁻¹. Contents were cooled naturally and promptly removed for characterization and electrode fabrication. Electrode ink was prepared using an 8:1:1 mass ratio of prepared biocarbon, Super P, and PTFE. A small amount of water was added to form a slurry. Slurries were evenly distributed on reduced nickel foam electrodes (3 cm²), dried at -10 psig for 16 h, then pressed, templated, and insulated using chemical resistant epoxy. Epoxied electrodes were allowed to cure overnight prior to electrochemical characterizations. Coin cell fabrication utilized two identical circular electrodes coated with prepared slurry, filter paper separator, and 150 µL of 2 M KOH pressed inside of a CR2032 case. Active mass calculations were performed using image geometric area ratios. Figure 6.1 shows overall methods in the form of a block flow diagram (BFD)

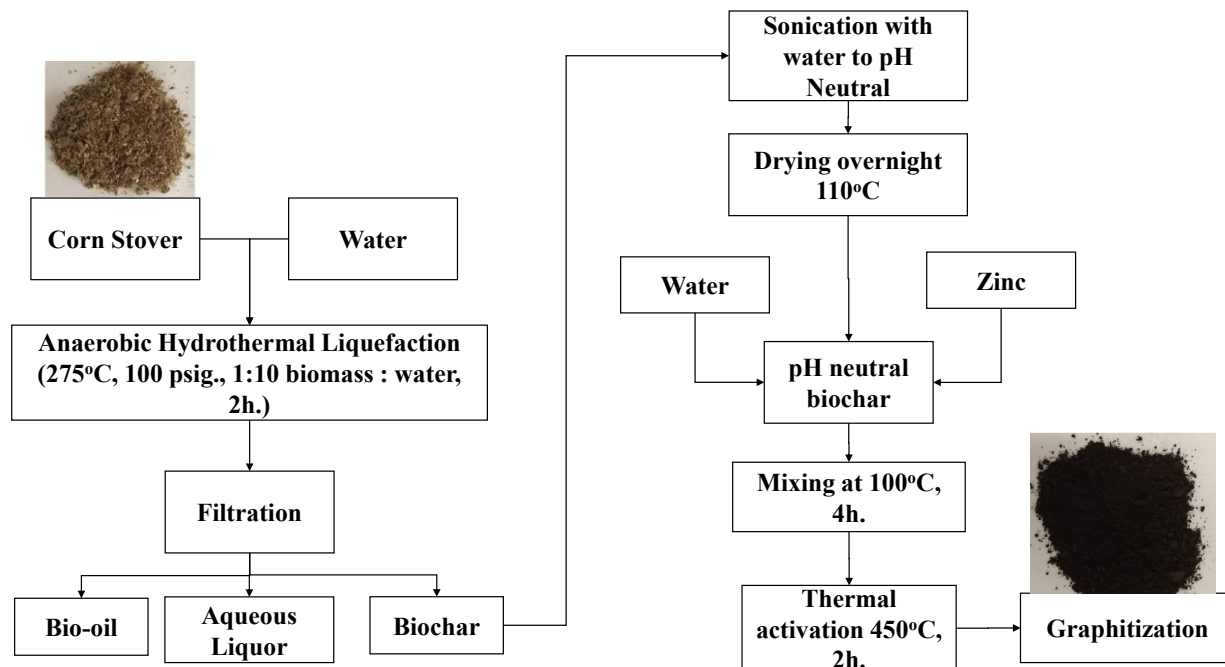


Figure 6.1. Anaerobic HTL conversion of Corn Stover to biochar and its activation via ZnCl_2 at 450 °C.

6.2.6 Characterizations

Characterization of pre-processed Corn Stover

The feedstock samples were prepared for analytical characterisation with an Ultra Centrifugal Mill ZM 200 using a 200 μm screen at 8000 rpm (Retsch GmbH). A thermogravimetric method using ASTM D7582-15 was used for proximate analysis. For moisture content, the LECO Thermogravimetric Analyser (TGA) 701 was heated to 107°C and held until a constant mass was reached under a nitrogen flow of 10 standard litres per minute (slm). The crucibles were capped with ceramic covers, and the temperature was then ramped to 950 °C and held for 7 min to determine volatiles content. Ash content was determined by cooling the instrument to 600 °C, removing the covers, and switching the gas to a flow of 3.5 slm of oxygen. The temperature was then increased to 750 °C and held until a constant mass was reached. Fixed carbon was calculated

from the weight loss during the ashing step. Ultimate analysis of the feedstocks, using a LECO TruSpec CHN and S add-on module, was conducted using a modified ASTM D5373-16 method (Flour and Plant Tissue Method) to accommodate biomass samples that use a slightly different burn profile of 4 slm for 40 s, 1 slm for 30 s, and 4 slm for 30 s of UHP O₂. Elemental sulphur content was determined using ASTM D4239-17, and oxygen content was determined by difference of the other constituents from 100 %. Heating values (high heating value, HHV, and low heating value, LHV) for the feedstocks were determined with a LECO AC600 Calorimeter using ASTM D5865-13.

Physical characterizations of Biocarbon: Surface areas (S_{BET}), pore size distributions, and average pore size (P_{avg}) were determined by nitrogen adsorption-desorption measurements using the Brunauer–Emmett–Teller (BET) method with a Quantichrome NOVA 2400e analyzer and software. Degassing was performed at 150 °C for 15 h prior to adsorption-desorption experiments. Attenuated total reflectance Fourier-transform infrared (ATR-FTIR) spectroscopy was carried out using a Thermo Fisher Scientific Nicolet iS10 infrared spectrometer with a total of 8 scans per sample. Raman spectroscopy was performed on a Thermo Scientific DXR SmartRaman spectrometer (532 nm) with sampling range of 100 to 3400 cm⁻¹. Nanographite planar size (L_a) was calculated by utilizing Equation 6.1. Derivation of the planar size equation is given by Cancado et al. (2006). Crystallinity of the biochar and biocarbon samples was examined by X-ray diffraction (XRD) using a Rigaku MiniFlex II X-ray diffractometer with a Cu K α radiation source, scan speed of 1.0° min⁻¹, sampling width of 0.01°, a voltage of 30 kV at 15 mA, and wavelength of 1.54 Å. Crystallite size and interplanar distance were calculated utilizing Scherrer's equation and Bragg's Law.

$$L_a = 2.4 * 10^{-10} (\lambda^4) \left(\frac{I_d}{I_g} \right)^{-1} \quad (6.1)$$

Where λ is the wavelength, I_d is the intensity of the D band, and I_g is the intensity of the G band in the Raman spectra.

Electrochemical Characterizations: Electrochemical characterizations were performed on an electrochemical workstation (CH Instruments, CHI 660E) in 2 M KOH. A 3-cell setup consisting of a fabricated electrode, saturated Ag/AgCl reference electrode, and Pt wire counter was utilized for cyclic voltammetry (CV, -1 – 0 V), chronopotentiometry (CP, -1 – 0 V), and electrochemical impedance spectroscopy (EIS, 0.01-100,000 Hz). Specific capacitances for CV and CP were calculated utilizing equations 6.1 and 6.2, respectively.

$$C_{S,CV} = \frac{\int_{V_i}^{V_f} I dV}{m v (V_f - V_i)} \quad (6.2)$$

$$C_{S,CP} = \frac{I t}{m (V_f - V_i)} \quad (6.3)$$

Where V_i and V_f are the endpoints of the voltage window, I is the current in A, m is the active mass of the electrode in g, v is the scan rate in mV s⁻¹, and t is the time to charge in s.

The fabricated coin cell supercapacitor underwent CP performance testing at 0.5 A g⁻¹ for 10,000 cycles. Specific capacitances used for capacitance retention calculations were calculated from Equation 6.4.

$$C_{S,CPc} = \frac{i t^*}{m (V_f - V_i)} \quad (6.4)$$

Where t^* is the time to discharge in seconds.

6.3. Results and Discussion

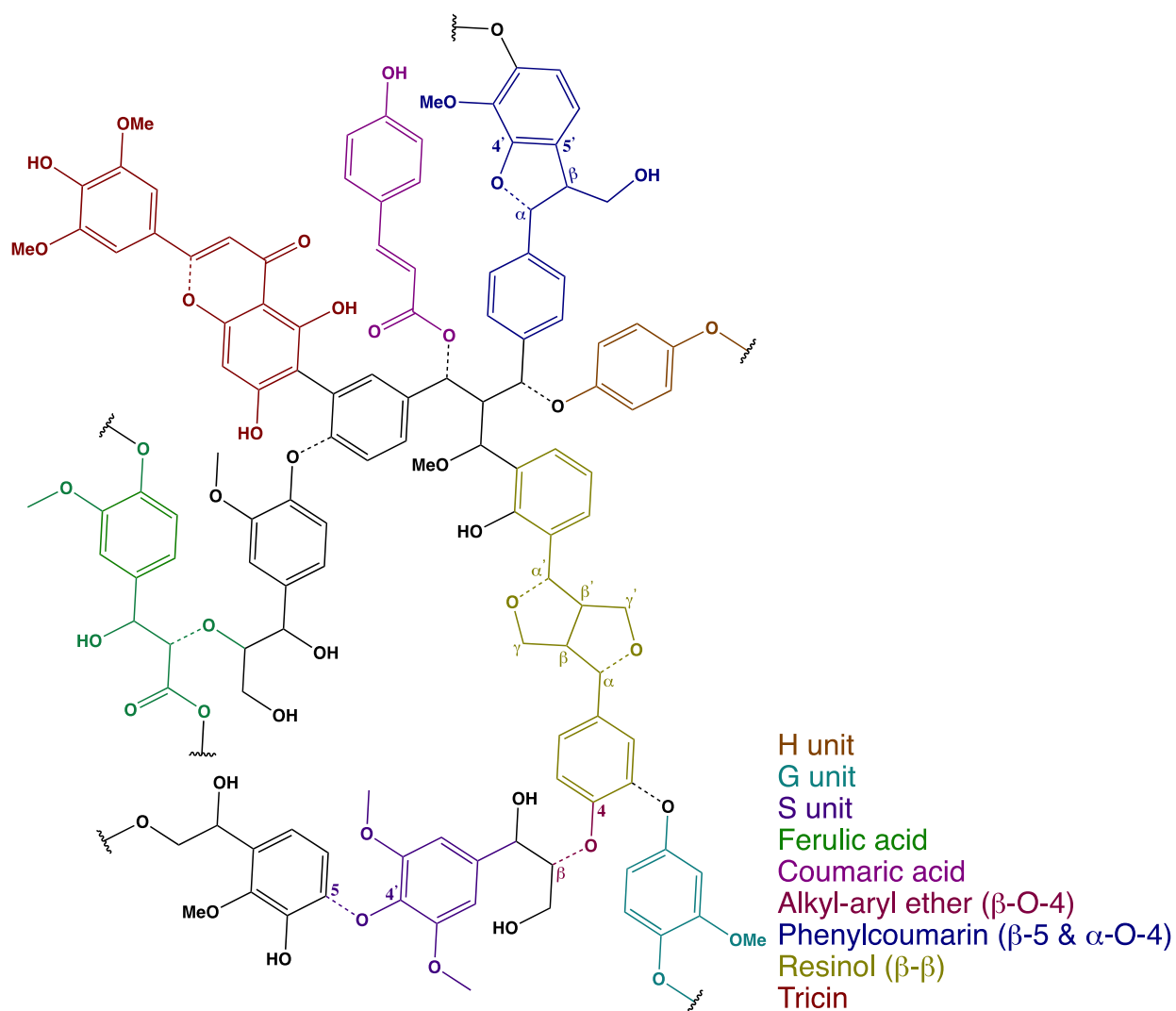


Figure 6.2. Hypothetical molecular representation of lignin with linkages and subsequent products.

The basic structural units of lignin (Figure 6.2) are derived from three phenylalanine monomers, *p*-coumaryl, coniferyl, & sinapyl alcohols, and differ based on the degree of methoxylation of their aromatic rings.^[172] These incorporated monolignols facilitate the growth of the lignin polymer as a racemic macromolecule through combinatorial free-radical coupling reactions which then results

in the *p*-hydroxyphenyl (H unit), guaiacyl (G unit) and syringyl (S unit) in the polymer, Figure 6.2.^{[172],[173]} Herbaceous biomass such as corn stover generally have lower S/G ratios (~0.62), *p*-coumaric acid (~20 %), ferulic acid (~10 %), triclin and hence, lower C–O bonds as compared to soft and hard woods.^{[114],[172],[174]} Corn stover biomass also contains inter-unit linkages such as the alkyl-aryl ether (β -O-4), phenylcoumarin (β -5 and α -O-4), resinol (β - β), and the 4-O-5.^[174] The structural characteristics normally changes during hydrothermal liquefaction of corn stover biomass. Hydrochar which is carbon-rich, liquid by-products (bio-oil), and small amounts of gaseous products such as hydrogen, methane, carbon monoxide, & carbon dioxide are usually generated.^{[175],[176]} The liquid by-products are produced from the hydrolysis of hemicellulose, cellulose, and lignin resulting in sugar-derived and lignin derived compounds.^{[176],[177]} The lignin derived compounds are phenolic monomers and oligomers resulting from the cleavage of the aforementioned C–O bonds and the more refractory C–C bonds making them more challenging to break; in addition to the easily broken C–O ester bonds from coumaric acid and ferulic acid. The bond dissociation energies for β -O-4, α -O-4 and 4-O-5 is 54 – 72 kcal mol⁻¹, 50 – 56 kcal mol⁻¹ and 78 – 83 kcal mol⁻¹, respectively.^{[178],[179]} Whereas, the bond dissociation energies for β -5 and β - β are 54 – 63 kcal mol⁻¹ and 81 kcal mol⁻¹, respectively.^{[178],[179]}

The presence of nickel ions during the catalytic hydrothermal liquefaction of corn stover has facilitated in a more efficient deconstruction of the biomass and higher bio-oil yield and lesser hydrochar yield. This is due to reductive pathways facilitated by hydrogen gas being generated from biomass depolymerization.^{[114],[180]} The presence of the nickel catalyst stabilizes reactive intermediate species during lignin bond cleavages such as the aryl-ether bond.^[114]

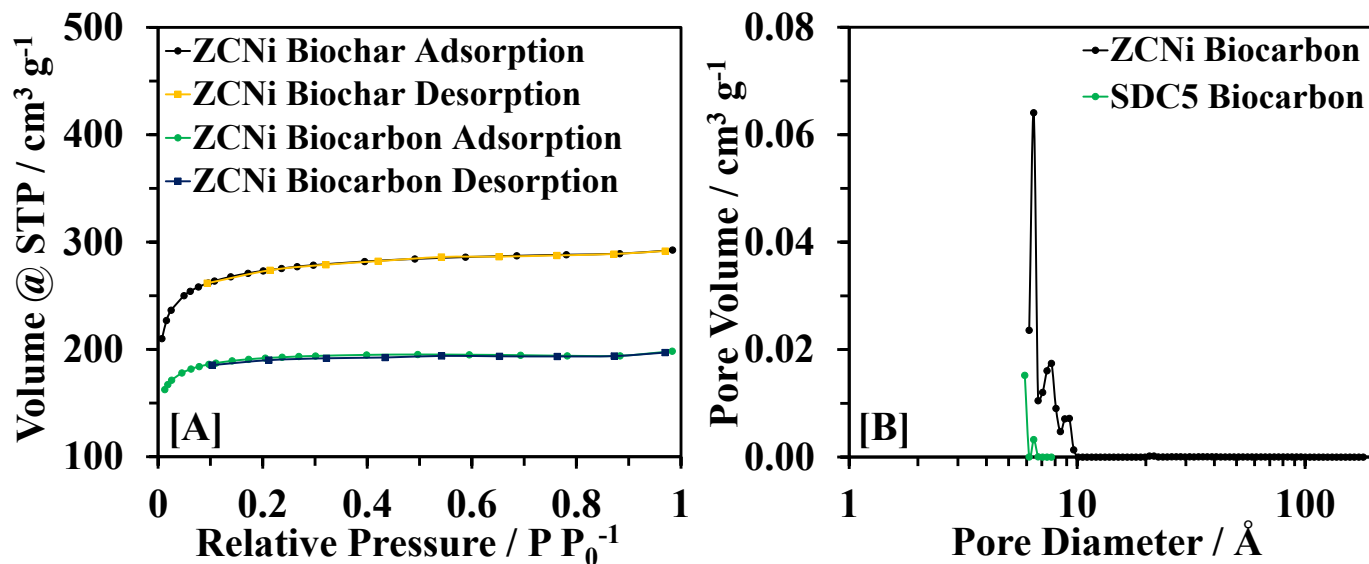


Figure 6.3. [A] Isotherms and [B] Pore size distribution of ZCNi and SDC5 biocarbons.

Nitrogen adsorption-desorption experiments were performed to assess material surface area and porosity and gain insight into physical parameters that effect electrochemical performance. Quantichrome software was utilized for performing Multipoint BET methods with micropore analysis as well as surface area and pore size distribution calculations. The zinc chloride/nickel nitrate catalyst (ZCNi) biochar and biocarbon demonstrated Type I(b) isotherms (Figure 6.3A), characteristic of microporous mediums containing a broader pore size distribution (< 2.5 nm) versus Type I(a) isotherms (< 1 nm).^[139] A steep uptake in volume at low P/P_0 indicates enhanced adsorbent-adsorptive interactions in micropores of molecular dimensions and causes micropores to quickly be filled.^[139] ZCNi biochar obtained S_{BET} of $1060 \text{ m}^2 \text{ g}^{-1}$ with a V_{BET} of $0.40 \text{ cm}^3 \text{ g}^{-1}$ while ZCNi biocarbon obtained an S_{BET} of $753 \text{ m}^2 \text{ g}^{-1}$ with a V_{BET} of $0.27 \text{ cm}^3 \text{ g}^{-1}$. Though the ZCNi biochar obtained a higher surface area and pore volume, this does not necessarily indicate that the biochar would have enhanced electrochemical characteristics. Conductivity plays a key role in capacitive behavior, thus affecting the specific capacitance. Key differences in the ZCNi biochar and biocarbon are discussed further in the Raman and electrochemical analyses. SDC5

biocarbon's S_{BET} and V_{BET} were significantly reduced comparative to ZCNi biocarbon at $140 \text{ m}^2 \text{ g}^{-1}$ and $0.22 \text{ cm}^3 \text{ g}^{-1}$, respectively. ZCNi biocarbon's increase in surface area and pore volume ultimately affects the overall specific capacitance during electrochemical operation as it provides a larger interfacial area for electrolyte ions to penetrate.^[19] Catalysts enhance the cleaving of functional groups, leaving behind pores, thus increasing porosity and surface area validated by ZCNi biocarbon. The pore size distribution in Figure 6.3B illustrates the pore size at which a certain volume of gas is adsorbed. It is clear ZCNi biocarbon exhibits a marked increase in pore volume at lower pore widths compared to SDC5 biocarbon. An ideal pore size range is described to be between 0.8 – 3 nm where, ZCNi obtained a calculated S_{avg} of 1.43 nm.^[14] SDC5 biocarbon a obtained a significantly higher S_{avg} of 6.29 nm, far removed from the ideal range. The enhanced BET results pertaining ZCNi biocarbon establishes the necessity of catalytic activators during biomass processing. All BET results are summarized in Table 6.1.

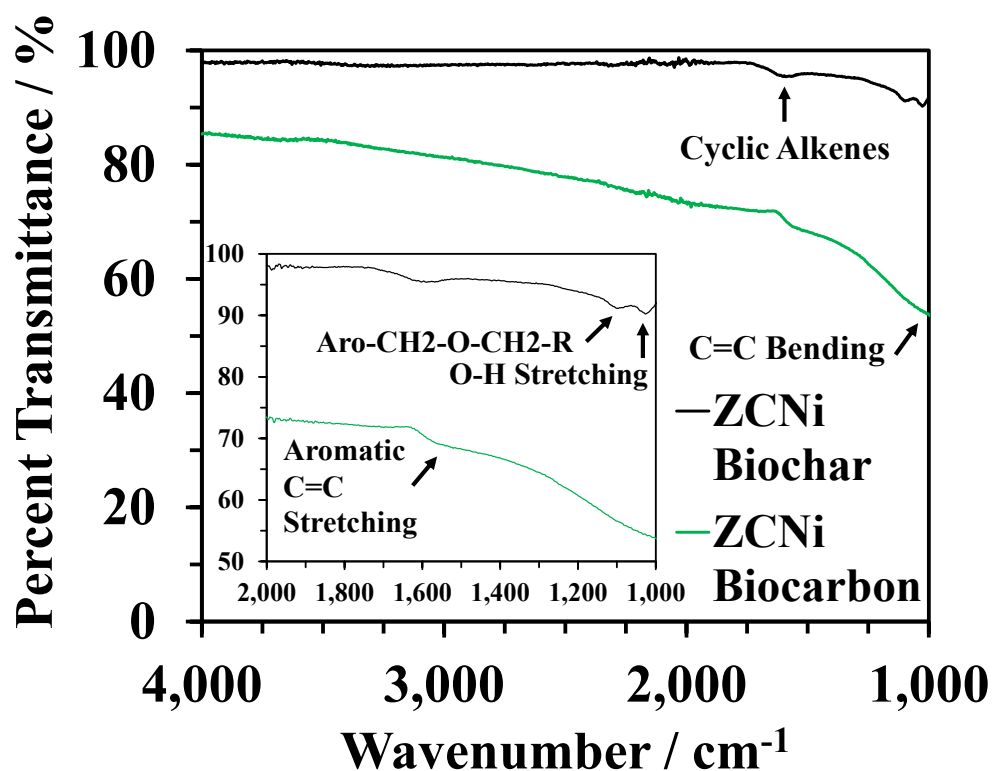


Figure 6.4. ATR-FTIR of ZCNi biochar and biocarbon with emphasis on wavenumbers between 1000 – 2000 cm^{-1} (inset).

The biochars and biocarbons were analyzed with ATR-FTIR spectroscopy (Figure 6.4) to determine functional groups of received biochar and the effect high temperature carbonization on cleaving these groups. ZCNi biochar contained C-O stretching from aliphatic ethers (Aromatic- $\text{CH}_2\text{-O-CH}_2\text{-R}$) determined from peaks located at 1024 and 1095 cm^{-1} . Additionally, the ZCNi biochar spectra contained a peak at 1599 cm^{-1} correlating to cyclic alkenes, characteristic of lignocellulosic compounds. Post carbonization, these groups are cleaved resulting in a primarily carbonaceous material. Bonds formerly allocated to functional groups become monosubstituted and aromatic C=C bonds as indicated by peaks located at 988 and 1534 cm^{-1} for ZCNi Biocarbon. SDC5 biochar demonstrated a varied spectrum when compared to ZCNi material. SDC5 biochar appeared to contain C-O stretching pertaining to aliphatic ethers at 1026 and 1089 cm^{-1} , similar to

the ZCNi biochar spectrum. The presence of esters is asserted from a peak within the shoulder of the 1089 cm^{-1} peak (1201 cm^{-1}). A small peak at 1424 cm^{-1} denotes the presence of O-H bending conforming to carboxylic acids. A medium peak at 1585 cm^{-1} corresponds to cyclic alkenes, comparable to ZCNi biochar. SDC5 biocarbon displays a strong peak at 1026 cm^{-1} relating to the presence of C-O stretching from aliphatic ethers, however C-O stretching from esters appeared to remain within the material post carbonization. Much like the ZCNi biocarbon spectrum, biocarbon SDC5 contained cyclic alkenes denoted from the peak located at 1551 cm^{-1} . When comparing the two materials, it is clear that the conjunction of the ZnCl_2 and NiNO_3 catalysts plays a vital role in cleaving functional groups during HTL processing. This is evident with the absence of esters and carboxylic groups in the resulting ZCNi biochar. Conversely, SDC5, which lacks any catalyst, retained several oxygen containing groups (denoted earlier) that could negatively affect electrochemical performance.

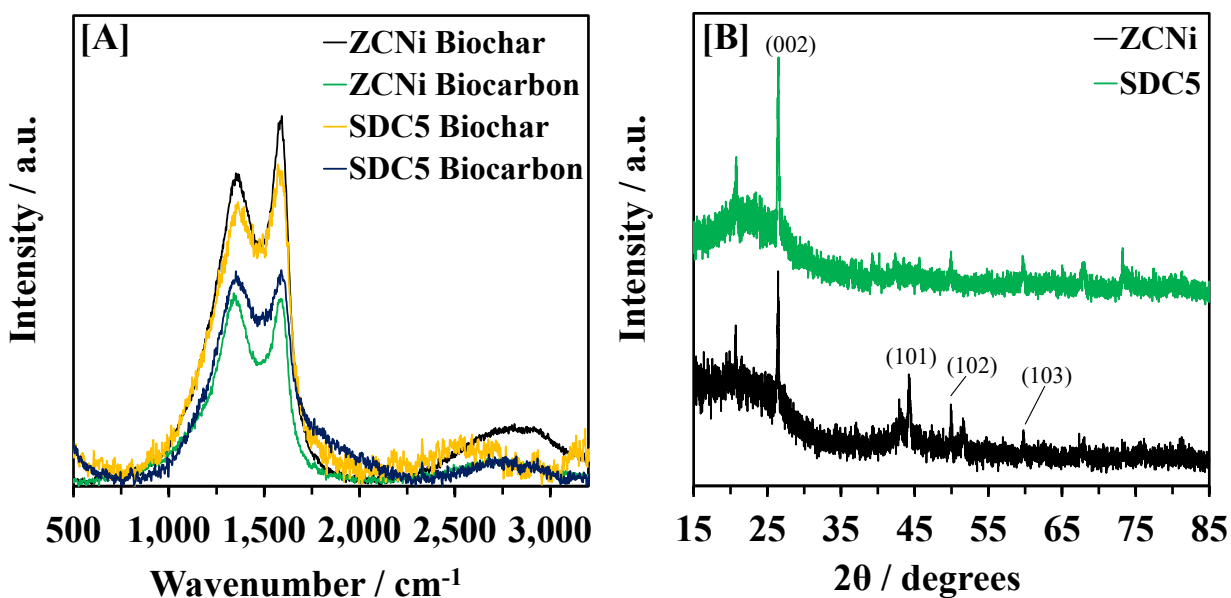


Figure 6.5. [A] Raman spectroscopy of ZCNi and SDC5 biochars and biocarbons. [B] XRD of ZCNi and SDC5 biocarbons.

Raman spectroscopy can help determine the graphitic nature of biocarbons and was employed for both presented biochars and biocarbons (Figure 6.5A). Raman spectra indicated two characteristic peaks, known as the D and G band (1351 and 1587 cm^{-1}), and a minor, but broad, G' band (2800 cm^{-1}). The D band implies defects within the graphitic layers of the biochars/biocarbons while the G band signifies more ordered sp^2 hybridized correlating to $-\text{C}=\text{C}-$ bonding.^[93] The minor G' band denotes interlayer interactions of graphite and is composed of multiple bands, hence the broad nature of the peak.^[181] A physio-characteristic parameter to assess the degree of graphitization can be derived from taking the ratio of intensities from the D and G band, respectively and is known as $I_d:I_g$. A lower $I_d:I_g$ asserts a higher degree of graphitization leading to higher conductivity. ZCNi biochar demonstrated an $I_d:I_g$ of 0.85 while the biocarbon $I_d:I_g$ was 1.02. This increase in the $I_d:I_g$ post carbonization is common and is explained by a theory proposed by Murty et al. where graphitization is a growth process. Heat supplied from the furnace breaks bonds causes rearrangement and crosslinking to fill in voids, known as a point-defect mechanism.^[88] The ZCNi biochar suggests a lower $I_d:I_g$ ratio compared to the non-catalytic SDC5 sample (0.88). It is clear from ATR-FTIR analysis that the ZCNi biochar demonstrated a lower presence of functional groups due to catalytic bond cleaving during HTL. This, in effect, would lead to a more crystalized biochar. During carbonization, the supplied energy would go towards the rearrangement of bonds over further functional group cleaving, hence the increase in as $I_d:I_g$. This difference is pronounced in SDC5 biocarbon where the $I_d:I_g$ was 0.99 and the biocarbon retained some $\text{C}=\text{O}$ bonding from esters. Further analysis of Raman results yielded nanographite planar size utilizing Equation 6.1. ZCNi and SDC5 held calculated L_a values of 22.7 and 21.8 nm, respectively. The higher planar size for ZCNi biochar can be attributed to the enhanced cleaving of functional groups discussed earlier. Post graphitization, the planar sizes were reduced to 18.9 and 19.3 nm for ZCNi and SDC5,

respectively, and correlates to the degree of graphitization. The lower planar size for ZCNi is justified by the theory of graphitization where bond rearrangement could induce smaller planar sizes.

Crystallography measurements were conducted on both biocarbons (Figure 6.5B) to determine micro characteristics of ZCNi and SDC, biocarbons. The most common peak observed in bio-based graphitic carbons is the (002) at $2\theta = 26^\circ$ signifying a reflection of the graphite basal plane. Additional graphitic peaks for ZCNi biocarbon were (101), (102), and (103) at $2\theta = 44, 49,$ and 59° , respectively. Crystallite size and interplanar distance were determined by Scherrer's Equation and Bragg's Law. ZCNi and SDC5 biocarbons obtained a calculated crystallite size of 0.72 and 0.64 nm both with an interplanar distance of 0.336 nm, respectively. In general, bio-based carbons tend to contain turbostratic graphitic layers, however here, interplanar distances correspond to graphite with minimal defects. These results indicate ZCNi biocarbon contained graphite with 2-3 layers while SDC5 biocarbon contained graphite with 1-2 layers. While the crystallite size remained small for both biocarbons, it is important to note that the layers of graphite within the material are generally free of defects due to the interplanar distances close to pure graphite (0.335 nm).^[182] This helps with improving conductivity by reducing ohmic resistances and the transfer of ions during electrochemical testing.^[113] While these results proved similar, both biocarbons held vastly different specific capacitances, meaning other factors, such as BET, have an overbearing effect on electrochemical performance.

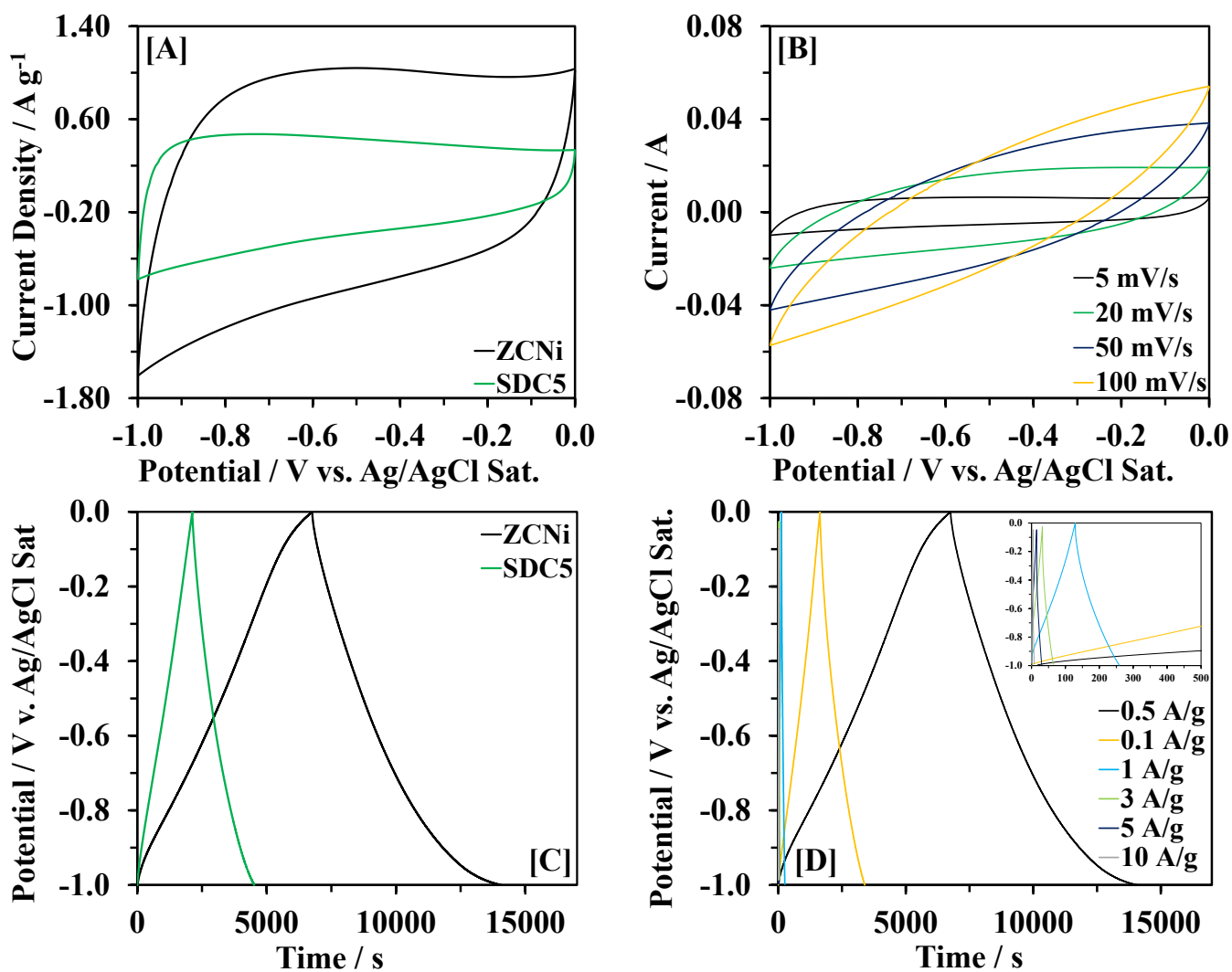


Figure 6.6. CV graphs of ZCNi and SDC5 at 5 mV s^{-1} [A] and ZCNi at scan rates ranging $5 - 100 \text{ mV s}^{-1}$ [B]. Chronopotentiometry of ZCNi and SDC5 at 0.05 A g^{-1} [C] and ZCNi at current densities ranging $0.05 - 10 \text{ A g}^{-1}$ [D].

Electrochemical experiments were performed on ZCNi biochar, ZCNi biocarbon and SDC5 biocarbon, however graphics containing ZCNi biochar electrochemical data are given in the Supplemental Instruction. All experiments were conducted in 2 M KOH between $-1 - 0 \text{ V vs. Ag/AgCl (sat.)}$. Cyclic voltammograms shown in Figure 6.6A exhibit smooth curves absent of redox reactions (reversible or irreversible), indicative of ideal EDLC behavior. ^[118] For

voltammograms, a larger area inside the curve corresponds to higher specific capacitance. Here, ZCNi biocarbon not only exceeds the area of SDC5 biocarbon, but also contains a more box-like shape, demonstrating enhanced ion mobility within the carbonaceous framework. Maintaining this box-like shape further indicates ideal capacitive behavior. Figure 6.6B validates ZCNi biocarbon's capability for enhanced ion transport at higher scan rates ($> 5 \text{ mV s}^{-1}$). ZCNi biocarbon reached a specific capacitance of 316 F g^{-1} at 5 mV s^{-1} and maintained a specific capacitance of 199 F g^{-1} at 20 mV s^{-1} . Higher scan rates provided reduced specific capacitances where scan rates 50 and 100 mV s^{-1} gave specific capacitances of 122 and 68 F g^{-1} , respectively. This is due to limited ion diffusivity caused by the rapid transport of electrolyte ions and is characteristic for hierarchical porous carbons.^[113] SDC5 biocarbon achieved a specific capacitance of less than half that of ZCNi biocarbon (139 F g^{-1} , 5 mV s^{-1}), however specific capacitances of these two materials were nearly the same at 100 mV s^{-1} (64 F g^{-1} , SDC5 biocarbon). This further supports the reduction of penetrable area and limited ion diffusivity observed at higher scan rates.

Chronopotentiometry (CP) in 3-cell was performed on ZCNi and SDC5 biocarbons to analyze ion adsorption-desorption characteristics similar to fabricated supercapacitors. CD curves in Figure 6.6C demonstrated symmetrical sawtooth-like shape at 0.05 A g^{-1} distinctive of EDLC ideal charge separation. ZCNi biocarbon held a significantly longer charge time signifying a higher specific capacitance (278 F g^{-1}) over SDC5 biocarbon (96 F g^{-1}). While true charge separation only occurs at low current densities, Figure 6.6D establishes ZCNi biocarbon's capability to retain an ideal shape at higher current densities ($0.05 - 10 \text{ A g}^{-1}$), signifying enhanced adsorption-desorption characteristics.^[113] Increasing current density inevitably leads to reduced specific capacitance due decreased penetrable area discussed earlier, however ZCNi was able to maintain a specific

capacitance of 100 F g^{-1} at 3 A g^{-1} . Physical and electrochemical data is summarized in Table 6.1 for comparison.

Table 6.1. Tabulated summary of presented results.

Material	Specific Capacitance CV, 5 mV s^{-1} F g^{-1}	S_{BET} $\text{m}^2 \text{ g}^{-1}$	V_{BET} $\text{cm}^3 \text{ g}^{-1}$	S_{avg} nm	Id:Ig	La nm	Crystallite Size nm
ZCNi Biochar	-	1060	0.40	1.51	0.85	22.7	-
ZCNi Biocarbon	316	753	0.27	1.43	1.02	18.9	0.72
SDC5 Biochar	-	20.7	0.04	8.00	0.88	21.8	-
SDC5 Biocarbon	139	140	0.22	6.29	0.99	19.3	0.64

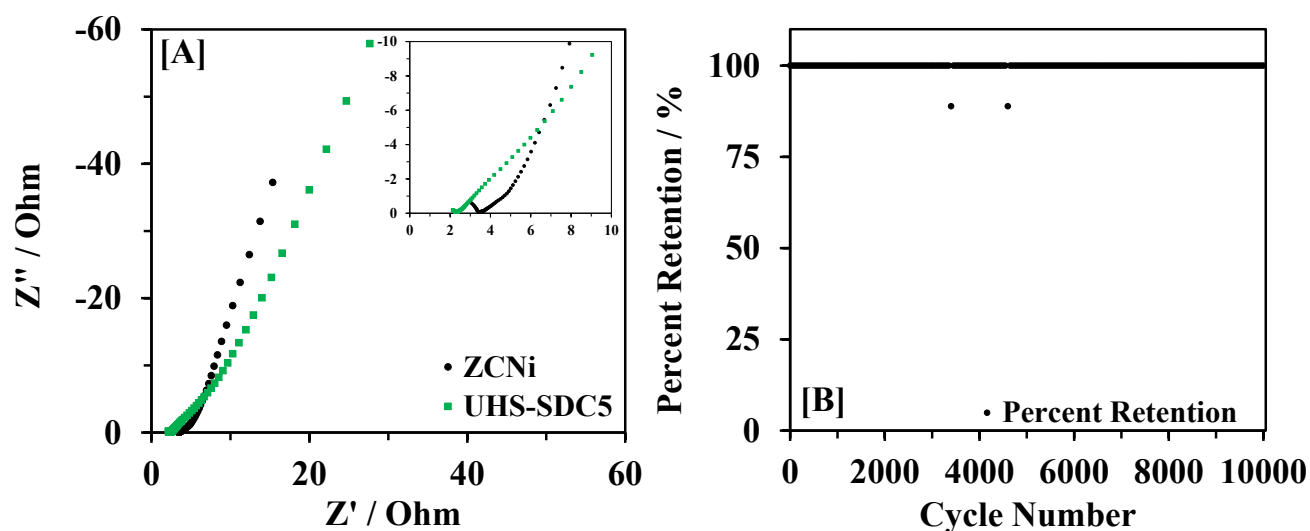


Figure 6.7. [A] EIS spectra of ZCNi and SDC5 biocarbon with high frequency region (inset) and [B] Stability data of ZCNi biocarbon over 10,000 cycles.

EIS experiments were conducted in an open circuit format to discern differences in material resistances, electrode-electrolyte interactions, and overall capacitive behavior. Nyquist plots in Figure 6.7A and inset reveal three characteristic regions correlating to interfacial charge resistance (high frequency), Warburg resistance (medium frequency), and ideal capacitive behavior (low

frequency). Equivalent series resistance (ESR) can be determined from where $-Z''$ crosses the x-axis in Figure 6.7A (inset). ESR denotes the resistance between electrode material and substrate as well as the ohmic resistance of the electrode-electrolyte interface.^[183] The ESR for ZCNi was 3.01 Ω , however SDC5 demonstrated a lower resistance of 2.13 Ω . This lower resistance can be attributed to the reduced surface area and larger pore sizing allowing ions to move freely within the material framework, albeit at reduced storage. The Warburg resistance corresponds to ion diffusion from the electrolyte to the electrode surface.^[121] Determining the slope of this region denotes the behavior of ion diffusion where a value of 1 is designated as ideal. ZCNi and SDC5 obtained a slope of 1.12 and 1.20 for the medium frequency region, respectively. The low frequency region signifies overall ideal capacitive behavior where higher slopes are desired.^[122] Here, ZCNi and SDC5 obtained values of 3.66 and 2.62, respectively. ZCNi demonstrated superior ion diffusion and overall ideal capacitive behavior, comparative to the non-catalytic sample SDC5, signifying enhanced material properties obtained from the catalytic HTL of corn stover.

Stability analysis was performed on ZCNi biocarbon fabricated into a symmetrical electrode coin cell (CR2032) and presented in Figure 6.7B. The coin cell underwent CP for 10000 cycles at 0.5 A g⁻¹ with 1000 cycles prior for proper break in. Results indicated a robust and stable material where specific capacitance remained at 100 % retention. In comparison with literature, Table 6.2 presents reported values of corn-derived biocarbons exhibiting the novelty and competitiveness of this work.

Table 6.2. Comparison of corn-derived biocarbons*

Material	Activation Technique	Specific Capacitance F g ⁻¹	S _{BET} m ² g ⁻¹	V _{BET} cm ³ g ⁻¹	Retention %	Reported Cycles	Reference
Corn Stover	ZnCl ₂ /NiNO ₃	316	753	0.27	100	10000	This Work
Corn Stover	Microwave pyrolysis	246	1433	0.76	n/a	n/a	[66]
Corn Stover	Facile thermal carbonization	242	215	0.12	92	2500	[113]
Corn Cob	KOH	328	3054	1.50	91	10000	[149]
Corn Stem	KOH	232	1420	n/a	n/a	10000	[98]
Corn Silk	KOH	160	2285	1.44	87.6	n/a	[68]
Corn Husk	KOH, thermal carbonization	356	867	0.51	95	2500	[69]
Corn Stalk	KOH, Ni catalyst	323	2495	1.23	98	1000	[100]
Corn Stalk	Fe catalyst, pyrolysis	213	540	0.48	99 (columb.)	6000	[67]
Corn Straw	Hydrothermal carbonization	222	1771	1.85	94	5000	[99]
Corn Starch	H ₃ PO ₄	162	1167	1.80	93	5000	[65]

* An expanded table of various biomass feedstocks is denoted in Appendix A8 (Table A8.1)

6.4. Conclusions

Presented is a novel and effective method for converting an abundant agricultural waste into a value-added product with emphasis on material properties that correspond to enhanced electrochemical performance. Fractionated low ash corn stover was hydrothermally liquefied in the presence of Ni(NO₃)₂ and ZnCl₂ at 275 °C then thermally treated at 450 °C to cleave remaining functional groups and prepare the biocarbon for graphitization. The subsequent hydrochar was

carbonized at 815 °C for 3 h under inert atmosphere to enhance graphitization and improve conductivity. Electrochemical results demonstrated a specific capacitance of 316 F g⁻¹ in aqueous electrolyte and retained 100 % of its capacitance over 10,000 cycles. BET results achieved an S_{BET} and V_{BET} of 753 m² g⁻¹ and 0.27 cm³ g⁻¹, respectively, agreeing with electrochemical results. The addition of catalytic activators during HTL aided in functional group cleaving leading to enhanced pore formation and improved graphitization.

Chapter VII. Process Scale-up Modeling and Technoeconomic Analysis of Biocarbon Production

Katelyn M. Shell, Bharathkiran Maddipudi, Vinod S. Amar, Arjun Patel, Robert F. Rafferty, Rajesh V. Shende, and Ram B. Gupta

Abstract

Biocarbon for energy storage devices has undergone extensive research within the last decade, however large scale graphitic biocarbon production facilities remain largely nonexistent. In this study a preliminary investigation into the economic feasibility of a large scale biocarbon production facility is carried out utilizing received biochar from the hydrothermal liquefaction (HTL) of corn stover biomass. Aspen Plus simulations are performed prior to the techno-economic analysis (TEA) to gain a comprehensive insight of scaled up production and material and energy balances. Data from detailed bench scale processes are used as the basis for pilot scale-up and subsequent modeling. Simulation results indicated a 73% yield of biocarbon from biochar feedstock demonstrating yields comparable to bench scale. TEA calculations include total capital and operating costs, which suggested good economic viability with a payoff period of seven years. Overall results provide a solid foundation for future studies and indicate the commercialization potential of corn stover-derived biocarbon for energy storage devices.

7.1 Introduction

Biomass is an abundant low-cost feedstock for biochars and biocarbons that have a wealth of uses in the areas of carbon capture, soil remediation, batteries and supercapacitors.^[184] Corn stover (stalks, stems, leaves, tassels, etc.) is a particularly ample biomass resource in the United States produced at 1.5 dry tons per acre yield.^[104] Rich in carbon containing lignocellulosic compounds, such as lignin, cellulose, and hemicellulose, corn stover provides an excellent template for energy storage materials, like supercapacitors.^[103] Currently, energy storage devices utilize carbons from petroleum cokes, creating large amounts of CO₂ and other greenhouse gasses (GHG) and depleting non-renewable sources.^{[113],[185]} This generates an urgent need for sustainable energy storage materials, like biocarbon, which can be synthesized from corn stover.

Often, a pretreatment process is necessary to breakdown the cellulosic structures within the cell wall.^[112] Hydrothermal liquefaction is an emerging moderate-temperature, elevated-pressure method for conversion of biomass to biofuels and chemicals.^[54] Byproduct solid residues are produced during the conversion, forming amorphous lignin-rich carbonaceous material suitable as a precursor for energy storage materials. These solid residues can be transformed into graphitic biocarbons through thermal activation methods which increase conductivity, facilitating electron mobility.^{[20],[21]} First, the solid residue undergoes thermal annealing (300 – 500 °C), removing functional groups such as O-H and C=O to form biochar, followed by a high temperature thermal activation (> 700 °C) to form graphitic structures. The method is well suited for scale up due to valorization of chemical waste streams in compact process steps.

Biocarbon production largely remains at bench scale, except for the coconut husk/shell-based biochar. The U.S. Bioenergy Technologies Office (BETO) has a targeted biomass feedstock cost of \$88 per metric ton while the current cost for corn stover is only \$65 per metric ton (dry basis), making it economically attractive.^{[186],[187]} Graphitic carbons for energy storage can have market value of upwards of \$20,000 ton⁻¹ with a global market of \$45 billion by year 2025.^[188] This is projected to further increase due to the heightened demand for smart devices, electric vehicles, and renewable microgrid systems. Hence, there is a need for more biocarbon production facilities that convert an easily accessible biomass feedstock into value added materials.

Several technoeconomic studies have been conducted on the conversion of biomass to biochars and biocarbons primarily for the purposes of steel making, CO₂ capture, and soil amendments, however there appears to be limited analysis on the production of graphitic biocarbon for energy storage.^{[189]-[191]} Aspen Plus simulations along with TEAs can provide insight into the real world plant modeling, production yields, and utility costs. This work presents synthesis of corn stover-

derived biocarbon, from the solid residues of an HTL method, adapted from bench scale to a pilot scale. The pilot scale is examined via Aspen Plus simulations to determine the feasibility of synthesis at scale, followed by a preliminary techno-economic analysis (TEA). Unit operation descriptions and justifications, yield comparisons of bench scale synthesis and Aspen simulations, total capital and operation costs, as well as time to payoff will be discussed.

7.2 Methods

7.2.1 Bench Scale Process

The basis for the pilot plant was developed at bench scale. Here, unhydrolyzed solids (UHS) were converted into hydrochar and subsequently to biochar under non-catalytic conditions through hydrothermal liquefaction (HTL) at South Dakota School of Mines and Technology (SDSMT). Biochar was generated from the low temperature annealing of hydrochar at 400 °C in a tubular furnace for 1 h. Detailed information on biochar synthesis is described in Shell et al. (2021).^[113] The biochar is received by Virginia Commonwealth University (VCU) and undergoes a multistep acid washing process using 1 M HCl, sonication, centrifugation, then decanting subsequent liquids. A small amount of 0.5 M NaOH (~1 mL) was used to neutralize the biochar followed by water washing. The wet biochar is dried overnight at -10 psig at 40 °C. Dried biochar undergoes high temperature carbonization at 850 °C for 3 h to form graphitic biocarbon. Additional process parameters, steps, waste effluent volumes, pH, and characterizations are noted in Figure 7.1.

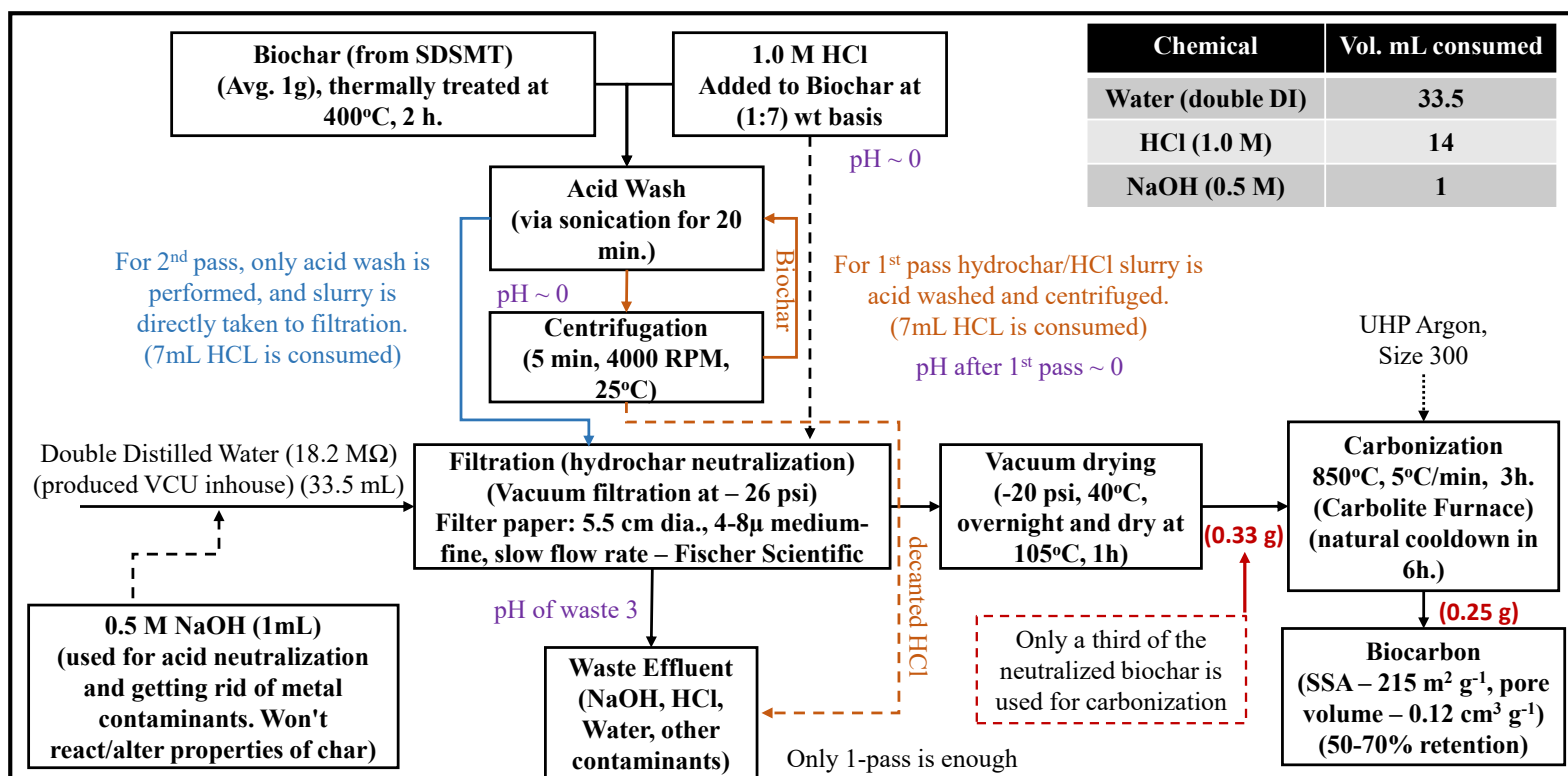


Figure 7.1. Block flow diagram of bench scale biocarbon production with process parameters and characterization details

7.2.2 Aspen Plus Model

Aspen Plus v10.1 is a powerful tool for conducting large scale simulations and was utilized for modeling the presented pilot scale process. A ‘solids’ template was selected for this progression. Biochar was modeled as a nonconventional component where ultimate analysis from literature values of corn stover derived biochar were given (Table 7.1). The process was modeled as a continuous plant with feed rate of 250 kg day^{-1} . Individual steps were modeled as separate unit operations. Physical and chemical reaction processes were modeled in separate flowsheets, and then results were combined to denote one continuous process. The chemical reactions flowsheet utilized FORTRAN statements in a calculator block to help perform atomic balances. ELECNRTL

was used as the base property method due to the usage of ionizable compounds such as HCl and NaOH.

The physical processes such as washing, filtration, and drying were modeled as blocks SWASH, FILTER (solids separator), and DRYER with appropriate parameters. The carbonization was modeled in a two-reactor flow. The first being an RYEILD reactor where product yields are specified by the user. The reaction temperature and pressure mimicked bench scale experiments and valid phases were denoted as “Solids-only”. An RGIBBS reactor followed the RYIELD reactor and gives flow rates of the products based on thermodynamic equilibrium. Modeled flowsheets are shown in Figure 7.3 with subsequent stream results.

Table 7.1. Ultimate analysis of corn stover-derived biochar.^[192]

Element	Composition wt.%
Ash	14.2
Carbon	74.3
Hydrogen	2.7
Nitrogen	0.8
Chlorine	0
Sulfur	0
Oxygen	8

7.2.3 Technoeconomic Analysis

Manual calculations were performed following a pseudo Lang method of factors to determine equipment, installed, and total capital costs. Equipment costs were determined from obtained quotes. Utility costs were determined using energy rates pertinent to Richmond, VA. The plant is

designed to run continuously, thus reflected in the calculations. Operating costs reflect the culmination of labor (3 operators, 8 hr shifts), maintenance, raw materials, and utility costs. Yearly return designates the revenue generated from selling the produced biocarbon. Coconut shell/husk biocarbon was used as a market benchmark biocarbon to which the yearly revenue is calculated from. Time to payoff is denoted as how many years until the pilot plant operates without deficit and is calculated as,

$$Payoff = TCC_{yr} - Net_{op} \quad (7.1)$$

$$Net_{op} = Net_p - C_{op} \quad (7.2)$$

where TCC_{yr} is the remaining capital costs for a particular year in USD, Net_p is the amount of revenue generated from the sales of the product for the same year in USD, C_{op} is the yearly operating costs in USD.

7.3 Results and Discussion

The bench scale method delivered about 0.25 g of biocarbon per day while the pilot scale is slated to deliver 150 kg of biocarbon per day. This, nearly five order of magnitude increase, requires innovative approaches in order to deliver an economically accurate scaling. At bench scale, aqueous waste stream volumes reach nearly 50 mL per gram of biochar. For 250 kg of biochar (starting), this would total 12,500 L (~3,300 gal) per day, therefore, the inclusion of recycling of aqueous streams becomes necessary to reduce the water requirement. Scaling equipment becomes a factor in feasibility as well. Large scale equipment, such as centrifuges, vacuum dryers, and vacuum filtration set-ups can add tens of thousands of dollars to the capital cost which can delay the payoff period considerably. To render this biocarbon synthesis path feasible, it is imperative

for equipment to serve multiple uses in order to reduce cost while still delivering a quality product. This is also help increase the equipment usage time.

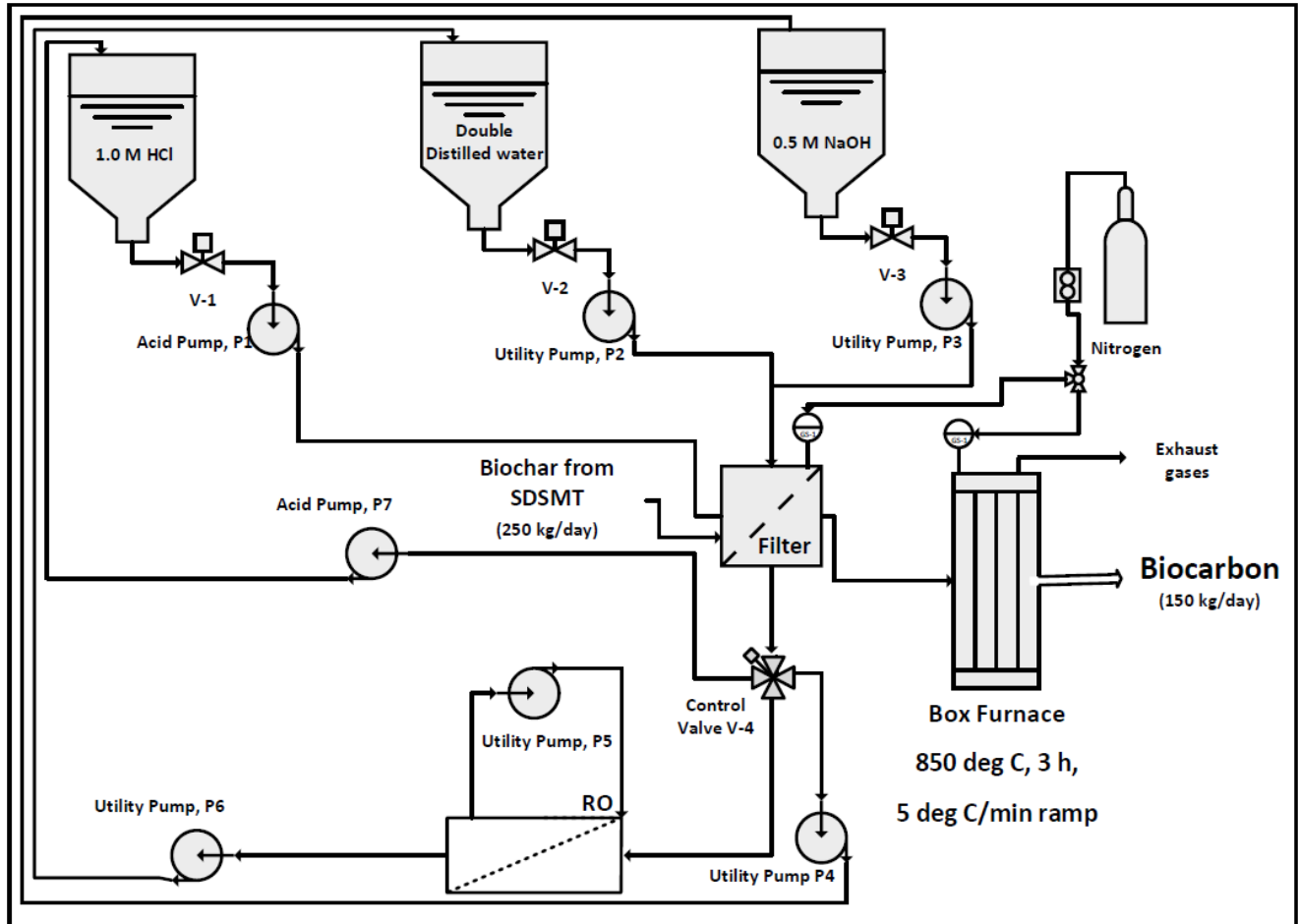


Figure 7.2. Process flow diagram of proposed pilot scale biocarbon production plant.

Figure 7.2 illustrates the proposed pilot scale process flow diagram (PFD). Biocarbon, at a rate of 250 kg per day, is fed into a multi-use filtration system, which has a capacity of 85 kg per load. The filtration system serves as a central and integral part of the pilot plant. Here, acid wash, neutralization, and decanting are all performed with the use of nitrogen to pressurize the system and remove moisture. During the acid wash, 1.0 M HCl is pumped into the filter where biochar fills the candles. Excess HCl exits the filter and is recycled back into the tank. 0.5 M NaOH is then

pumped into the filtration system to help neutralize the biochar, and then it is recycled back to its respective tank. Finally, water is pumped into the system to wash the material of any residual salts or ions that may be present from the washing process. Excess water is pumped into a reverse osmosis (RO) system that is capable of removing the residual salts and ions at a rate of 7000 gal per day. The water then returns to its respective tank for re-use. Following the washing process, the biocarbon enters into a box 4.2 cubic feet box furnace for carbonization at 850 °C under N₂ for 3 h.

7.3.1 Aspen Plus Modeling

Aspen Plus modeling was performed utilizing the scaled pilot plant shown in Figure 7.2 and as discussed in the previous section. Aspen Plus is used to model each step of the process as a separate unit operation. For example, the washing of biochar and decanting of excess HCl are denoted as separate unit operations. Below (in order) are the modeled unit operations with process parameters, descriptions and results. The full Aspen Plus simulation is represented in Figure 7.3 with stream descriptions denoted in Table 7.2.

HCLWASH

The first step in the washing process is the introduction of 1.0 M HCl to dry biochar at a 4:1 weight ratio. This removes any unwanted metal contaminants that may be present from previous processing. In order to reach the goal of 150 kg of biocarbon a day, dry biochar is fed into HCLWASH, which is a representative solid washing unit operation, at a rate of 10.42 kg h⁻¹ (25 °C, 1 bar). Here, the mixing efficiency is taken as 1. For Aspen Plus modeling purposes, a small amount of nitrogen (to provide oxygen-free atmosphere) is fed in with the dry biochar. Throughout the process this nitrogen is denoted as an inert component and does not participate in any reactions.

FLTSTG1

The HCl/biochar slurry exits HCLWASH and enters FILTST1. From laboratory experiments it was found that the fraction of liquids retained in the biochar was 60 wt.%, thus this is denoted as 0.6 for liquid load of solid outlet. The fraction of solids retained was denoted at 0.9 to satisfy mass balance requirements. About 70% of the liquids exit FILTSTG1 in the liquid stream and the solids stream contains 37.5% liquids and 62.5% solids.

NAOHNEUT

Following FLTSTG1, the biochar stream enters the NAOHNEUT SWASH unit operation, where 0.5 M NaOH is fed into the system at a rate of 30.6 kg h^{-1} to ensure a liquid to solid ratio of 0.5:1. Similar to HCLWASH, a mixing efficiency of 1 was used. Liquid and solid fractions of the exit solids stream (NAOHBIOC) were 0.33 and 0.67, respectively.

FLTSTG2

The exit solids stream from NAOHNEUT follows the same pattern as during the HCl washing and filtration steps. Stream NAOHBIOC flows into FLTSTG2 at a rate of 14.07 kg h^{-1} . Parameters for liquid load of solid outlet and fraction of solids to solid outlet are 0.5 and 0.9, respectively. Here, there is little NaOH that is decanted (0.01 kg h^{-1}), therefore future simulations do not need to model a filtration stage post NaOH Wash.

WTRNEUT

The final SWASH stage (WTRNEUT) is utilized for further neutralization of the biochar. Similar to the first SWASH (HCLWASH), the liquid to solid ratio is 4:1 and mixing efficiency of 1 to

ensure full saturation of the material. The biochar/water mixture exiting WTRNEUT flows at a rate of 46.84 kg h^{-1} with a liquids and solids mass ratio of 0.8 and 0.2, respectively.

FLTSTG3

A final filtration step is implemented to decant excess water from the biochar and prepare it for the drying process. Similar to HCLWASH, the liquid load of the solid outlet is 0.6 and the fraction of solids to solid outlet is 0.9. The resulting flow rate of the solids stream (BIOCH) exiting FLTSTG3 was 16.62 kg h^{-1} with a liquid and solid fraction of 0.375 and 0.625, respectively.

DRYING

In order to model the carbonization of biochar in Aspen Plus, a two-step simulation was employed. The first step is denoted as unit operation DRYING (shortcut). Wet biomass exiting FLTSTG3 enters into DRYING at $25 \text{ }^\circ\text{C}$ (1 bar) and is heated to $200 \text{ }^\circ\text{C}$. This subsequently evaporates all moisture leaving only biochar, exiting at a rate of 10.39 kg h^{-1} .

BIOCHARY

Modeled in a separate flowsheet, the exact parameters of biochar exiting DRYING are used for the entering stream to BIOCHARY. This reactor uses product yield inputs to determine exit stream composition. The reactor is set to $850 \text{ }^\circ\text{C}$ at 1 bar with yields specified as 0.75 for biocarbon, 0.248 for CO_2 , 0.001 for H_2O , and 0.001 for CO. The model compound for biocarbon is graphitic carbon, a known component in Aspen's database. Component mass flows exiting the reactor are as follows: Biocarbon, 7.79 kg h^{-1} ; CO_2 , 2.58 kg h^{-1} ; H_2O , 0.01 kg h^{-1} ; and CO, 0.01 kg h^{-1} .

EQUILRCT

Immediately following BIOCHARY, an RGIBBS reactor (EQUILRCT) was implemented to determine actual product stream compositions based on phase and chemical equilibrium. Parameters for temperature and pressure were set to match BIOCHARY with one fluid and one solid phase denoted. Given the stream entering EQUILRCT is the same as the one exiting BIOCHARY, the final stream flow rates are 7.31 kg h⁻¹ for biocarbon, 0.83 kg h⁻¹ for CO₂, 0.01 kg h⁻¹ for H₂O, and 2.24 kg h⁻¹ for CO. On average, a 75.7 wt.% yield was achieved during laboratory experiments. The results provided by the Aspen Plus simulations denotes similar yields giving validity to the model.

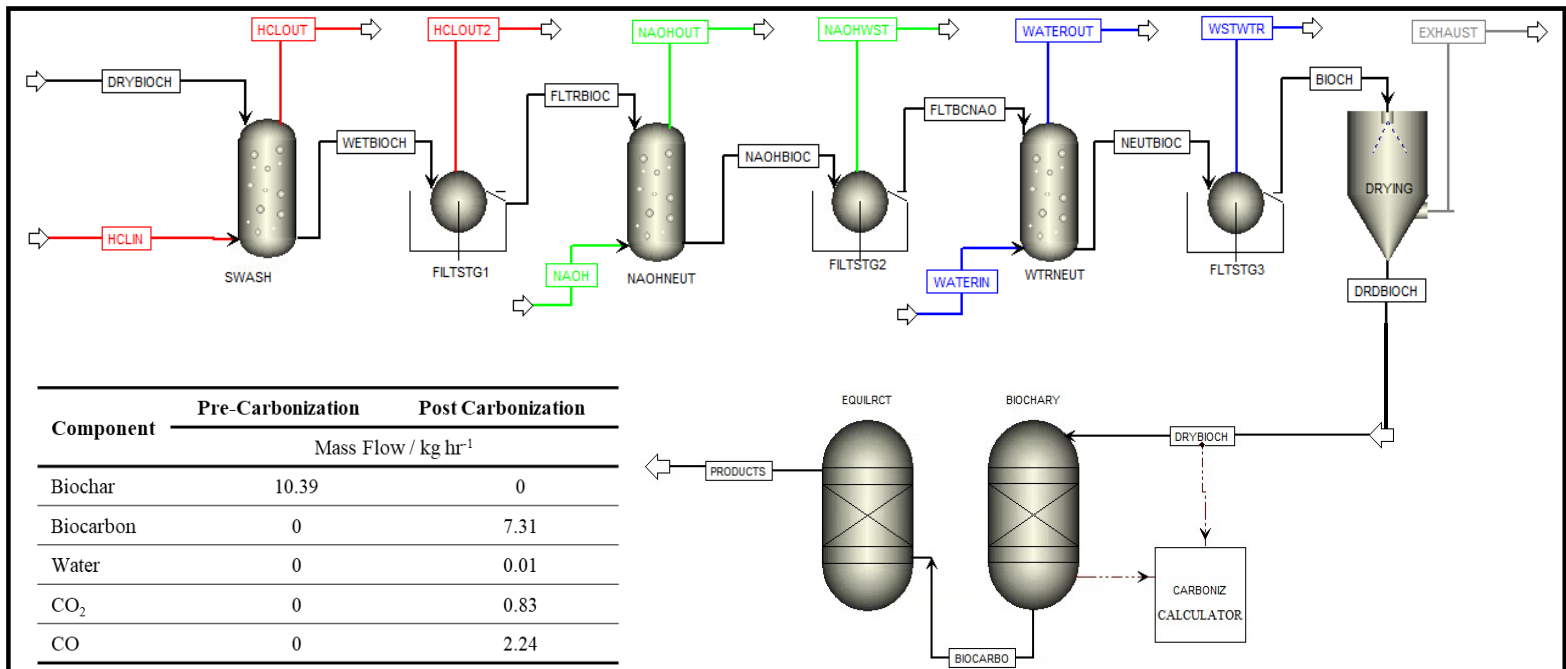


Figure 7.3. Aspen Flow diagram representing the pilot plant process flow diagram as individual unit operations with modeled flow rates pre and post carbonization.

Table 7.2. Descriptions of each stream represented in the Aspen Plus flow diagram

Identifier	Description	Identifier	Description
DRYBIOCH	As-received biochar from SDSMT	FLTBCNAO	Biochar from FLTSTG2 with residual NaOH entering into SWASH (WTRNEUT)
HCLIN	1.0 M HCl entering into the first SWASH unit operation	WATERIN	Water entering WTRNEUT for final washing/neutralization of biochar
HCLOUT	Excess HCl exiting from first SWASH unit operation	WATEROUT	Excess water from WTRNEUT
WETBIOCH	Biochar with adsorbed HCl exiting from SWASH and entering into filter (FLTSTG1)	NEUTBIOC	Neutralized biochar from WTRNEUT entering into filter (FLTSTG3)
HCLOUT2	Decanted HCl from filter (FLTSTG1)	WSTWTR	Water decanted from unit operation FLTSTG3
FLTBIOSH	Filtered biochar from FLTSTG1 entering SWASH unit (NAOHNEUT)	BIOCH	Biochar with residual moisture from FLTSTG3 entering into the drying unit operation (DRYING)
NAOH	0.5 M NaOH entering into SWASH (NAOHNEUT)	EXHAUST	Vapor stream from the drying of biochar
NAOHOUT	Excess NaOH from NAOHNEUT	DRDBIOCH	Dried biochar entering the carbonization unit operation
NAOHBIOC	Biochar exiting NAOHNEUT and entering filter (FLTSTG2)	BIOCARBO	Biocarbon produced from biochar at 850 °C
NAOHWST	Decanted NaOH from FLTSTG2	PRODUCTS	Actual products streams based off thermodynamic equilibrium

7.3.2 Technoeconomic Analysis

A preliminary technoeconomic analysis was conducted on the pilot scale production of corn stover-derived biocarbon through manual calculations following a pseudo-Lang method of factors. Analysis began with determination of equipment costs based off the pilot scale PFD. Three holding tanks of various sizes would be needed for the 1.0 M HCl (200 gal), 0.5 M NaOH (100 gal), and water (500 gal). These tanks ranged in price from \$500 to \$2,400 and would all be manufactured from acid/base-resistant plastics. The filtration unit was specifically designed for this process by

Nano-Mag Technologies Ltd and is comprised of Hastelloy steel for resistance to corrosive materials. Capacity for this unit is 85 kg (wet basis) with biochar discharge capabilities from pressurized nitrogen. Total cost for this unit was quoted at \$80,000 directly from the manufacturer. Due to the infeasibility of a large-scale tube furnace, a box furnace, sized to 4.2 cu ft was chosen for the carbonization of biochar at scale. A Grieve Ovens box furnace with similar volume to scaled calculations was chosen at a cost of \$35,297. Reverse osmosis was implemented to recycle water from the acid washing of received biochar. A 7,000 gal per day unit was quoted from Crystal Quest to be \$7,200. This unit is capable of effectively removing Na⁺, Cl⁻, Ca⁺⁺, and any other contaminant ions that may be present in the waste effluent. Transportation of liquid streams via pumps is necessary to automate the pilot facility. Two acid pumps are needed for pumping 1.0 M HCl to the filtration system and recycling of spent effluent. The cost per unit is nearly \$7,000 as quoted from Magnatex. The four remaining pumps needed were sized to a max of with various flow capabilities. A detailed list of each unit and total equipment cost can be viewed in Table 7.3.

Table 7.3. Equipment list, capacities, materials of construction, cost for individual units and company of manufacture.

Pilot Scale Equipment	Capacity	Material of Construction	Cost per unit	Supplier
HCl Tank	200 gal	Plastic	\$2,321	Tamco
Water Tank	500 gal	Plastic	\$1,263	Ace Roto-Mold / Den-Hartog
NaOH Tank	100 gal	Plastic	\$483	Tamco
Filtration Unit	85 kg	Hastelloy	\$80,000	Nano-Mag
Box Furnace	4.2 cu ft	Multiple	\$35,297	Grieve
Reverse Osmosis (pump incl.)	7,000 gal day ⁻¹	Multiple	\$7,190	Crystal Quest
Acid Pump X 2	50 GPM	Metal	\$6,910	Magnatex Pumps
Utility Pump X 4	40.5 ft head	Metal	\$208	Little Giant
Total			\$140,582	

After obtaining quotes and combining equipment costs, installation costs were determined using the Lang factor for a solids and liquids processing plant (3.63).^[193] This factor was multiplied by the total equipment cost to obtain the total installed costs. The total equipment cost was subtracted to obtain only the installation cost. The installation costs of this biocarbon production plant were calculated to be approx. \$370,000. The last part of calculating total capital costs is having a facility or platform for construction. As per project goals, the construction of the pilot plant will be within a small transport trailer (8 x 16 ft). While costs vary for a trailer of this size depending on wear, a search was able to provide an average cost of \$13,000 for a used, but in good condition, trailer. The summation of equipment, installation, and platform of construction costs equal the total capital costs for this model and are listed in Table 7.4.

Energy consumption and subsequent utility costs were calculated based on power requirements of equipment listed in Table 7.3. In theory, the plant will run continuously throughout the year, therefore a total of 8760 h will be used for calculating energy consumption. The box furnace will require 19 kW of power and will consume 166,440 kWh yr⁻¹. The main power consumption from operating reverse osmosis is from the pump that pressurizes the system. The 1.5 hp (1.1 kW) pump for the reverse osmosis unit would consume 9,800 kWh over the course of one year. There are six additional pumps needed for the pilot scale production of biocarbon; two acid pumps and four utility pumps. For the purposes of this model all power requirements pertaining to the utility pumps will be the same due the availability of information. One acid pump contains a 5.27 hp motor (~4 kW), thus one pump requires 35,000 kWh yr⁻¹. In total, the two acid pumps will require 70,000 kWh yr⁻¹. A 1/3 hp (0.25 kW) magnetic drive utility pump will require much less power, thus all four pumps will require 8,800 kWh per annum. Utility costs were based on rates for Richmond,

VA where the cost of electricity is \$0.1104 per kWh (Dominion Power). Multiplying the total energy consumption by the rate per kWh yields a utility cost of 28,100 yr⁻¹.

Obtaining raw materials regularly will be required for the scaled process. While the overall plant is designed with recycling loops, fresh HCl, NaOH and water will be needed in order to maintain quality biocarbon production. At this time, it is unclear if one particular vendor or multiple vendors will be used for obtaining raw materials, however it is assumed that multiple vendors will be utilized with the purpose of maintaining competitive production costs. Concentrated HCl (37 wt.%) can be purchased from Lab Alley in 55 gal drums (~200 L) for \$1,500 per drum. 1.0 M HCl can be prepared from the concentrated solution. The HCl will be changed weekly leading to a yearly cost of \$24,000. Sodium hydroxide (50 wt.% solution) in 55 gal drums can be purchased from Alliance Chemical for \$930 per drum. The 0.5 M NaOH solution will be changed weekly yielding a yearly cost of \$ 2,790. The main proponent in biocarbon synthesis is water, specifically double distilled (18.2 MΩ) water. Water can be purchased from Ingredi.com for \$124 per 55 gal drum with the DI water for the water only tank slated to be changed quarterly. Including the water needed for NaOH and HCl solutions, water will cost \$62,430 annually.

Maintenance of pilot equipment is imperative to the longevity of production. Maintenance costs generally are about 5 – 10% of the fixed equipment costs.^[194] Here, a factor of 0.075, representing the mean of maintenance costs, is used for calculation leading to an approx. total of \$7,900 annually. While the plant is modeled as a continuous operation, constant supervision of the facility will be needed. Three operators in 8 h shifts are included in the TEA with an annual salary of \$50,000 per operator yielding a labor cost of \$150,000. The summation of utility, raw material, maintenance, and labor costs comprise the yearly operating costs for this pilot plant and is listed in Table 7.4.

Yearly return was calculated using the market price of coconut husk-derived biocarbon (provided by Delta Adsorbents) at \$6,000 ton⁻¹. The pilot plan is expected to produce about 150 kg biocarbon per day totaling 55 tons annually. If all of the biocarbon is sold, this equates to an annual return of \$330,000. The total capital costs and annual operation costs are \$524,000 and \$249,000, respectively. Utilizing Equation (7.1), there is a net profit of \$81,000 per annum which will go directly to offset total capital costs. By applying Equation (7.2), the estimated time to payoff was determined to be seven years and exceeds the target goal of 10 years

Table 7.4. Manual calculations of costs related to pilot scale biocarbon plant with years to payoff.

Description	Amount
Equipment Costs	\$140,600
Installation Costs	\$370,000
Total Capital Costs	\$524,000
Utility Costs (yearly)	\$28,100
Operating Costs (yearly)	\$249,000
Yearly Return (Est.)	\$330,000
Time to Payoff	7 yrs.

7.3.3 Limitations of the Model

The TEA provided in this work gives comprehensive preliminary insight into the feasibility of a pilot scale corn stover-derived facility, however there are certain limitations to this model. It is apparent that no transportation costs have been assessed which may be non-negligible for some locations. This is primarily due to the lack of information available about where the feedstock and raw materials will be coming from. Trucking companies have not been established in this project for the transportation of biochar to the biocarbon facility as well as the biocarbon transported from the facility. Taxes and inflation were also not part of the model as they would be covered by

possible incentives for renewable industry. While the plant is modeled to be located in Richmond, VA, it is very possible the plant will be situated elsewhere. This could effectively change the model and payoff period due to inflated or deflated costs associated with a different area. Feedstock compositions are subject to change based on the catalytic methods used in the collaborators pilot facilities. This could change costs associated with maintenance and/or require more frequent changing of fluids. Nevertheless, the model provides a good look into the feasibility of a pilot scale biocarbon production facility.

7.4 Conclusions

Production of biocarbon from a facile thermal carbonization was first developed at bench scale, then scaled up. The proposed pilot scale process design was modeled using Aspen Plus software following a continuous process scheme. The simulation demonstrated product yields of 73 wt.% which are comparable to bench scale yields (76 wt.%) observed experimentally. Following the Aspen Plus simulations, a preliminary technoeconomic analysis was performed to establish the feasibility of the biocarbon pilot plant. Equipment, utility, raw materials, and maintenance costs were all factors of the TEA. Using coconut husk/shell derived biocarbon as a comparable product, it was determined that the pilot plant could break even in seven years. Implications of this research provide a foundation for biocarbon plant modeling for both process and economic feasibility.

Chapter VIII. Conclusions and Future Directions

8.1 Dissertation Conclusions

High performance biomass derived carbons are highly desirable as an alternative for petroleum derived graphitic materials for batteries and supercapacitors. Biomass offers a sustainable, low-cost tactic to meeting the world's energy storage demands and is urgently needed in the commercial market. Presented are several novel techniques for biocarbon synthesis utilizing an integrated biorefinery approach as well as naturally embedded catalysts through phytoremediation. Details discussed include the viability of solid residues from various stages of an IBR, implementation of catalysts to synergistically enhance liquid and solid co-products, in-depth explanations into electrochemical performance based on physical characterizations, and process scale-up feasibility through simulations and technoeconomic analysis.

For the first time, solid residues from the enzymatic hydrolysis of corn stover were converted into biocarbon via low temperature thermal annealing at 375 °C followed by high temperature carbonization at 850 °C. Biocarbons from the 2-step method demonstrated viability as an electrode material, reaching a specific capacitance of 120 F g⁻¹ (CV, 5 mV s⁻¹). The 2-step method produced biocarbons with a significantly higher surface area (43 % more), signifying the need for low temperature thermal annealing prior to carbonization/activation. In this respect, volatile compounds are effectively cleaved allowing for graphitization to occur at higher temperatures. Knowledge gained from these experiments provide a foundation for future studies where catalysts may be implemented to enhance physical properties.

Ensuing experiments focused on the solid products from the HTL of corn stover-derived UHS. During HTL, biofuels, biofuel precursors, and solids are generated, however literature is sparse in utilizing the solids for energy storage. Primary experiments converted biochars, derived at various

HTL conditions, into biocarbon to determine process conditions that enhance electrochemical performance. Results indicated that biocarbon produced from HTL conditions 275 °C, 40 psig, 1 h, and 1:30 ($\text{g}_{\text{biomass}}:\text{g}_{\text{water}}$) achieved the highest specific capacitance of 242 F g^{-1} with 92% retention over 10,000 cycles. Properties that lead to enhanced electrochemical performance included an increase in crystallite size (0.80 nm), which increases conductivity, and higher pore volumes over all other samples. Statistical analysis performed on this sample set denoted three major deductions:

1. Biomass to water ratio and reaction time are the two most significant parameters that determine electrochemical performance of corn stover-derived biocarbons. A theoretical maximum specific capacitance of 333 F g^{-1} could be achieved at HTL experimental conditions of 250 °C, 0 psig, 2 h, and 1:30 ($\text{g}_{\text{biomass}}:\text{g}_{\text{water}}$).
2. Pore volume and degree of graphitization are the most significant physical parameters that effect electrochemical performance. Increases in both parameters deliver higher overall specific capacitances.
3. Statistical analyses can be used in the areas of energy storage to help make critical decisions on processes conditions that can benefit overall performance of the material. Models will be different for various materials due to changes in compositions.

A short study pertaining to the effect of various catalysts, during the HTL of corn stover-derived UHS, on electrochemical performance was conducted. Here, catalysts $\text{Ni}(\text{NO}_3)_2$, $\text{Ni}(\text{OH})_2$, $\text{Ca}(\text{OH})_2$, and K_2CO_3 were implemented during HTL and subsequent biochars were converted to biocarbons, fabricated into electrodes, and underwent electrochemical characterizations. Biocarbons where Ni was utilized demonstrated enhanced electrochemical performance with a specific capacitance of 203 F g^{-1} for biocarbon H1C, however samples where calcium hydroxide

was used as a catalyst during HTL demonstrated similar electrochemical performance to the Ni^{++} samples at increased scan rates and current densities. In addition, Ca^{++} catalyst samples showed increased charge transfer kinetics, as demonstrated by EIS. Calcium containing catalysts provide a lower cost and more environmentally friendly alternative to nickel catalysts which may increase process scalability.

Phytoremediation is an established method for passive remediation of contaminated soil/water, however this route generates unused biomass. Metals, such as Ni^{2+} , are detrimental to the environment in high concentrations, but are utilized as catalysts for the activation of biocarbon. Utilization of phytoremediative techniques as a method of embedding nickel catalysts for energy storage materials is novel. Presented in Chapter V was a comprehensive study demonstrating the effect of preabsorbed catalysts, in different concentrations, on water hyacinth. Cultivated, harvested, and activated in-house, this method demonstrated a specific capacitance of 541 F g^{-1} (5 mV s^{-1} , WH-5), 98% of the theoretical capacitance. Stability studies demonstrated the robustness of the biocarbon with 100% retention over 10,000 cycles. The high specific capacitance is attributed to the large surface area and pore volume, reaching in excess of $3400 \text{ m}^2 \text{ g}^{-1}$ and $2.0 \text{ cm}^3 \text{ g}^{-1}$ for biocarbon WH-5. These results demonstrate the synergistic nature of phytoremediation techniques as both a remediation solution and for producing material for energy storage devices.

Biocarbon production remains at bench scale, except for biocarbons derived from coconut husk. This generates a need for diversification of market electrode grade biocarbons. In order to scale up biocarbon production, computer simulations and economic feasibility studies were conducted through Aspen Plus software and TEA. Aspen plus simulations indicated that pilot scale production of biocarbon is comparable to bench scale yields and will reach the 150 kg day^{-1} target. Following the Aspen Plus modeling, a TEA was performed through manual calculations to

establish if large scale corn-stover derived biocarbon production is feasible and determine the time to payoff. Payoff period was determined to be 7 years based on information gathered which indicates an economically feasible process.

The culmination of studies presented here denotes the ability for bio-derived solid waste streams to be converted into a high quality biocarbon for energy storage devices. Non-catalytic and catalytic HTL-derived biocarbons showed favorable electrochemical performance. Various activation routes for biocarbon synthesis were performed including thermal and thermochemical/catalytic methods with multiple biomass precursors. Lastly, biocarbon processes were scaled for pilot plant implementation with computer simulations and techno-economic analysis, creating a fully comprehensive portfolio of research pertaining to biomass-derived carbons for supercapacitors.

8.2 Future Directions

Simulation of pilot scale production process has been completed, however real-world implementation must be completed to confirm the predictions. Future construction of a pilot scale facility has been confirmed by Southwest Research Institute (SWRI) and is intended to be operational by Summer 2022. Biocarbon produced from the pilot facility will be fabricated into supercapacitors and tested for electrochemical properties and compared to bench scale studies. Information gained from these experiments will confirm the successful production of biocarbon and open pathways for commercial implementation of biocarbons.

Life Cycle analysis (LCA) is an important aspect of cradle to grave design and should be included in the future work. This includes the summation of CO₂ produced during synthesis and from transportation of feedstocks, equipment, raw materials, products, and wastes. Additionally, other

environmental impacts of the facility during construction, post commissioning, and disposing of equipment after the plant has been decommissioned should be factored into the LCA. Results of the LCA are intended to further direct the feasibility of the pilot plant with respect to environmental impacts.

Lastly, further experiments should be conducted with respect to utilizing phytoremediation techniques to catalytically enhance biocarbon for energy storage. Catalysts, such as Mn^{++} , Cu^{++} , and Co^{++} , have been used as post adsorbed catalysts for biocarbon activation. Noting the enhanced activation of biocarbon through pre-adsorbed routes, it would be pertinent to conduct studies on how these catalysts effect pore formation/structures, graphitization, and overall specific capacitance. It is important to note that water hyacinth may not be appropriate for experiments utilizing other catalysts. Hyperaccumulator species are generally resistant to a select number of metal contaminants. Consultation with the hyperaccumulator database produced by the University of Queensland (Australia) is recommended.

References

- [1] EIA projects nearly 50% increase in world energy usage by 2050, led by growth in Asia <https://www.eia.gov/todayinenergy/detail.php?id=41433> (accessed Jul 30, 2021).
- [2] International Energy Agency. Global Energy Review 2021. *Glob. Energy Rev. 2020* **2021**.
- [3] EIA. U.S. energy facts explained <https://www.eia.gov/energyexplained/us-energy-facts/> (accessed Jul 30, 2021).
- [4] Bioenergy Frequently Asked Questions <https://www.energy.gov/eere/bioenergy/bioenergy-frequently-asked-questions#7>.
- [5] Liu, L.; Solin, N.; Inganäs, O. Biocarbon Meets Carbon-Humic Acid/Graphite Electrodes Formed by Mechanochemistry. *Materials (Basel)*. **2019**, *12* (24). <https://doi.org/10.3390/ma1224032>.
- [6] Fu, F.; Yang, D.; Zhang, W.; Wang, H.; Qiu, X. Green Self-Assembly Synthesis of Porous Lignin-Derived Carbon Quasi-Nanosheets for High-Performance Supercapacitors. *Chem. Eng. J.* **2019**, No. August, 123721. <https://doi.org/10.1016/j.cej.2019.123721>.
- [7] Zhao, J. R.; Hu, J.; Li, J. F.; Chen, P. N-Doped Carbon Nanotubes Derived from Waste Biomass and Its Electrochemical Performance. *Mater. Lett.* **2020**, *261*, 127146. <https://doi.org/10.1016/j.matlet.2019.127146>.
- [8] Zhang, L. L.; Zhao, X. S. Carbon-Based Materials as Supercapacitor Electrodes. *Chem. Soc. Rev.* **2009**, *38* (9), 2520–2531. <https://doi.org/10.1039/b813846j>.
- [9] Borenstein, A.; Hanna, O.; Attias, R.; Luski, S.; Brousse, T.; Aurbach, D. Carbon-Based Composite Materials for Supercapacitor Electrodes: A Review. *J. Mater. Chem. A* **2017**, *5*

- (25), 12653–12672. <https://doi.org/10.1039/c7ta00863e>.
- [10] González, A.; Goikolea, E.; Barrena, J. A.; Mysyk, R. Review on Supercapacitors: Technologies and Materials. *Renew. Sustain. Energy Rev.* **2016**, *58*, 1189–1206. <https://doi.org/10.1016/j.rser.2015.12.249>.
- [11] Jäckel, N.; Simon, P.; Gogotsi, Y.; Presser, V. Increase in Capacitance by Subnanometer Pores in Carbon. *ACS Energy Lett.* **2016**, *1* (6), 1262–1265. <https://doi.org/10.1021/acsenergylett.6b00516>.
- [12] Ali, B. A.; Allam, N. K. A First-Principles Roadmap and Limits to Design Efficient Supercapacitor Electrode Materials. *Phys. Chem. Chem. Phys.* **2019**, *21* (32), 17494–17511. <https://doi.org/10.1039/c9cp02614b>.
- [13] Liu, C.; Yan, X.; Hu, F.; Gao, G.; Wu, G.; Yang, X. Toward Superior Capacitive Energy Storage: Recent Advances in Pore Engineering for Dense Electrodes. *Adv. Mater.* **2018**, *30* (17), 1–14. <https://doi.org/10.1002/adma.201705713>.
- [14] Li, Y.; Zhang, D.; Zhang, Y.; He, J.; Wang, Y.; Wang, K.; Xu, Y.; Li, H.; Wang, Y. Biomass-Derived Microporous Carbon with Large Micropore Size for High-Performance Supercapacitors. *J. Power Sources* **2020**, *448* (July 2019), 227396. <https://doi.org/10.1016/j.jpowsour.2019.227396>.
- [15] Jung, S. H.; Myung, Y.; Kim, B. N.; Kim, I. G.; You, I. K.; Kim, T. Y. Activated Biomass-Derived Graphene-Based Carbons for Supercapacitors with High Energy and Power Density. *Sci. Rep.* **2018**, *8* (1), 1–8. <https://doi.org/10.1038/s41598-018-20096-8>.
- [16] Gao, Y. P.; Zhai, Z. B.; Huang, K. J.; Zhang, Y. Y. Energy Storage Applications of

- Biomass-Derived Carbon Materials: Batteries and Supercapacitors. *New J. Chem.* **2017**, *41* (20), 11456–11470. <https://doi.org/10.1039/c7nj02580g>.
- [17] Lu, Y. Facile Method for Preparation of Porous Carbon Derived from Biomass for High Performance Supercapacitors. *Int. J. Electrochem. Sci.* **2019**, *14*, 11199–11211. <https://doi.org/10.20964/2019.12.54>.
- [18] Cai, N.; Cheng, H.; Jin, H.; Liu, H.; Zhang, P.; Wang, M. Porous Carbon Derived from Cashew Nut Husk Biomass Waste for High-Performance Supercapacitors. *J. Electroanal. Chem.* **2020**, *861*, 113933. <https://doi.org/10.1016/j.jelechem.2020.113933>.
- [19] Sima, X. F.; Jiang, S. F.; Shen, X. C.; Jiang, H. Harvesting Biomass-Based Ni-N Doped Carbonaceous Materials with High Capacitance by Fast Pyrolysis of Ni Enriched Spent Wetland Biomass. *Ind. Eng. Chem. Res.* **2019**, *58* (31), 13868–13878. <https://doi.org/10.1021/acs.iecr.9b02126>.
- [20] Sankar, S.; Ahmed, A. T. A.; Inamdar, A. I.; Im, H.; Im, Y. Bin; Lee, Y.; Kim, D. Y.; Lee, S. Biomass-Derived Ultrathin Mesoporous Graphitic Carbon Nanoflakes as Stable Electrode Material for High-Performance Supercapacitors. *Mater. Des.* **2019**, *169*, 107688. <https://doi.org/10.1016/j.matdes.2019.107688>.
- [21] Guo, D.; Song, X.; Li, B.; Tan, L.; Ma, H.; Pang, H.; Wang, X.; Zhang, L.; Chu, D. Oxygen Enriched Carbon with Hierarchical Porous Structure Derived from Biomass Waste for High-Performance Symmetric Supercapacitor with Decent Specific Capacity. *J. Electroanal. Chem.* **2019**, *855* (4), 113349. <https://doi.org/10.1016/j.jelechem.2019.113349>.
- [22] Gabhi, R. S.; Kirk, D. W.; Jia, C. Q. Preliminary Investigation of Electrical Conductivity

- of Monolithic Biochar. *Carbon N. Y.* **2017**, *116*, 435–442.
<https://doi.org/10.1016/j.carbon.2017.01.069>.
- [23] Li, C.; Kumar, S. Preparation of Activated Carbon from Un-Hydrolyzed Biomass Residue. *Biomass Convers. Biorefinery* **2016**, *6* (4), 407–419. <https://doi.org/10.1007/s13399-016-0197-7>.
- [24] Luo, X.; Chen, S.; Hu, T.; Chen, Y.; Li, F. Renewable Biomass-derived Carbons for Electrochemical Capacitor Applications. *SusMat* **2021**, No. December 2020, 211–240. <https://doi.org/10.1002/sus2.8>.
- [25] Abhijit Dutta, Michael Talmadge, Jesse Hensley, Matt Worley, Doug Dudgeon, D. B.; Peter Groenendijk, Daniela Ferrari, Brien Stears, Erin Searcy, C. W.; Hess, and J. R. Techno-Economics for Conversion of Lignocellulosic Biomass to Ethanol by Indirect Gasification and Mixed Alcohol Synthesis. *Am. Inst. Chem. Eng.* **2012**, *31* (2), 182–190. <https://doi.org/10.1002/ep10625>.
- [26] Ahmad, B.; Yadav, V.; Yadav, A.; Rahman, M. U.; Yuan, W. Z.; Li, Z.; Wang, X. Integrated Biorefinery Approach to Valorize Winery Waste: A Review from Waste to Energy Perspectives. *Sci. Total Environ.* **2020**, *719*, 137315. <https://doi.org/10.1016/j.scitotenv.2020.137315>.
- [27] Zang, G.; Shah, A.; Wan, C. Techno-Economic Analysis of an Integrated Biorefinery Strategy Based on One-Pot Biomass Fractionation and Furfural Production. *J. Clean. Prod.* **2020**, *260*, 120837. <https://doi.org/10.1016/j.jclepro.2020.120837>.
- [28] Shende, R. Pilot-Scale Biochemical and Hydrothermal Integrated Biorefinery (IBR) for Cost-Effective Production of Fuels and Value Added Products. 2019.

- [29] Fernand, F.; Israel, A.; Skjermo, J.; Wichard, T.; Timmermans, K. R.; Golberg, A. Offshore Macroalgae Biomass for Bioenergy Production: Environmental Aspects, Technological Achievements and Challenges. *Renew. Sustain. Energy Rev.* **2017**, *75* (November 2016), 35–45. <https://doi.org/10.1016/j.rser.2016.10.046>.
- [30] Mukherjee, G.; Dhiman, G.; Akhtar, N. Efficient Hydrolysis of Lignocellulosic Biomass: Potential Challenges and Future Perspectives for Biorefineries. *Environ. Sci. Eng.* **2017**, 213–237.
- [31] Coppola, F.; Bastianoni, S.; Østergård, H. Sustainability of Bioethanol Production from Wheat with Recycled Residues as Evaluated by Emergy Assessment. *Biomass and Bioenergy* **2009**, *33* (11), 1626–1642. <https://doi.org/10.1016/j.biombioe.2009.08.003>.
- [32] Cantrell, K. B.; Novak, J. M.; Frederick, J. R.; Karlen, D. L.; Watts, D. W. Influence of Corn Residue Harvest Management on Grain, Stover, and Energy Yields. *Bioenergy Res.* **2014**, *7* (2), 590–597. <https://doi.org/10.1007/s12155-014-9433-9>.
- [33] Langholtz, M. H.; Stokes, B. J.; Eaton, L. M. 2016 Billion-Ton Report: Advancing Domestic Resources for a Thriving Bioeconomy, Volume 1: Economic Availability of Feedstock. U.S. Department of Energy. ORNL/TM-2016/160. Oak Ridge National Laboratory. *U.S. Dep. Energy. ORNL/TM-2016/160. Oak Ridge Natl. Lab. Oak Ridge, TN.* **2016**, *1* (Vol. 1), 411.
- [34] Malherbe, S.; Cloete, T. E. Lignocellulose Biodegradation: Fundamentals and Applications. *Rev. Environ. Sci. Biotechnol.* **2002**, *1* (2), 105–114. <https://doi.org/10.1023/A:1020858910646>.
- [35] Kumar, S.; Kothari, U.; Kong, L.; Lee, Y. Y.; Gupta, R. B. Hydrothermal Pretreatment of

- Switchgrass and Corn Stover for Production of Ethanol and Carbon Microspheres. *Biomass and Bioenergy* **2011**, *35* (2), 956–968.
<https://doi.org/10.1016/j.biombioe.2010.11.023>.
- [36] Yu, H.; Xu, Y.; Hou, J.; Ni, Y.; Liu, S.; Liu, Y.; Yu, S.; Nie, S.; Wu, Q.; Wu, C. Efficient Fractionation of Corn Stover for Biorefinery Using a Sustainable Pathway. *ACS Sustain. Chem. Eng.* **2020**, *8* (8), 3454–3464. <https://doi.org/10.1021/acssuschemeng.9b07791>.
- [37] Rackemann, D. W.; Doherty, W. O. S. The Conversion of Lignocellulosics to Levulinic Acid. *Biofuels, Bioprod. Biorefining* **2011**, *5* (2), 198–214.
- [38] Licursi, D.; Antonetti, C.; Fulignati, S.; Vitolo, S.; Puccini, M.; Ribechini, E.; Bernazzani, L.; Raspolli Galletti, A. M. In-Depth Characterization of Valuable Char Obtained from Hydrothermal Conversion of Hazelnut Shells to Levulinic Acid. *Bioresour. Technol.* **2017**, *244* (June), 880–888. <https://doi.org/10.1016/j.biortech.2017.08.012>.
- [39] Rivas, S.; Raspolli-Galletti, A. M.; Antonetti, C.; Santos, V.; Parajó, J. C. Sustainable Conversion of Pinus Pinaster Wood into Biofuel Precursors: A Biorefinery Approach. *Fuel* **2016**, *164*, 51–58. <https://doi.org/10.1016/j.fuel.2015.09.085>.
- [40] Chang, C.; Cen, P.; Ma, X. Levulinic Acid Production from Wheat Straw. *Bioresour. Technol.* **2007**, *98* (7), 1448–1453. <https://doi.org/10.1016/j.biortech.2006.03.031>.
- [41] Efremov, A. A.; Pervyshina, G. G.; Kuznetsov, B. N. Thermocatalytic Transformations of Wood and Cellulose in the Presence of HCl, HBr, and H₂SO₄. *Chem. Nat. Compd.* **1997**, *33* (1), 84–88. <https://doi.org/10.1007/BF02273932>.
- [42] Yan, L.; Yang, N.; Pang, H.; Liao, B. Production of Levulinic Acid from Bagasse and

- Paddy Straw by Liquefaction in the Presence of Hydrochloride Acid. *Clean - Soil, Air, Water* **2008**, *36* (2), 158–163. <https://doi.org/10.1002/clen.200700100>.
- [43] Chen, W.; Hu, H.; Cai, Q.; Zhang, S. Synergistic Effects of Furfural and Sulfuric Acid on the Decomposition of Levulinic Acid. *Energy and Fuels* **2020**, *34* (2), 2238–2245. <https://doi.org/10.1021/acs.energyfuels.9b03971>.
- [44] Covinich, L. G.; Clauser, N. M.; Felissia, F. E.; Vallejos, M. E.; Area, M. C. The Challenge of Converting Biomass Polysaccharides into Levulinic Acid through Heterogeneous Catalytic Processes. *Biofuels, Bioprod. Biorefining* **2020**, *14* (2), 417–445. <https://doi.org/10.1002/bbb.2062>.
- [45] Runge, T.; Zhang, C. Two-Stage Acid-Catalyzed Conversion of Carbohydrates into Levulinic Acid. *Ind. Eng. Chem. Res.* **2012**, *51* (8), 3265–3270. <https://doi.org/10.1021/ie2021619>.
- [46] Lopes, E. S.; Leal Silva, J. F.; Rivera, E. C.; Gomes, A. P.; Lopes, M. S.; Maciel Filho, R.; Tovar, L. P. Challenges to Levulinic Acid and Humins Valuation in the Sugarcane Bagasse Biorefinery Concept. *Bioenergy Res.* **2020**, *13* (3), 757–774. <https://doi.org/10.1007/s12155-020-10124-9>.
- [47] Antonetti, C.; Licursi, D.; Fulignati, S.; Valentini, G.; Galletti, A. M. R. New Frontiers in the Catalytic Synthesis of Levulinic Acid: From Sugars to Raw and Waste Biomass as Starting Feedstock. *Catalysts* **2016**, *6* (12), 1–29. <https://doi.org/10.3390/catal6120196>.
- [48] Timokhin, B. V. Levulinic Acid in Organic Synthesis. *Russ. Chem. Rev.* **1999**, *68* (1), 73–84.

- [49] Hayes, D. J.; Fitzpatrick, S.; Hayes, M. H. B.; Ross, J. R. H. The Biofine Process - Production of Levulinic Acid, Furfural, and Formic Acid from Lignocellulosic Feedstocks. *Biorefineries-Industrial Process. Prod. Status Quo Futur. Dir.* **2008**, *1*, 139–164. <https://doi.org/10.1002/9783527619849.ch7>.
- [50] Jeong, H.; Jang, S. K.; Hong, C. Y.; Kim, S. H.; Lee, S. Y.; Lee, S. M.; Choi, J. W.; Choi, I. G. Levulinic Acid Production by Two-Step Acid-Catalyzed Treatment of Quercus Mongolica Using Dilute Sulfuric Acid. *Bioresour. Technol.* **2017**, *225*, 183–190. <https://doi.org/10.1016/j.biortech.2016.11.063>.
- [51] Muranaka, Y.; Suzuki, T.; Sawanishi, H.; Hasegawa, I.; Mae, K. Effective Production of Levulinic Acid from Biomass through Pretreatment Using Phosphoric Acid, Hydrochloric Acid, or Ionic Liquid. *Ind. Eng. Chem. Res.* **2014**, *53* (29), 11611–11621. <https://doi.org/10.1021/ie501811x>.
- [52] Díaz, M. J.; Cara, C.; Ruiz, E.; Romero, I.; Moya, M.; Castro, E. Hydrothermal Pre-Treatment of Rapeseed Straw. *Bioresour. Technol.* **2010**, *101* (7), 2428–2435. <https://doi.org/10.1016/j.biortech.2009.10.085>.
- [53] Hsu, T.-A. Pretreatment of Biomass. In *Handbook on Bioethanol, Production and Utilization*; C.E Wyman (Ed.), 1996.
- [54] Jaswal, R.; Shende, A.; Nan, W.; Amar, V.; Shende, R. Hydrothermal Liquefaction and Photocatalytic Reforming of Pinewood (Pinus Ponderosa)-Derived Acid Hydrolysis Residue for Hydrogen and Bio-Oil Production. *Energy and Fuels* **2019**, *33* (7), 6454–6462. <https://doi.org/10.1021/acs.energyfuels.9b01071>.
- [55] Sun, Y.; Cheng, J. Hydrolysis of Lignocellulosic Materials for Ethanol Production: A

- Review. *Bioresour. Technol.* **2002**, 83 (1), 1–11. [https://doi.org/10.1016/S0960-8524\(01\)00212-7](https://doi.org/10.1016/S0960-8524(01)00212-7).
- [56] Bobleter, O. Hydrothermal Degradation of Polymers Derived from Plants. *Prog. Polym. Sci.* **1994**, 19 (5), 797–841. [https://doi.org/10.1016/0079-6700\(94\)90033-7](https://doi.org/10.1016/0079-6700(94)90033-7).
- [57] Hendriks, A. T. W. M.; Zeeman, G. Pretreatments to Enhance the Digestibility of Lignocellulosic Biomass. *Bioresour. Technol.* **2009**, 100 (1), 10–18. <https://doi.org/10.1016/j.biortech.2008.05.027>.
- [58] Kohlmann, K. .; Sarikaya, A.; Westgate, P. J.; Weil, J.; Velayudhan, A.; Hendrickson, R.; Ladisch, M. R. *Enhanced Enzyme Activities on Hydrated Lignocellulosic Substrates*; 1995.
- [59] Laxman, R.S. & Lachke, A. H. Bioethanol Lignocellulosic Biomass. In *Handbook Plant-Based Biofuels*; 2009; pp 121–139.
- [60] Mosier, N.; Hendrickson, R.; Ho, N.; Sedlak, M.; Ladisch, M. R. Optimization of PH Controlled Liquid Hot Water Pretreatment of Corn Stover. *Bioresour. Technol.* **2005**, 96 (18 SPEC. ISS.), 1986–1993. <https://doi.org/10.1016/j.biortech.2005.01.013>.
- [61] Thakkar, A.; Kumar, S. Hydrothermal Carbonization for Producing Carbon Materials. *Sub- and Supercritical Hydrothermal Technology*, 2019, 17.
- [62] Weil, J.; Brewer, M.; Hendrickson, R.; Sarikaya, A.; Ladisch, M. R. Continuous PH Monitoring during Pretreatment of Yellow Poplar Wood Sawdust Pressure Cooking Water. *Biotechnol. Fuels Chem.* **1998**, 99–111.
- [63] Liu, C.; Wyman, C. E. The Effect of Flow Rate of Very Dilute Sulfuric Acid on Xylan,

- Lignin, and Total Mass Removal from Corn Stover. *Ind. Eng. Chem. Res.* **2004**, *43* (11), 2781–2788. <https://doi.org/10.1021/ie030754x>.
- [64] Rogalinski, T.; Ingram, T.; Brunner, G. Hydrolysis of Lignocellulosic Biomass in Water under Elevated Temperatures and Pressures. *J. Supercrit. Fluids* **2008**, *47* (1), 54–63. <https://doi.org/10.1016/j.supflu.2008.05.003>.
- [65] Pang, L.; Zou, B.; Han, X.; Cao, L.; Wang, W.; Guo, Y. One-Step Synthesis of High-Performance Porous Carbon from Corn Starch for Supercapacitor. *Mater. Lett.* **2016**, *184*, 88–91. <https://doi.org/10.1016/j.matlet.2016.07.147>.
- [66] Jin, H.; Wang, X.; Shen, Y.; Gu, Z. A High-Performance Carbon Derived from Corn Stover via Microwave and Slow Pyrolysis for Supercapacitors. *J. Anal. Appl. Pyrolysis* **2014**, *110* (1), 18–23. <https://doi.org/10.1016/j.jaap.2014.07.010>.
- [67] Wang, L.; Mu, G.; Tian, C.; Sun, L.; Zhou, W.; Yu, P.; Yin, J.; Fu, H. Porous Graphitic Carbon Nanosheets Derived from Cornstalk Biomass for Advanced Supercapacitors. *ChemSusChem* **2013**, *6* (5), 880–889. <https://doi.org/10.1002/cssc.201200990>.
- [68] Mitravinda, T.; Nanaji, K.; Anandan, S.; Jyothirmayi, A.; Chakravadhanula, V. S. K.; Sharma, C. S.; Rao, T. N. Facile Synthesis of Corn Silk Derived Nanoporous Carbon for an Improved Supercapacitor Performance. *J. Electrochem. Soc.* **2018**, *165* (14), A3369–A3379. <https://doi.org/10.1149/2.0621814jes>.
- [69] Song, S.; Ma, F.; Wu, G.; Ma, D.; Geng, W.; Wan, J. Facile Self-Templating Large Scale Preparation of Biomass-Derived 3D Hierarchical Porous Carbon for Advanced Supercapacitors. *J. Mater. Chem. A* **2015**, *3* (35), 18154–18162. <https://doi.org/10.1039/c5ta04721h>.

- [70] Khu, L. Van; Cu, D. Van; Thi, L.; Thuy, T. Investigation of the Capacitive Properties of Activated Carbon Prepared from Corn Cob in Na₂SO₄ and K₂SO₄ Electrolytes. *Can. Chem. Trans.* **2016**, *4* (3), 302–315.
<https://doi.org/10.13179/canchemtrans.2016.04.03.0317>.
- [71] Arshad, F.; Li, L.; Amin, K.; Fan, E.; Manurkar, N.; Ahmad, A.; Yang, J.; Wu, F.; Chen, R. A Comprehensive Review of the Advancement in Recycling the Anode and Electrolyte from Spent Lithium Ion Batteries. *ACS Sustain. Chem. Eng.* **2020**, *8* (36), 13527–13554.
<https://doi.org/10.1021/acssuschemeng.0c04940>.
- [72] Christensen, D. Battery-Grade Graphite Produced from Siviour Concentrates via Low-Cost Purification. *Renascor Resources Ltd.* 2019, pp 1–4.
- [73] Olson, D. W.; Virta, R. L.; Mahdavi, M.; Sangine, E. S.; Fortier, S. M. Natural Graphite Demand and Supply—Implications for Electric Vehicle Battery Requirements. *GSA Spec. Pap.* **2016**, *520*, 67–77. [https://doi.org/10.1130/2016.2520\(08\)](https://doi.org/10.1130/2016.2520(08)).
- [74] Liu, Z.; Tian, D.; Shen, F.; Nnanna, P. C.; Hu, J.; Zeng, Y.; Yang, G.; He, J.; Deng, S. Valorization of Composting Leachate for Preparing Carbon Material to Achieve High Electrochemical Performances for Supercapacitor Electrode. *J. Power Sources* **2020**, *458* (February), 228057. <https://doi.org/10.1016/j.jpowsour.2020.228057>.
- [75] Dujearic-stephane, K.; Panta, P.; Shulga, Y. M.; Kumar, A. Physico-Chemical Characterization of Activated Carbon Synthesized from Datura Metel ' s Peels and Comparative Capacitive Performance Analysis in Acidic Electrolytes and Ionic Liquids. *Bioresour. Technol. Reports* **2020**, *11* (May), 100516.
<https://doi.org/10.1016/j.biteb.2020.100516>.

- [76] Wang, L.; Li, Y.; Yang, K.; Lu, W.; Yu, J.; Gao, J.; Liao, G.; Qu, Y.; Wang, X.; Li, X.; Yin, Z. Hierarchical Porous Carbon Microspheres Derived from Biomass-Corn cob as Ultra-High Performance Supercapacitor Electrode. *Int. J. Electrochem. Sci.* **2017**, *12* (6), 5604–5617. <https://doi.org/10.20964/2017.06.16>.
- [77] Gupta, R.; Lee, Y. Y. Mechanism of Cellulase Reaction on Pure Cellulosic Substrates. *Biotechnol. Bioeng.* **2009**, *102* (6), 1570–1581. <https://doi.org/10.1002/bit.22195>.
- [78] Mosier, N.; Wyman, C.; Dale, B.; Elander, R.; Lee, Y. Y.; Holtzapple, M.; Ladisch, M. Features of Promising Technologies for Pretreatment of Lignocellulosic Biomass. *Bioresour. Technol.* **2005**, *96* (6), 673–686. <https://doi.org/10.1016/j.biortech.2004.06.025>.
- [79] Zhang, Z.; Zhu, Z.; Shen, B.; Liu, L. Insights into Biochar and Hydrochar Production and Applications: A Review. *Energy* **2019**, *171*, 581–598. <https://doi.org/10.1016/j.energy.2019.01.035>.
- [80] Elliott, D. C.; Biller, P.; Ross, A. B.; Schmidt, A. J.; Jones, S. B. Hydrothermal Liquefaction of Biomass: Developments from Batch to Continuous Process. *Bioresour. Technol.* **2015**, *178*, 147–156. <https://doi.org/10.1016/j.biortech.2014.09.132>.
- [81] Molino, A.; Chianese, S.; Musmarra, D. Biomass Gasification Technology: The State of the Art Overview. *J. Energy Chem.* **2016**, *25* (1), 10–25. <https://doi.org/10.1016/j.jechem.2015.11.005>.
- [82] Zhang, Q.; Chang, J.; Wang, T.; Xu, Y. Review of Biomass Pyrolysis Oil Properties and Upgrading Research. *Energy Convers. Manag.* **2007**, *48* (1), 87–92. <https://doi.org/10.1016/j.enconman.2006.05.010>.

- [83] Gollakota, A. R. K.; Kishore, N.; Gu, S. A Review on Hydrothermal Liquefaction of Biomass. *Renew. Sustain. Energy Rev.* **2018**, *81* (April 2017), 1378–1392.
<https://doi.org/10.1016/j.rser.2017.05.178>.
- [84] Ou, L.; Thilakaratne, R.; Brown, R. C.; Wright, M. M. Techno-Economic Analysis of Transportation Fuels from Defatted Microalgae via Hydrothermal Liquefaction and Hydroprocessing. *Biomass and Bioenergy* **2015**, *72*, 45–54.
<https://doi.org/10.1016/j.biombioe.2014.11.018>.
- [85] Reimer, C.; Snowdon, M. R.; Vivekanandhan, S.; You, X.; Misra, M.; Gregori, S.; Mielewski, D. F.; Mohanty, A. K. Synthesis and Characterization of Novel Nitrogen Doped Biocarbons from Distillers Dried Grains with Solubles (DDGS) for Supercapacitor Applications. *Bioresour. Technol. Reports* **2020**, *9*, 100375.
<https://doi.org/10.1016/j.biteb.2019.100375>.
- [86] Maniscalco, M. P.; Corrado, C.; Volpe, R.; Messineo, A. Bioresource Technology Reports Evaluation of the Optimal Activation Parameters for Almond Shell Bio-Char Production for Capacitive Deionization. *Bioresour. Technol. Reports* **2020**, *11* (February), 100435.
<https://doi.org/10.1016/j.biteb.2020.100435>.
- [87] Houck, J. D.; Shende, R. V. Catalytic HTL-Derived Biochar and Sol-Gel Synthesized (Mn , Ti) -Oxides for Asymmetric Supercapacitors. *Int. J. Energy Res.* **2020**, *44* (15), 12546–12558. <https://doi.org/10.1002/er.5938>.
- [88] Murty, H. N.; Heintz, E. A.; Speer, A.; Falh, N. Kinetics of Graphitization Activation. **1969**, *7*, 667–681.
- [89] Moeser, Geoffrey, D. High Surface Area Graphitized Carbon and Processes for Making

Same, 2009.

- [90] Quosai, P.; Anstey, A.; Mohanty, A. K.; Misra, M. Characterization of Biocarbon Generated by High- and Low-Temperature Pyrolysis of Soy Hulls and Coffee Chaff: For Polymer Composite Applications. *R. Soc. Open Sci.* **2018**, *5* (8).
<https://doi.org/10.1098/rsos.171970>.
- [91] Liu, W. J.; Jiang, H.; Yu, H. Q. Development of Biochar-Based Functional Materials: Toward a Sustainable Platform Carbon Material. *Chem. Rev.* **2015**, *115* (22), 12251–12285. <https://doi.org/10.1021/acs.chemrev.5b00195>.
- [92] Major, I.; Pin, J. M.; Behazin, E.; Rodriguez-Uribe, A.; Misra, M.; Mohanty, A. Graphitization of Miscanthus Grass Biocarbon Enhanced by in Situ Generated FeCo Nanoparticles. *Green Chem.* **2018**, *20* (10), 2269–2278.
<https://doi.org/10.1039/c7gc03457a>.
- [93] Usha Rani, M.; Nanaji, K.; Rao, T. N.; Deshpande, A. S. Corn Husk Derived Activated Carbon with Enhanced Electrochemical Performance for High-Voltage Supercapacitors. *J. Power Sources* **2020**, *471* (June), 228387.
<https://doi.org/10.1016/j.jpowsour.2020.228387>.
- [94] Demir, M.; Kahveci, Z.; Aksoy, B.; Palapati, N. K. R.; Subramanian, A.; Cullinan, H. T.; El-kaderi, H. M.; Harris, C. T.; Gupta, R. B. Graphitic Biocarbon from Metal-Catalyzed Hydrothermal Carbonization of Lignin. **2015**. <https://doi.org/10.1021/acs.iecr.5b02614>.
- [95] Keiluweit, M.; Nico, P. S.; Johnson, M.; Kleber, M. Dynamic Molecular Structure of Plant Biomass-Derived Black Carbon (Biochar). *Environ. Sci. Technol.* **2010**, *44* (4), 1247–1253. <https://doi.org/10.1021/es9031419>.

- [96] Yu, M.; Saunders, T.; Su, T.; Gucci, F.; Reece, M. J. Effect of Heat Treatment on the Properties of Wood-Derived Biocarbon Structures. *Materials (Basel)*. **2018**, *11* (9), 1–9. <https://doi.org/10.3390/ma11091588>.
- [97] Gong, Y.; Li, D.; Fu, Q.; Zhang, Y.; Pan, C. Nitrogen Self-Doped Porous Carbon for High-Performance Supercapacitors. *Appl. Energy Mater.* **2020**, *3*, 1585–1592. <https://doi.org/10.1021/acsaem.9b02077>.
- [98] Lee, M. E.; Choe, J. H.; Yun, Y. S.; Jin, H.-J. Corn Stem-Derived, Hierarchically Nanoporous Carbon as Electrode Material for Supercapacitors. *Nanosci. Nanotechnol.* **2017**, *17* (6), 7729–7734. <https://doi.org/https://doi-org.proxy.library.vcu.edu/10.1166/jnn.2017.14773>.
- [99] Lu, Y.; Zhang, S.; Yin, J.; Bai, C.; Zhang, J.; Li, Y.; Yang, Y.; Ge, Z.; Zhang, M.; Wei, L.; Ma, M.; Ma, Y.; Chen, Y. Data on High Performance Supercapacitors Based on Mesoporous Activated Carbon Materials with Ultrahigh Mesopore Volume and Effective Specific Surface Area. *Data Br.* **2018**, *18*, 1448–1456. <https://doi.org/10.1016/j.dib.2018.04.057>.
- [100] Cao, Y.; Wang, K.; Wang, X.; Gu, Z.; Fan, Q.; Gibbons, W.; Hoefelmeyer, J. D.; Kharel, P. R.; Shrestha, M. Hierarchical Porous Activated Carbon for Supercapacitor Derived from Corn Stalk Core by Potassium Hydroxide Activation. *Electrochim. Acta* **2016**, *212*, 839–847. <https://doi.org/10.1016/j.electacta.2016.07.069>.
- [101] Xue, Y.; Chen, H.; Zhao, W.; Chao, Y.; Ma, P.; Han, S. A Review on the Operating Conditions of Producing Biooil from Hydrothermal Liquefaction of Biomass. *Int. J. Energy Res.* **2016**, *40*, 865–877. <https://doi.org/10.1002/er.3473>.

- [102] Tungal, R.; Shende, R. V. Hydrothermal Liquefaction of Pinewood (*Pinus Ponderosa*) for H₂, Biocrude and Bio-Oil Generation. *Appl. Energy* **2014**, *134*, 401–412.
<https://doi.org/10.1016/j.apenergy.2014.07.060>.
- [103] Bao, D.-X.; Yu, Y.-Y.; Zhao, Q.-M. Evaluation of the Chemical Composition and Rheological Properties of Bio-Asphalt from Different Biomass Sources. *Road Mater. Pavement Des.* **2020**, *21* (7), 1829–1843.
<https://doi.org/10.1080/14680629.2019.1568287>.
- [104] García, R.; Pizarro, C.; Lavín, A. G.; Bueno, J. L. Biomass Sources for Thermal Conversion. Techno-Economical Overview. *Fuel* **2017**, *195*, 182–189.
<https://doi.org/10.1016/j.fuel.2017.01.063>.
- [105] Fatma, S.; Hameed, A.; Noman, M.; Ahmed, T.; Sohail, I.; Shahid, M.; Tariq, M.; Tabassum, R. Lignocellulosic Biomass: A Sustainable Bioenergy Source for Future. *Protein Pept. Lett.* **2018**, *25* (January).
<https://doi.org/10.2174/0929866525666180122144504>.
- [106] Baruah, J.; Bikash, K. N.; Sharma, R.; Kumar, S.; Deka, R. C.; Baruah, D. C.; Kalita, E. Recent Trends in the Pretreatment of Lignocellulosic Biomass for Value-Added Products. *Front. Energy Res.* **2018**, *6*, 141. <https://doi.org/10.3389/fenrg.2018.00141>.
- [107] Beims, R. F.; Hu, Y.; Shui, H.; Charles, C. Hydrothermal Liquefaction of Biomass to Fuels and Value-Added Chemicals: Products Applications and Challenges to Develop Large-Scale Operations. *Biomass and Bioenergy* **2020**, *135*, 105510.
<https://doi.org/10.1016/j.biombioe.2020.105510>.
- [108] Castello, D.; Pedersen, T. H. Continuous Hydrothermal Liquefaction of Biomass: A

- Critical Review. *Energies* **2018**, *11* (11), 3165. <https://doi.org/10.3390/en11113165>.
- [109] Houck, J. D.; Amar, V. S.; Shende, R. V. Sol-Gel Derived Mixed Phase (Mn, Ti)-Oxides/Graphene Nanoplatelets for Hybrid Supercapacitors. *Int. J. Energy Res.* **2020**, *44* (15), 12474–12484. <https://doi.org/10.1002/er.5454>.
- [110] Shell, K. M.; Vohra, S. Y.; Rodene, D. D.; Gupta, R. B. Phytoremediation of Nickel via Water Hyacinth for Biocarbon-Derived Supercapacitor Applications. *Energy Technol.* **2021**, *9* (8), 2100130. <https://doi.org/10.1002/ente.202100130>.
- [111] Amar, V. S.; Houck, J. D.; Maddipudi, B.; Penrod, T. A.; Shell, K. M.; Thakkar, A.; Shende, A. R.; Hernandez, S.; Kumar, S.; Gupta, R. B.; Shende, R. V. Hydrothermal Liquefaction (HTL) Processing of Unhydrolyzed Solids (UHS) for Hydrochar and Its Use for Asymmetric Supercapacitors with Mixed (Mn, Ti) Perovskite Oxides. *Renew. Energy* **2021**, *173*, 329–341. <https://doi.org/10.1016/j.renene.2021.03.126>.
- [112] Anuj Thakkar, Katelyn M. Shell, Martino Bertosin, Dylan D. Rodene, Vinod Amar, Alberto Bertucco, Ram B. Gupta, Rajesh Shende, and S. K. Production of Levulinic Acid and Biocarbon Electrode Material from Corn Stover through an Integrated Biorefinery Process. *Fuels Process. Technol.*
- [113] Shell, K. M.; Rodene, D. D.; Amar, V.; Thakkar, A.; Maddipudi, B.; Kumar, S.; Shende, R.; Gupta, R. B. Supercapacitor Performance of Corn Stover-Derived Biocarbon Produced from the Solid Co-Products of a Hydrothermal Liquefaction Process. *Bioresour. Technol. Reports* **2021**, *13* (February 2020), 100625. <https://doi.org/10.1016/j.biteb.2021.100625>.
- [114] Anderson, E. M.; Katahira, R.; Reed, M.; Resch, M. G.; Karp, E. M.; Beckham, G. T.; Román-Leshkov, Y. Reductive Catalytic Fractionation of Corn Stover Lignin. *ACS*

- Sustain. Chem. Eng.* **2016**, *4* (12), 6940–6950.
<https://doi.org/10.1021/acssuschemeng.6b01858>.
- [115] de Caprariis, B.; Scarsella, M.; Bavasso, I.; Bracciale, M. P.; Tai, L.; De Filippis, P. Effect of Ni, Zn and Fe on Hydrothermal Liquefaction of Cellulose: Impact on Bio-Crude Yield and Composition. *J. Anal. Appl. Pyrolysis* **2021**, *157* (June), 105225.
<https://doi.org/10.1016/j.jaap.2021.105225>.
- [116] Ong, H. C.; Chen, W. H.; Farooq, A.; Gan, Y. Y.; Lee, K. T.; Ashokkumar, V. Catalytic Thermochemical Conversion of Biomass for Biofuel Production: A Comprehensive Review. *Renew. Sustain. Energy Rev.* **2019**, *113* (July), 109266.
<https://doi.org/10.1016/j.rser.2019.109266>.
- [117] Lu, Q.; Li, W.; Zhang, X.; Liu, Z.; Cao, Q.; Xie, X.; Yuan, S. Experimental Study on Catalytic Pyrolysis of Biomass over a Ni/Ca-Promoted Fe Catalyst. *Fuel* **2020**, *263* (September 2019), 116690. <https://doi.org/10.1016/j.fuel.2019.116690>.
- [118] Gong, Y.; Li, D.; Fu, Q.; Zhang, Y.; Pan, C. Nitrogen Self-Doped Porous Carbon for High-Performance Supercapacitors. *ACS Appl. Energy Mater.* **2020**, *3* (2), 1585–1592.
<https://doi.org/10.1021/acsaem.9b02077>.
- [119] Abanades, J. C.; Criado, Y. A.; Fernández, J. R. An Air CO₂capture System Based on the Passive Carbonation of Large Ca(OH)₂structures. *Sustain. Energy Fuels* **2020**, *4* (7), 3409–3417. <https://doi.org/10.1039/d0se00094a>.
- [120] Zhao, Y.; Xie, H.; Ma, Q.; Zhang, B.; Chen, X.; Xing, P.; Yin, H. Recovery of Cobalt and Nickel from Hard Alloy Scraps for the Synthesis of Li(Ni_{1-x-y}CoxMny)O₂ Lithium-Ion Battery Cathodes. *J. Sustain. Metall.* **2020**, *6* (4), 775–784.

<https://doi.org/10.1007/s40831-020-00314-2>.

- [121] He, Y.; Zhang, Y.; Li, X.; Lv, Z.; Wang, X.; Liu, Z. Capacitive Mechanism of Oxygen Functional Groups on Carbon Surface in Supercapacitors. *Electrochim. Acta* **2018**, *282*, 618–625. <https://doi.org/10.1016/j.electacta.2018.06.103>.
- [122] Arulepp, M.; Leis, J.; Latt, M.; Miller, F.; Rumma, K.; Lust, E.; Burke, A. F. The Advanced Carbide-Derived Carbon Based Supercapacitor. *J. Power Sources* **2006**, *162*, 1460–1466. <https://doi.org/10.1016/j.jpowsour.2006.08.014>.
- [123] Twardowska, I., Allen, H. E., Kettrup, A. F., & Lacy, W. J. *Solid Waste: Assessment, Monitoring and Remediation*; Gulf Professional Publishing, 2004.
- [124] Pandey, V.; Baudhh, K. *Phytomanagement of Polluted Sites*; Elsevier Inc.: Cambridge, MA, 2019.
- [125] Meuser, H. *Soil Remediation and Rehabilitation: Treatment of Contaminated and Disturbed Land*; Springer Science and Business Dordrecht, 2013.
<https://doi.org/10.1007/978-94-007-5751-6>.
- [126] Nascimento, C.; Xing, B. Phytoextraction: A Review on Enhanced Metal Availability and Plant Accumulation. *Sci. Agric.* **2006**, *63* (3), 299–311.
- [127] Mallick, N.; Bagchi, S. K.; Koley, S.; Singh, A. K. Progress and Challenges in Microalgal Biodiesel Production. *Front. Microbiol.* **2016**, *7* (JUN), 1–11.
<https://doi.org/10.3389/fmicb.2016.01019>.
- [128] Details, A.; Kumar, N.; Baudhh, K.; Dwivedi, N.; Barman, S. C.; Singh, D. P.; Division, E. M. Accumulation of Metals in Selected Macrophytes Grown in Mixture of Drain Water

- and Tannery Effluent and Their Phytoremediation Potential. *J. Environ. Biol.* **2012**, *33* (5), 923–927.
- [129] Shah, M.; Hashmi, H. N.; Ali, A.; Ghumman, A. R. Performance Assessment of Aquatic Macrophytes for Treatment of Municipal Wastewater. *J. Environ. Heal. Sci. Eng.* **2014**, *12*, 1–12.
- [130] Henry-silva, G. G.; Camargo, A. F. M. Efficiency of Aquatic Macrophytes to Treat Nile Tilapia Pond Effluents. *Sci. Agric.* **2006**, *63* (5), 433–438.
- [131] Kinidi, L.; Salleh, S. Phytoremediation of Nitrogen as Green Chemistry for Wastewater Treatment System. *Int. J. Chem. Eng.* **2017**, *2017*, 1–12.
- [132] Ibezim-Ezeani, M.; Ihunwo, O. Assessment of Pb, Cd, Cr and Ni in Water and Water Hyacinth (*Eichhornia Crassipes*). *J. Appl. Sci. Environ. Manag.* **2020**, *24* (4), 719–727.
- [133] Baudouin, C.; Charveron, M.; Tarroux, R.; Gall, Y.; Institut, C.; Pierre, D. R.; Cellulaire, L. D. B. Environmental Pollutants and Skin Cancer. *Cell Biol. Toxicol.* **2002**, *18*, 341–348.
- [134] Li, X.; Zhou, Y.; Yang, Y.; Yang, S.; Sun, X. Physiological and Proteomics Analyses Reveal the Mechanism of *Eichhornia Crassipes* Tolerance to High-Concentration Cadmium Stress Compared with *Pistia Stratiotes*. *PLoS One* **2015**, *10* (4), 1–22.
<https://doi.org/10.1371/journal.pone.0124304>.
- [135] Niu, J.; Shao, R.; Liu, M.; Zan, Y.; Dou, M.; Liu, J. Porous Carbons Derived from Collagen-Enriched Biomass: Tailored Design, Synthesis, and Application in Electrochemical Energy Storage and Conversion. *Adv. Funct. Mater.* **2019**, *29* (46), 1–23.

<https://doi.org/10.1002/adfm.201905095>.

- [136] Liu, W.; Jiang, H.; Yu, H. Thermochemical Conversion of Lignin to Functional Materials: A Review and Future Directions. *Green Chem.* **2015**, *17*, 4888–4907.

<https://doi.org/10.1039/c5gc01054c>.

- [137] Hussain, S. T.; Mahmood, T.; Malik, S. A. Phytoremediation Technologies for Ni⁺⁺ by Water Hyacinth. *African J. Biotechnol.* **2010**, *9* (50), 8648–8660.

<https://doi.org/10.4314/ajb.v9i50>.

- [138] Simenonov, L. I.; Hassanien, M. A. *Exposure and Risk Assessment of Chemical Pollution - Contemporary Methodology*; Springer Science and Business Media, 2009.

- [139] Thommes, M.; Kaneko, K.; Neimark, A. V.; Olivier, J. P.; Rodriguez-Reinoso, F.; Rouquerol, J.; Sing, K. S. W. Physisorption of Gases, with Special Reference to the Evaluation of Surface Area and Pore Size Distribution (IUPAC Technical Report). *Pure Appl. Chem.* **2015**, *87* (9–10), 1051–1069. <https://doi.org/10.1515/pac-2014-1117>.

- [140] Zhang, Y.; Liu, S.; Zheng, X.; Wang, X.; Xu, Y.; Tang, H.; Kang, F. Biomass Organs Control the Porosity of Their Pyrolyzed Carbon. *Adv. Funct. Mater.* **2017**, *27* (3), 1–8.

<https://doi.org/10.1002/adfm.201604687>.

- [141] Zheng, K.; Li, Y.; Zhu, M.; Yu, X.; Zhang, M.; Shi, L. The Porous Carbon Derived from Water Hyacinth with Well-Designed Hierarchical Structure for Supercapacitors. *J. Power Sources* **2017**, *366*, 270–277. <https://doi.org/10.1016/j.jpowsour.2017.09.034>.

- [142] Ganguli, S.; Roy, A. K.; Anderson, D. P. Improved Thermal Conductivity for Chemically

- Functionalized Exfoliated Graphite/Epoxy Composites. *Carbon N. Y.* **2008**, *46* (5), 806–817. <https://doi.org/10.1016/j.carbon.2008.02.008>.
- [143] Dijith, K. S.; Aiswarya, R.; Praveen, M.; Pillai, S.; Peethambharan, K. Polyol Derived Ni and NiFe Alloys for Effective Shielding of Electromagnetic Interference. *Mater. Chem. Front.* **2018**, *2*, 1829–1841. <https://doi.org/10.1039/c8qm00264a>.
- [144] Zhang, Y.; Sun, C.; Tang, Z. High Specific Capacitance and High Energy Density Supercapacitor Electrodes Enabled by Porous Carbon with Multilevel Pores and Self-Doped Heteroatoms Derived from Chinese Date. *Diam. Relat. Mater.* **2019**, *97*, 107455. <https://doi.org/10.1016/j.diamond.2019.107455>.
- [145] Zhang, G.; Chen, Y.; Chen, Y.; Guo, H. Activated Biomass Carbon Made from Bamboo as Electrode Material for Supercapacitors. *Mater. Res. Bull.* **2018**, *102*, 391–398. <https://doi.org/10.1016/j.materresbull.2018.03.006>.
- [146] Demir, M.; Ashourirad, B.; Mugumya, J. H.; Saraswat, S. K.; El-kaderi, H. M.; Gupta, R. B. Nitrogen and Oxygen Dual-Doped Porous Carbons Prepared from Pea Protein as Electrode Materials for High Performance Supercapacitors. *Int. J. Hydrogen Energy* **2018**, *43* (40), 18549–18558. <https://doi.org/10.1016/j.ijhydene.2018.03.220>.
- [147] Li, J.; Liu, K.; Gao, X.; Yao, B.; Huo, K.; Cheng, Y.; Cheng, X. Oxygen- and Nitrogen-Enriched 3D Porous Carbon for Supercapacitors of High Volumetric Capacity. *ACS Appl. Mater. Interfaces* **2015**, *7* (44), 24622–24628. <https://doi.org/10.1021/acsami.5b06698>.
- [148] Sun, L.; Tian, C.; Li, M.; Meng, X.; Wang, L.; Wang, R.; Yin, J.; Fu, H. From Coconut Shell to Porous Graphene-like Nanosheets for High-Power Supercapacitors. *J. Mater. Chem. A* **2013**, *1*, 6462–6470. <https://doi.org/10.1039/c3ta10897j>.

- [149] Wang, D.; Geng, Z.; Li, B.; Zhang, C. High Performance Electrode Materials for Electric Double-Layer Capacitors Based on Biomass-Derived Activated Carbons. *Electrochim. Acta* **2015**, *173*, 377–384. <https://doi.org/10.1016/j.electacta.2015.05.080>.
- [150] Zhu, B.; Liu, B.; Qu, C.; Zhang, H.; Guo, W.; Liang, Z.; Chen, F.; Zou, R. Tailoring Biomass-Derived Carbon for High-Performance Supercapacitors from Controllably Cultivated Algae Microspheres. *J. Mater. Chem. A* **2018**, No. 4, 1–8. <https://doi.org/10.1039/C7TA09608A>.
- [151] Graham, R. L.; Sheehan, J. Current and Potential U.S. Corn Stover Supplies. *Agron. J.* **2007**, *99* (January), 1–11. <https://doi.org/10.2134/argonj2005.0222>.
- [152] Polin, J. P.; Carr, H. D.; Whitmer, L. E.; Smith, R. G.; Brown, R. C. Conventional and Autothermal Pyrolysis of Corn Stover: Overcoming the Processing Challenges of High-Ash Agricultural Residues. *J. Anal. Appl. Pyrolysis* **2019**, *143*, 104679. <https://doi.org/10.1016/j.jaap.2019.104679>.
- [153] Shende, A.; Tungal, R.; Jaswal, R.; Shende, R. A Novel Integrated Hydrothermal Liquefaction and Solar Catalytic Reforming Method for Enhanced Hydrogen Generation from Biomass. *J. Energy Res.* **2015**, *3* (1), 1–7. <https://doi.org/10.12691/ajer-3-1-1>.
- [154] Tungal, R.; Shende, R. Subcritical Aqueous Phase Reforming of Wastepaper for Biocrude and H₂ Generation. *Appl. Energy* **2013**, *134*, 401–412.
- [155] Wang, L. J. Production of Bioenergy and Bioproducts from Food Processing Wastes: A Review. *Trans. ASABE* **2013**, *56* (1), 217–230. <https://doi.org/10.13031/2013.42572>.
- [156] Michailof, C. M.; Kalogiannis, K. G.; Sfetsas, T.; Patiaka, D. T.; Lappas, A. A. Advanced

- Analytical Techniques for Bio-Oil Characterization. *Wiley Interdiscip. Rev. Energy Environ.* **2016**, 5 (6), 614–639. <https://doi.org/10.1002/wene.208>.
- [157] González, J. F.; Román, S.; Encinar, J. M.; Martínez, G. Pyrolysis of Various Biomass Residues and Char Utilization for the Production of Activated Carbons. *J. Anal. Appl. Pyrolysis* **2009**, 85 (1–2), 134–141. <https://doi.org/10.1016/j.jaap.2008.11.035>.
- [158] Benedetti, V.; Patuzzi, F.; Baratieri, M. Characterization of Char from Biomass Gasification and Its Similarities with Activated Carbon in Adsorption Applications. *Appl. Energy* **2018**, 227, 92–99. <https://doi.org/10.1016/j.apenergy.2017.08.076>.
- [159] Amar, V. S.; Houck, J.; Shende, R. Derived Biochar as Electrode Material for Supercapacitors. In *2019 AIChE Annual Meeting; 2019*.
- [160] Nanofibers, E. P. Carbon Nanofibrous Sponge Made from Hydrothermally Generated Biochar Carbon Nanofibrous Sponge Made from Hydrothermally Generated Biochar and Electrospun Polymer Nanofibers. *Adv. Fiber Mater.* **2020**, 1–11. <https://doi.org/10.1007/s42765-020-00032-0>.
- [161] Yang, J.; Hong, C.; Xing, Y.; Zheng, Z.; Li, Z.; Zhao, X.; Qi, C. Research Progress and Hot Spots of Hydrothermal Liquefaction for Bio-Oil Production Based on Bibliometric Analysis. *Environ. Sci. Pollut. Res.* **2021**, 1–15.
- [162] Cardella, U.; Decker, L.; Sundberg, J.; Klein, H. Process Optimization for Large-Scale Hydrogen Liquefaction. *Int. J. Hydrogen Energy* **2017**, 42 (17), 12339–12354. <https://doi.org/10.1016/j.ijhydene.2017.03.167>.
- [163] Perkins, G.; Batalha, N.; Kumar, A.; Bhaskar, T.; Konarova, M. Recent Advances in

- Liquefaction Technologies for Production of Liquid Hydrocarbon Fuels from Biomass and Carbonaceous Wastes. *Renew. Sustain. Energy Rev.* **2019**, *115*, 109400.
<https://doi.org/10.1016/j.rser.2019.109400>.
- [164] Baloch, H. A.; Nizamuddin, S.; Siddiqui, M. T. H.; Riaz, S.; Sattar, A.; Dumbre, D. K.; Mubarak, N. M.; Srinivasan, M. P.; Gri, G. J. Recent Advances in Production and Upgrading of Bio-Oil from Biomass: A Critical Overview. *J. Environ. Chem. Eng.* **2018**, *6* (4), 5101–5118. <https://doi.org/10.1016/j.jece.2018.07.050>.
- [165] Xiu, S.; Shahbazi, A. Bio-Oil Production and Upgrading Research: A Review. *Renew. Sustain. Energy Rev.* **2012**, *16* (7), 4406–4414. <https://doi.org/10.1016/j.rser.2012.04.028>.
- [166] Song, C.; Hu, H.; Zhu, S.; Wang, G.; Chen, G. Nonisothermal Catalytic Liquefaction of Corn Stalk in Subcritical and Supercritical Water. *Energy & fuels* **2004**, *18* (1), 90–96.
- [167] Tymchyshyn, M.; Xu, C. C. Liquefaction of Bio-Mass in Hot-Compressed Water for the Production of Phenolic Compounds. *Bioresour. Technol.* **2010**, *101* (7), 2483–2490.
<https://doi.org/10.1016/j.biortech.2009.11.091>.
- [168] Elliott, D. C.; Sealock, L. J. Aqueous Catalyst Systems for the Water-Gas Shift Reaction. 1. Comparative Catalyst Studies. *Ind. Eng. Chem. Prod. Res. Dev.* **1983**, *22* (3), 426–431.
- [169] Sinag, A.; Kruse, A.; Rathert, J. Influence of the Heating Rate and the Type of Catalyst on the Formation of Key Intermediates and on the Generation of Gases During Hydrolysis of Glucose in Supercritical Water in a Batch. *Ind. Eng. Chem. Res.* **2004**, *42* (3), 502–508.
- [170] Amar, V. S.; Houck, J. D.; Maddipudi, B.; Penrod, T. A.; Shell, K. M.; Thakkar, A.;

- Shende, A. R.; Hernandez, S.; Kumar, S.; Gupta, R. B.; Shende, R. V. Hydrothermal Liquefaction (HTL) Processing of Unhydrolyzed Solids (UHS) for Hydrochar and Its Use for Asymmetric Supercapacitors with Mixed (Mn,Ti)-Perovskite Oxides. *Renew. Energy* **2021**, *173*, 329–341. <https://doi.org/10.1016/j.renene.2021.03.126>.
- [171] Amar, V. S.; Houck, J. D.; Shende, R. V. Catalytic HTL-Derived Biochar and Sol-Gel Synthesized (Mn, Ti)-Oxides for Asymmetric Supercapacitors. *Int. J. Energy Res.* **2020**, *44* (15), 12546–12558. <https://doi.org/10.1002/er.5938>.
- [172] Mansfield, S. D.; Kim, H.; Lu, F.; Ralph, J. Whole Plant Cell Wall Characterization Using Solution-State 2D NMR. *Nat. Protoc.* **2012**, *7* (9), 1579–1589. <https://doi.org/10.1038/nprot.2012.064>.
- [173] Mottiar, Y.; Vanholme, R.; Boerjan, W.; Ralph, J.; Mansfield, S. D. Designer Lignins: Harnessing the Plasticity of Lignification. *Curr. Opin. Biotechnol.* **2016**, *37*, 190–200. <https://doi.org/10.1016/j.copbio.2015.10.009>.
- [174] Min, D.; Wang, S. F.; Chang, H. M.; Jameel, H.; Lucia, L. Molecular Changes in Corn Stover Lignin Resulting from Pretreatment Chemistry. *BioResources* **2017**, *12* (3), 6262–6275. <https://doi.org/10.15376/biores.12.3.6262-6275>.
- [175] Zhang, Y.; Jiang, Q.; Xie, W.; Wang, Y.; Kang, J. Effects of Temperature, Time and Acidity of Hydrothermal Carbonization on the Hydrochar Properties and Nitrogen Recovery from Corn Stover. *Biomass and Bioenergy* **2019**, *122* (February), 175–182. <https://doi.org/10.1016/j.biombioe.2019.01.035>.
- [176] Mohammed, I. S.; Na, R.; Kushima, K.; Shimizu, N. Investigating the Effect of Processing Parameters on the Products of Hydrothermal Carbonization of Corn Stover. *Sustain.* **2020**,

- 12 (12). <https://doi.org/10.3390/su12125100>.
- [177] Zhang, L.; Wang, Q.; Wang, B.; Yang, G.; Lucia, L. A.; Chen, J. Hydrothermal Carbonization of Corncob Residues for Hydrochar Production. *Energy and Fuels* **2015**, *29* (2), 872–876. <https://doi.org/10.1021/ef502462p>.
- [178] Rinaldi, R.; Jastrzebski, R.; Clough, M. T.; Ralph, J.; Kennema, M.; Bruijninx, P. C. A.; Weckhuysen, B. M. Paving the Way for Lignin Valorisation: Recent Advances in Bioengineering, Biorefining and Catalysis. *Angew. Chemie - Int. Ed.* **2016**, *55* (29), 8164–8215. <https://doi.org/10.1002/anie.201510351>.
- [179] Huang, J. B.; Wu, S. Bin; Cheng, H.; Lei, M.; Liang, J. J.; Tong, H. Theoretical Study of Bond Dissociation Energies for Lignin Model Compounds. *Ranliao Huaxue Xuebao/Journal Fuel Chem. Technol.* **2015**, *43* (4), 429–436. [https://doi.org/10.1016/s1872-5813\(15\)30011-6](https://doi.org/10.1016/s1872-5813(15)30011-6).
- [180] de Caprariis, B.; Bracciale, M. P.; Bavasso, I.; Chen, G.; Damizia, M.; Genova, V.; Marra, F.; Paglia, L.; Pulci, G.; Scarsella, M.; Tai, L.; De Filippis, P. Unsupported Ni Metal Catalyst in Hydrothermal Liquefaction of Oak Wood: Effect of Catalyst Surface Modification. *Sci. Total Environ.* **2020**, *709*, 136215. <https://doi.org/10.1016/j.scitotenv.2019.136215>.
- [181] Hodkiewicz, J. Characterizing Carbon Materials with Raman Spectroscopy. *Thermo Fish. Sci.* **2010**, 1–5.
- [182] Sevilla, M.; Sanchi, C.; Valde, T. Synthesis of Graphitic Carbon Nanostructures from Sawdust and Their Application as Electrocatalyst Supports. *J. Phys. Chem.* **2007**, *111*, 9749–9756.

- [183] Biswal, M.; Banerjee, A.; Deo, M.; Ogale, S. From Dead Leaves to High Energy Density Supercapacitors. *Energy Environ. Sci.* **2013**, *6*, 1249–1259.
<https://doi.org/10.1039/c3ee22325f>.
- [184] Dahawi, Y. A.; Abdulrazik, A.; Abu Seman, M. N.; Abd Aziz, M. A.; Mohd Yunus, M. Y. Aspen Plus Simulation of Bio-Char Production from a Biomass-Based Slow Pyrolysis Process. *Key Eng. Mater.* **2019**, *797*, 336–341.
<https://doi.org/10.4028/www.scientific.net/KEM.797.336>.
- [185] Gupta, R. B.; Demirbas, A. *Gasoline, Diesel, and Ethanol Biofuels from Grasses and Plants*; Cambridge University Press, 2010.
- [186] Lamers, P.; Roni, M. S.; Tumuluru, J. S.; Jacobson, J. J.; Cafferty, K. G.; Hansen, J. K.; Kenney, K.; Teymouri, F.; Bals, B. Techno-Economic Analysis of Decentralized Biomass Processing Depots. *Bioresour. Technol.* **2015**, *194*, 205–213.
<https://doi.org/10.1016/j.biortech.2015.07.009>.
- [187] Thompson, J. L.; Tyner, W. E. Corn Stover for Bioenergy Production: Cost Estimates and Farmer Supply Response. *Biomass and Bioenergy* **2014**, *62*, 166–173.
<https://doi.org/10.1016/j.biombioe.2013.12.020>.
- [188] Sanders, M. Lithium-Ion Battery Raw Material Supply and Demand 2016-2025. In *Advanced Automotive Battery Conference*; 2017.
- [189] Hakala, J.; Kangas, P.; Rintala, L.; Fabritius, T.; Koukkari, P. Biocarbon from Bark or Black Pellets as an Alternative for Coal in Steelmaking – Techno-Economic Evaluation. *Scandinavian J. For. Res.* **2020**, *35* (8), 532–546.

- [190] Olszewski, M.; Kempegowda, R. S.; Skreiberg, Ø.; Wang, L.; Løvås, T. Techno-Economics of Biocarbon Production Processes under Norwegian Conditions. *Energy and Fuels* **2017**, *31* (12), 14338–14356. <https://doi.org/10.1021/acs.energyfuels.6b03441>.
- [191] Pramanik, P.; Patel, H.; Charola, S.; Neogi, S.; Maiti, S. High Surface Area Porous Carbon from Cotton Stalk Agro-Residue for CO₂ adsorption and Study of Techno-Economic Viability of Commercial Production. *J. CO₂ Util.* **2021**, *45* (January), 101450. <https://doi.org/10.1016/j.jcou.2021.101450>.
- [192] Fuertes, A. B.; Arbestain, M. C.; Sevilla, M.; MacIá-Agulló, J. A.; Fiol, S.; López, R.; Smernik, R. J.; Aitkenhead, W. P.; Arce, F.; MacIas, F. Chemical and Structural Properties of Carbonaceous Products Obtained by Pyrolysis and Hydrothermal Carbonisation of Corn Stover. *Aust. J. Soil Res.* **2010**, *48* (6–7), 618–626. <https://doi.org/10.1071/SR10010>.
- [193] Lang, H. J. Simplified Approach to Preliminary Cost Estimates. *Chem. Eng.* **1948**, *55* (6), 112–113.
- [194] Saeed, W. ESTIMATION OF OPERATING COSTS.
- [195] Kumar, R.; Singh, S.; Singh, O. V. Bioconversion of Lignocellulosic Biomass: Biochemical and Molecular Perspectives. **2008**, 377–391. <https://doi.org/10.1007/s10295-008-0327-8>.
- [196] Thakkar, A.; Shell, K. M.; Bertosin, M.; Rodene, D. D.; Amar, V.; Bertuccio, A.; Gupta, R. B.; Shende, R.; Kumar, S. Production of Levulinic Acid and Biocarbon Electrode Material from Corn Stover through an Integrated Biorefinery Process. *Fuel Process. Technol.* **2020**, No. October, 106644. <https://doi.org/10.1016/j.fuproc.2020.106644>.

- [197] Popov, S.; Ruhl, I.; Uppugundla Sousa, N. L. da C.; Balan, V.; Hatcher, P. G.; Kumar, S. Bio-Oil via Catalytic Liquefaction of Unhydrolyzed Solids in Aqueous Medium.Pdf. *Biofuels* **2014**, *5* (4), 431–446.
- [198] Hu, Y.; Gu, Z.; Li, W.; Xu, C. C. Alkali-Catalyzed Liquefaction of Pinewood Sawdust in Ethanol / Water. *Biomass and Bioenergy* **2020**, *134* (December 2019), 105485. <https://doi.org/10.1016/j.biombioe.2020.105485>.
- [199] Wang, Z.; Wang, F.; Cao, J.; Wang, J. Pyrolysis of Pine Wood in a Slowly Heating Fixed-Bed Reactor : Potassium Carbonate versus Calcium Hydroxide as a Catalyst. *Fuel Process. Technol.* **2010**, *91* (8), 942–950. <https://doi.org/10.1016/j.fuproc.2009.09.015>.
- [200] Ioannidou, O.; Zabaniotou, A.; Antonakou, E. V; Papazisi, K. M.; Lappas, A. A.; Athanassiou, C. Investigating the Potential for Energy , Fuel , Materials and Chemicals Production from Corn Residues (Cobs and Stalks) by Non-Catalytic and Catalytic Pyrolysis in Two Reactor Configurations. *Renew. Sustain. Energy Rev.* **2009**, *13* (4), 750–762. <https://doi.org/10.1016/j.rser.2008.01.004>.
- [201] Krishna, B. B.; Singh, R.; Bhaskar, T. Effect of Catalyst Contact on the Pyrolysis of Wheat Straw and Wheat Husk. *Fuel* **2015**, *160*, 64–70. <https://doi.org/10.1016/j.fuel.2015.07.065>.
- [202] Zhu, Z.; Sohail, S.; Rosendahl, L.; Yu, D.; Chen, G. Influence of Alkali Catalyst on Product Yield and Properties via Hydrothermal Liquefaction of Barley Straw. *Energy* **2015**, *80*, 284–292. <https://doi.org/10.1016/j.energy.2014.11.071>.
- [203] Yim, S.; Cheng, S.; Quitain, A. T.; Yusup, S.; Sasaki, M.; Uemura, Y.; Kida, T. Metal Oxide-Catalyzed Hydrothermal Liquefaction of Malaysian Oil Palm Biomass to Bio-Oil

- under Supercritical Condition. *J. Supercrit. Fluids* **2017**, *120*, 384–394.
<https://doi.org/10.1016/j.supflu.2016.05.044>.
- [204] Cheng, S.; Wei, L.; Julson, J.; Ram, P.; Cao, Y.; Gu, Z. Catalytic Liquefaction of Pine Sawdust for Biofuel Development on Bifunctional Zn/HZSM-5 Catalyst in Supercritical Ethanol. *J. Anal. Appl. Pyrolysis* **2017**, *126*, 257–266.
<https://doi.org/10.1016/j.jaap.2017.06.001>.
- [205] Schmieder, H.; Abeln, J.; Boukis, N.; Dinjus, E.; Kruse, A.; Kluth, M.; Petrich, G.; Sadri, E.; Schacht, M. Hydrothermal Gasification of Biomass and Organic Wastes. *J. Supercrit. Fluids* **2000**, *17*, 145–153.
- [206] Cheng, S.; Wei, L.; Alsowij, M.; Corbin, F.; Boakye, E.; Gu, Z. Catalytic Hydrothermal Liquefaction (HTL) of Biomass for Bio-Crude Production Using Ni / HZSM-5 Catalysts. *AIMS Env. Sci* **2017**, *4* (April), 417–430. <https://doi.org/10.3934/environsci.2017.3.417>.
- [207] Zhu, H.; Wang, X.; Yang, F.; Yang, X. Promising Carbons for Supercapacitors Derived from Fungi. *Adv. Mater.* **2011**, *23* (24), 2745–2748.
<https://doi.org/10.1002/adma.201100901>.
- [208] Chen, W.; Zhang, H.; Huang, Y.; Wang, W. A Fish Scale Based Hierarchical Lamellar Porous Carbon Material Obtained Using a Natural Template for High Performance Electrochemical Capacitors. *J. Mater. Chem.* **2010**, *20* (23), 4773–4775.
<https://doi.org/10.1039/c0jm00382d>.
- [209] Raymundo-Piñero, E.; Cadek, M.; Béguin, F. Tuning Carbon Materials for Supercapacitors by Direct Pyrolysis of Seaweeds. *Adv. Funct. Mater.* **2009**, *19* (7), 1032–1039. <https://doi.org/10.1002/adfm.200801057>.

- [210] Peng, C.; Yan, X. Bin; Wang, R. T.; Lang, J. W.; Ou, Y. J.; Xue, Q. J. Promising Activated Carbons Derived from Waste Tea-Leaves and Their Application in High Performance Supercapacitors Electrodes. *Electrochim. Acta* **2013**, *87*, 401–408. <https://doi.org/10.1016/j.electacta.2012.09.082>.
- [211] Kalpana, D.; Cho, S. H.; Lee, S. B.; Lee, Y. S.; Misra, R.; Renganathan, N. G. Recycled Waste Paper-A New Source of Raw Material for Electric Double-Layer Capacitors. *J. Power Sources* **2009**, *190* (2), 587–591. <https://doi.org/10.1016/j.jpowsour.2009.01.058>.
- [212] Lv, Y.; Gan, L.; Liu, M.; Xiong, W.; Xu, Z.; Zhu, D.; Wright, D. S. A Self-Template Synthesis of Hierarchical Porous Carbon Foams Based on Banana Peel for Supercapacitor Electrodes. *J. Power Sources* **2012**, *209*, 152–157. <https://doi.org/10.1016/j.jpowsour.2012.02.089>.
- [213] Li, X.; Xing, W.; Zhuo, S.; Zhou, J.; Li, F.; Qiao, S. Z.; Lu, G. Q. Preparation of Capacitor's Electrode from Sunflower Seed Shell. *Bioresour. Technol.* **2011**, *102* (2), 1118–1123. <https://doi.org/10.1016/j.biortech.2010.08.110>.
- [214] Li, X.; Han, C.; Chen, X.; Shi, C. Preparation and Performance of Straw Based Activated Carbon for Supercapacitor in Non-Aqueous Electrolytes. *Microporous Mesoporous Mater.* **2010**, *131* (1–3), 303–309. <https://doi.org/10.1016/j.micromeso.2010.01.007>.
- [215] Yun, Y. S.; Cho, S. Y.; Shim, J.; Kim, B. H.; Chang, S. J.; Baek, S. J.; Huh, Y. S.; Tak, Y.; Park, Y. W.; Park, S.; Jin, H. J. Microporous Carbon Nanoplates from Regenerated Silk Proteins for Supercapacitors. *Adv. Mater.* **2013**, *25* (14), 1993–1998. <https://doi.org/10.1002/adma.201204692>.
- [216] Zhang, L.; Zhang, F.; Yang, X.; Leng, K.; Huang, Y.; Chen, Y. High-Performance

- Supercapacitor Electrode Materials Prepared from Various Pollens. *Small* **2013**, *9* (8), 1342–1347. <https://doi.org/10.1002/sml.201202943>.
- [217] Kuratani, K.; Okuno, K.; Iwaki, T.; Kato, M.; Takeichi, N.; Miyuki, T.; Awazu, T.; Majima, M.; Sakai, T. Converting Rice Husk Activated Carbon into Active Material for Capacitor Using Three-Dimensional Porous Current Collector. *J. Power Sources* **2011**, *196* (24), 10788–10790. <https://doi.org/10.1016/j.jpowsour.2011.09.001>.
- [218] Huang, W.; Zhang, H.; Huang, Y.; Wang, W.; Wei, S. Hierarchical Porous Carbon Obtained from Animal Bone and Evaluation in Electric Double-Layer Capacitors. *Carbon N. Y.* **2011**, *49* (3), 838–843. <https://doi.org/10.1016/j.carbon.2010.10.025>.
- [219] Olivares-Marín, M.; Fernández, J. A.; Lázaro, M. J.; Fernández-González, C.; Macías-García, A.; Gómez-Serrano, V.; Stoeckli, F.; Centeno, T. A. Cherry Stones as Precursor of Activated Carbons for Supercapacitors. *Mater. Chem. Phys.* **2009**, *114* (1), 323–327. <https://doi.org/10.1016/j.matchemphys.2008.09.010>.
- [220] Wu, F. C.; Tseng, R. L.; Hu, C. C.; Wang, C. C. Effects of Pore Structure and Electrolyte on the Capacitive Characteristics of Steam- and KOH-Activated Carbons for Supercapacitors. *J. Power Sources* **2005**, *144* (1), 302–309. <https://doi.org/10.1016/j.jpowsour.2004.12.020>.
- [221] Sun, L.; Tian, C.; Li, M.; Meng, X.; Wang, L.; Wang, R.; Yin, J.; Fu, H. From Coconut Shell to Porous Graphene-like Nanosheets for High-Power Supercapacitors. *J. Mater. Chem. A* **2013**, *1* (21), 6462–6470. <https://doi.org/10.1039/c3ta10897j>.
- [222] Zhang, W.; Zhao, M.; Liu, R.; Wang, X.; Lin, H. Hierarchical Porous Carbon Derived from Lignin for High Performance Supercapacitor. *Colloids Surfaces A Physicochem.*

Eng. Asp. **2015**, *484*, 518–527. <https://doi.org/10.1016/j.colsurfa.2015.08.030>.

- [223] Wang, K.; Cao, Y.; Wang, X.; Castro, M. A.; Luo, B.; Gu, Z.; Liu, J.; Hoefelmeyer, J. D.; Fan, Q. Rod-Shape Porous Carbon Derived from Aniline Modified Lignin for Symmetric Supercapacitors. *J. Power Sources* **2016**, *307*, 462–467. <https://doi.org/10.1016/j.jpowsour.2016.01.008>.
- [224] Hu, S.; Zhang, S.; Pan, N.; Hsieh, Y. Lo. High Energy Density Supercapacitors from Lignin Derived Submicron Activated Carbon Fibers in Aqueous Electrolytes. *J. Power Sources* **2014**, *270* (x), 106–112. <https://doi.org/10.1016/j.jpowsour.2014.07.063>.
- [225] Demir, M. *Renewable Carbon from Lignin Biomass and Its Electrode and Catalyst Applications in Batteries, Supercapacitors, and Fuel Cells*; (Doctoral dissertation, Virginia Commonwealth University), 2017.

Appendix A1. Electrode and Coin Cell Fabrication

Fabrication of a working electrode is the first step in gaining electrochemical performance results. It is important to ensure each electrode is very similar to identical. To ensure this, the following steps are taken for every electrode fabricated and discussed in this dissertation:

1. A 1 cm x 3 cm sliver of nickel foam is cut from a bulk roll.
2. The nickel foam sliver is washed in 1 M HCl and sonicated for 10 mins to further reduce the nickel. Nickel oxide can cause internal resistances to increase. Post sonication the excess HCl is decanted.
3. The nickel foam is washed with ethanol and sonicated for 10 mins, then decanted.
4. Milli Q water is added to further neutralize the nickel foam. An additional 10 mins of sonication is performed, then the excess is decanted.
5. The reduced nickel foam is placed in a vacuum oven at -60 kPa and 40 °C for 1 hr.
6. Post drying, the nickel foam sliver is weighed and given an identifier.
7. Electrode ink is prepared by taking the prepared biocarbon, Super P (conductive carbon) and PTFE (60 wt.% in water) and mixing into a homogenous slurry. A few drops of Milli Q water are added to help with the mixing process. Note: It is important to only add enough water to form a paste-like consistency. A slurry that contains an excess of water will bleed through the nickel foam when applied to the electrode surface.
8. The electrode ink is spread evenly onto one end of the nickel foam. Since electrodes are prepared in triplicate, caution is practiced to ensure that all electrodes receive an even layer with the same prepared electrode ink.
9. Electrodes are placed in the vacuum oven at -60 kPa and 40 °C overnight to dry.

10. The next day, electrodes are taken out, weighed, and placed under a label identifying the electrode. Pictures are taken of the electrode next to a reference object (Figure A1.1 [Left]). The reference object can be anything that does not significantly change in size based on normal STP conditions. In the case of this dissertation, the reference object is an American nickel.
11. The electrodes are pressed using an Across International pneumatic press between two steel plates. This is to ensure that the thickness of the ink at the electrode surface is homogenous. Variances in ink thickness can cause skewed results during electrochemical testing.
12. Once pressed, chemical resistant epoxy is applied to the electrode surface and allowed to cure overnight. The goal is to ensure that only the electrode material is exposed and the nickel foam is insulated from the electrolyte. The electrolyte will react with the metal causing skewed electrochemical results.
13. On the following day pictures are taken of the epoxied electrode with the reference object (Figure A1 [Right]). Active mass calculations are performed utilizing images taken during electrode fabrication. Pixel areas of the electrode surfaces and reference object are determined using ImageJ software. Equation 5.1 discussed in Chapter 5 is used for calculating the active mass.
14. When the active mass calculations are complete, the electrode is ready for electrochemical testing.



Figure A1.1. [Left] nickel foam with electrode ink and reference object (U.S. nickel) prior to templating and [Right] the electrode and reference object post templating.

Coin cell fabrication is important in determining the real-world performance of a supercapacitor. For the purposes of this dissertation coin cells were generally fabricated for long term stability testing. This is primarily due to the absence of electrolyte evaporation that generally occurs in 2-cell and 3-cell experiments. The following procedure is used when fabricating a coin cell supercapacitor:

1. A strip of nickel foam ~ 2.5 cm x 5 cm is cut from the bulk roll and washed in the same manner at steps 2-5 above.
2. Electrode ink is prepared in the same manner as step 7 above. Note: A larger quantity of ink needs to be prepared as the electrode surfaces inside of a coin cell are much greater than that of a single prepared electrode.
3. Electrode ink is applied in an even layer to the reduced nickel foam surface, covering the majority of the surface.
4. The electrode strip is dried overnight in a vacuum oven at -60 kPa and 40 °C overnight.
5. The electrode strip is pressed in accordance with step 11 above.

6. The pressed electrode strip is inserted into an MTI Corp. Precision Disk Cutter outfitted with a CR 2032 battery die. Two identical disks are cut from the one electrode and retrieved.
7. The disks are weighed and given an identifier.
8. The active mass of each electrode is determined from subtracting the mass of the working electrodes from previously cut reference electrodes. These reference electrodes do not contain any electrode material.
9. A CR 2032 coin cell supercapacitor is assembled utilizing the scheme in Figure A1.2.
10. The assembled coin cell supercapacitor is placed in an MTI digital pressure controlled electric crimper set to 0.8 T and crimped together.
11. Once crimped, the coin cell is ready to undergo electrochemical performance testing.

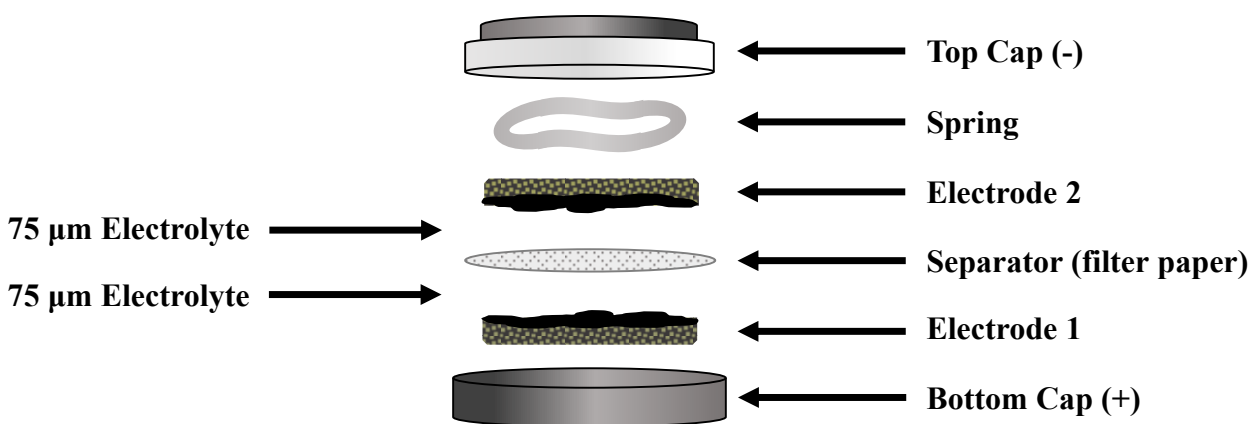


Figure A1.2. Components required for coin cell supercapacitor fabrication in order of application.

Appendix A2. Electrochemical Test Set-up

There are three different methods for electrochemical performance testing presented in this dissertation, each having a particular importance. The first and most common set-up is 3-Cell or 3-Electrode. Here, ideal properties of the electrode can be analyzed and the potential versus the reference is determined. In this method there is a working, counter, and reference electrode. The working electrode is the one that is being tested for its electrochemical properties (fabricated). The counter is generally comprised of Pt or other noble metal and is used to complete the circuit. The reference electrode's purpose is to provide a stable potential for the working electrode. An ideal reference electrode does not pass current through the working electrode and has zero impedance. For all experiments presented, the reference electrode is an Ag/AgCl in a saturated KCl solution with a potential of 0.197 v. NHE.

In a 2-cell (2-electrode) system, there is only an anode and cathode and can provide a closer to real world look at electrochemical performance. In the case of EDLC's both the anode and cathode are the same. When testing on the potentiostat, the reference lead (white) is clipped onto the counter electrode's lead (Figure A2.1). Here, there is a potential difference between the anode and cathode creating the voltage of the pseudo supercapacitor.

The final method of electrochemical testing presented is through a coin cell system. As stated in Appendix A1. coin cells give the real-world electrochemical performance data of the biocarbon material. Within the coin cells are two identical electrodes with a separator between them. A small amount of electrolyte provides the bulk transport fluid for the system. During testing, the supercapacitor is clipped into a coin cell holder with the working lead attached to the positive (+) post and the reference/counter attached to the negative (-) post.

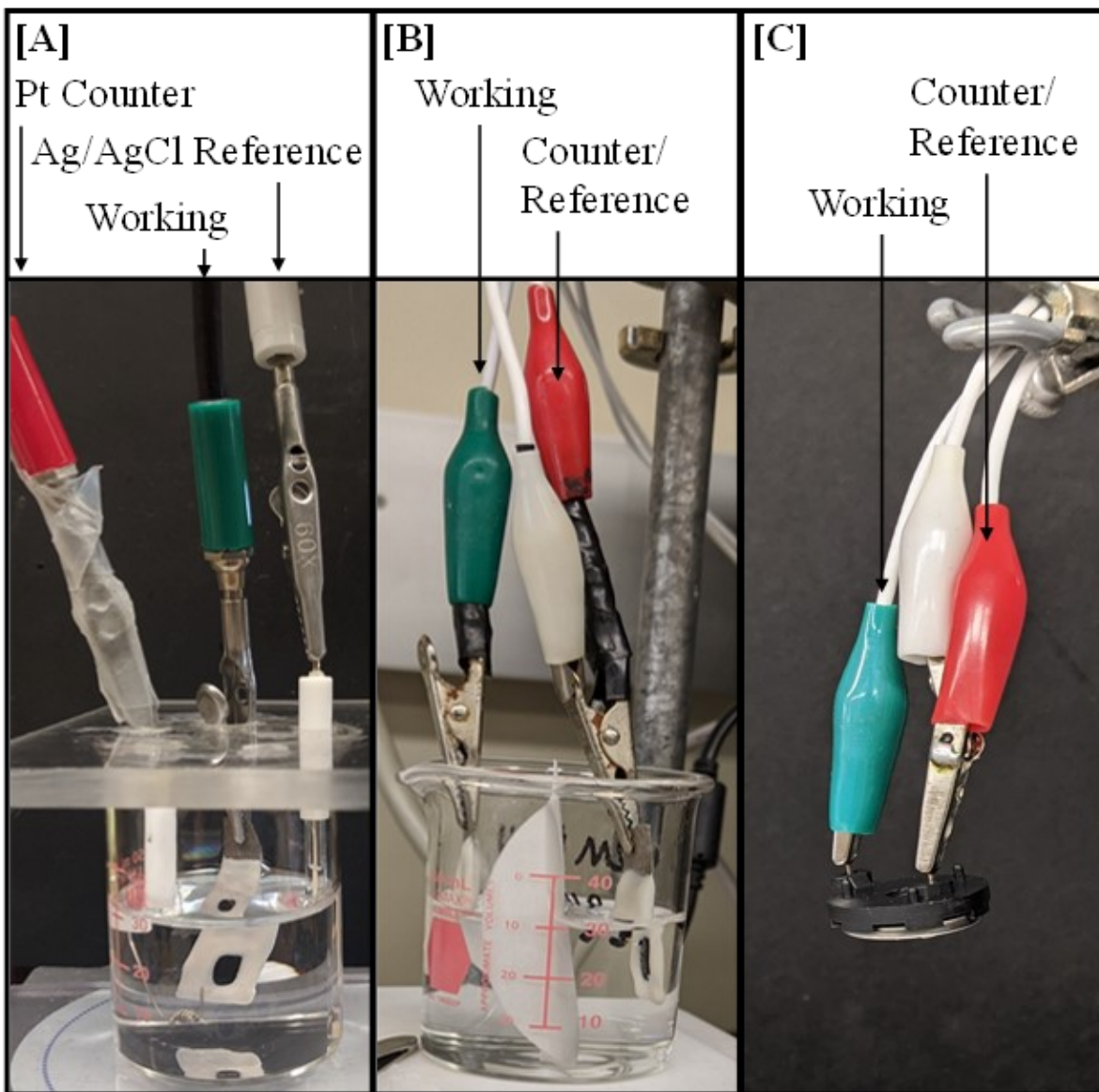


Figure A2.1. Electrochemical test setup for [A] 3-cell, [B] 2-cell, [C] coin cell.

Appendix A3. CHI Code for Electrochemical Testing 3-Cell

```
# Welcome to Macro Command!  
#  
# Use this dialog box to execute a series of commands.  
# This is analogous to batch files in Windows or shell scripts in Unix/Linux.  
# Click the 'Help' button for more information.  
# -----
```

```
#CV
```

```
tech:cv  
ei=0  
eh=0  
el=-1  
v=0.005  
cl=8  
sens=1e-2  
run  
folder: C:\CHI Users\Katelyn\2D Electrodes 11_13_20\E3 WH-C A  
save: cv 5 mv per s 2M KOH R  
tsave: cv 5 mv per s 2MKOH R
```

```
tech:cv  
ei=0  
eh=0  
el=-1  
v=0.1  
cl=8  
sens=1e-2  
run  
folder: C:\CHI Users\Katelyn\2D Electrodes 11_13_20\E3 WH-C A  
save: 100 mv per s 2 M KOH R  
tsave: 100 mv per s 2M KOH R
```

```
tech:cv  
ei=0  
eh=0  
el=-1  
v=0.02  
cl=8  
sens=1e-2  
run  
folder: C:\CHI Users\Katelyn\2D Electrodes 11_13_20\E3 WH-C A  
save: 20 mv per s 2M KOH R
```

tsave: 20 mv per s 2M KOH R

tech:cv

ei=0

eh=0

el=-1

v=0.005

cl=8

sens=1e-2

run

folder: C:\CHI Users\Katelyn\2D Electrodes 11_13_20\E3 WH-C A

save: 5 mv per s 2M KOH R2

tsave: 5 mv per s 2M KOH R2

tech:cv

ei=0

eh=0

el=-1

v=0.05

cl=8

sens=1e-2

run

folder: C:\CHI Users\Katelyn\2D Electrodes 11_13_20\E3 WH-C A

save: 50 mv per s 2M KOH

tsave: 50 mv per s 2M KOH

tech:cv

ei=0

eh=0

el=-1

v=0.1

cl=8

sens=1e-2

run

folder: C:\CHI Users\Katelyn\2D Electrodes 11_13_20\E3 WH-C A

save: 100 mv per s 2M KOH R2

tsave: 100 mv per s 2M KOH R2

tech:cp

ic=0.00034

ia=0.00034

eh=0

heht=0

el=-1

tc=10

ta=10

pn:p
si=1
cl=21
prioe
run
folder: C:\CHI Users\Katelyn\2D Electrodes 11_13_20\E3 WH-C A
save: 0.1 A per g 2M KOH
tsave: 0.1 A per g 2M KOH

tech:cp
ic=0.0034
ia=0.0034
eh=0
heht=0
el=-1
tc=10
ta=10
pn:p
si=1
cl=21
prioe
run
folder: C:\CHI Users\Katelyn\2D Electrodes 11_13_20\E3 WH-C A
save: 1 A per g 2M KOH
tsave: 1 A per g 2M KOH

tech:cp
ic=0.0102
ia=0.0102
eh=0
heht=0
el=-1
tc=10
ta=10
pn:p
si=1
cl=21
prioe
run
folder: C:\CHI Users\Katelyn\2D Electrodes 11_13_20\E3 WH-C A
save: 3 A per g 2M KOH
tsave: 3 A per g 2M KOH

tech:cp
ic=0.017
ia=0.017

eh=0
heht=0
el=-1
tc=10
ta=10
pn:p
si=1
cl=21
prioe
run
folder: C:\CHI Users\Katelyn\2D Electrodes 11_13_20\E3 WH-C A
save: 5 A per g 2M KOH
tsave: 5 A per g 2M KOH

tech:cp
ic=0.034
ia=0.034
eh=0
heht=0
el=-1
tc=10
ta=10
pn:p
si=1
cl=21
prioe
run
folder: C:\CHI Users\Katelyn\2D Electrodes 11_13_20\E3 WH-C A
save: 10 A per g 2M KOH
tsave: 10 A per g 2M KOH

tech:imp
ei=0
fl= 0.01
fh=100000
amp=0.005
qt=2
impsf
ibias=1
run
folder: C:\CHI Users\Katelyn\2D Electrodes 11_13_20\E3 WH-C A
save: EIS 0.01_100000 2M KOH
tsave: EIS 0.01_100000 2M KOHKOH

Appendix A4. CHI Code for Electrochemical Testing 2-Cell

```
# Welcome to Macro Command!  
#  
# Use this dialog box to execute a series of commands.  
# This is analogous to batch files in Windows or shell scripts in Unix/Linux.  
# Click the 'Help' button for more information.  
# -----
```

```
#CV
```

```
tech:cv  
ei=0  
eh=0  
el=-1  
v=0.005  
cl=12  
sens=1e-2  
run  
folder: C:\CHI Users\Katelyn\2D Electrodes 11_30_20\E3 WH-5 2 Cell  
save: cv 5 mv per s 2M KOH R  
tsave: cv 5 mv per s 2MKOH R
```

```
tech:cp  
ic=0.00014  
ia=0.00014  
eh=0  
heht=0  
el=-1  
tc=10  
ta=10  
pn:p  
si=1  
cl=11  
prioe  
run  
folder: C:\CHI Users\Katelyn\2D Electrodes 11_30_20\E3 WH-5 2 Cell  
save: 0.1 A per g 2M KOH  
tsave: 0.1 A per g 2M KOH
```

```
tech:cp  
ic=0.0014  
ia=0.0014  
eh=0
```

heht=0
el=-1
tc=10
ta=10
pn:p
si=1
cl=11
prioe
run
folder: C:\CHI Users\Katelyn\2D Electrodes 11_30_20\E3 WH-5 2 Cell
save: 1 A per g 2M KOH
tsave: 1 A per g 2M KOH

tech:cp
ic=0.0042
ia=0.0042
eh=0
heht=0
el=-1
tc=10
ta=10
pn:p
si=1
cl=11
prioe
run
folder: C:\CHI Users\Katelyn\2D Electrodes 11_30_20\E3 WH-5 2 Cell
save: 3 A per g 2M KOH
tsave: 3 A per g 2M KOH

tech:cp
ic=0.007
ia=0.007
eh=0
heht=0
el=-1
tc=10
ta=10
pn:p
si=1
cl=11
prioe
run
folder: C:\CHI Users\Katelyn\2D Electrodes 11_30_20\E3 WH-5 2 Cell
save: 5 A per g 2M KOH
tsave: 5 A per g 2M KOH

tech:cp
ic=0.014
ia=0.014
eh=0
heht=0
el=-1
tc=10
ta=10
pn:p
si=1
cl=11
prioe
run
folder: C:\CHI Users\Katelyn\2D Electrodes 11_30_20\E3 WH-5 2 Cell
save: 10 A per g 2M KOH
tsave: 10 A per g 2M KOH

Appendix A5. VBA Code for Long Term

Chronopotentiometry

```
Sub Specific_Capacity4()
'Labels the raw data for easy cycle separation
'For Katelyns Supercapacitors with =IF(AND(B1596>B1595,
B1596>B1597),"Max",IF(AND(B1596<B1595, B1596<B1597),"min","")) in column C.
'Copy and paste values from column C into column D and run
'Also, after 1,000 seconds the seconds have to be manually updated before running

Dim LVolt As Double, UVolt As Double
Dim i As Long, k As Double, j As Double, kk As Double
Dim t As Double, tt As Double, ttt As Double
Dim ii As Integer, TimeS As Double
Dim A As Double, jj As Integer, TimeH As Double, mA As Double, g As Double

'LVolt = InputBox("Enter Lower Limit for Voltage", "Voltage Input", 2.7)
'UVolt = InputBox("Enter Upper Cut Off Voltage Limit", "Voltage Input", 4.5)

'counters
i = 1 'cycle counter
j = 0 'segment counter
'jj = 0 'column counter
k = 5 'row counter
kk = 5 'space counter

'Time constants
t = Cells(k, 1) 'time at max
tt = 0 'time at min
'ttt = 0

Do While Cells(k + 1, 2).Value <> ""
    If Cells(k, 4) = "Max" Then
        'Charge

        t = Cells(k, 1)
        Cells(k, 6) = t - tt 'time output

        Cells(k, 5) = i 'cycle number
```

```

i = i + 1

ElseIf Cells(k, 4) = "min" Then
'Discharge

tt = Cells(k, 1)
Cells(k, 6 + 2) = tt - t 'time output
Cells(k, 5 + 2) = i

End If

k = k + 1
Loop

k = 5 'reset counter

Do While Cells(k + 1, 2).Value <> ""
If Cells(k, 5) <> "" Then
Cells(kk, 5 + 4) = Cells(k, 5)
Cells(kk, 6 + 4) = Cells(k, 6)
kk = kk + 1

End If
k = k + 1
Loop

k = 5 'reset counter
kk = 5 'reset counter

Do While Cells(k + 1, 2).Value <> ""
If Cells(k, 5 + 2) <> "" Then
Cells(kk, 5 + 2 + 4) = Cells(k, 5 + 2)
Cells(kk, 6 + 2 + 4) = Cells(k, 6 + 2)
kk = kk + 1

End If
k = k + 1
Loop

"Add titles
'Cells(22, 5) = "Time (h)"
'Cells(22, 6) = "Specific Capacity (mA h/g)"

"Time conversion to hours
'ii = 1
'Do While Cells(22 + ii, 7).Value <> ""

```

```

' TimeS = Cells(22 + ii, 1)
' Cells(22 + ii, 5) = TimeS / 3600
' ii = ii + 1
'Loop

"Specific Capacity
'jj = 1
'A = InputBox("Enter Amps Used to Run CD", "Amps Input", 0.0001056)
'g = InputBox("Enter Weight of Active Material On The Electrode", "Active Material Weight,
g", 0.00264)
'mA = A * 1000
'Cells(10, 4) = mA
'Cells(10, 5) = "mA"
'Cells(11, 4) = g
'Cells(11, 5) = "g"
'Do While Cells(22 + jj, 7).Value <> ""
' TimeH = Cells(22 + jj, 5)
' Cells(22 + jj, 6) = TimeH * mA / g
' jj = jj + 1
'Loop

End Sub

```

Appendix A6. Supplemental for Supercapacitor Performance of Biocarbon Produced from Non-catalytic Hydrothermal Liquefaction of Corn Stover Biomass

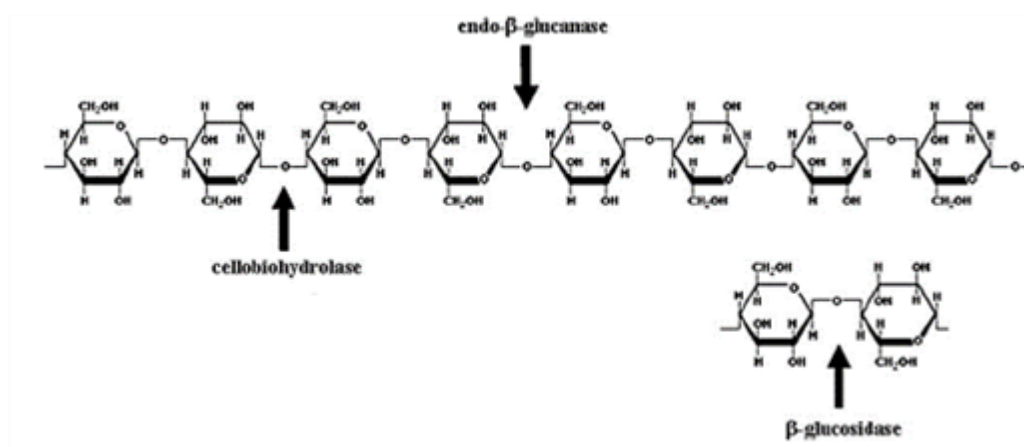


Figure A6.1. Molecular structure of cellulose and site of action of endoglucanases, exoglucanases (cellobiohydrolase), and β -glucosidases [195].

Cellulose is a homopolysaccharide composed of β -(1 \rightarrow 4) linked D-glucose units. The cellulase enzyme blend used for hydrolysis of cellulose into glucose is made up of endoglucanases, exoglucanases, and β -glucosidases. The endoglucanases randomly break internal bonds of the cellulose polysaccharide, while exoglucanases attack the chain ends, releasing cellobiose (disaccharide). Glucose monomer is released by the action of β -glucosidases on cellobiose [195]. The efficiency of these enzymes is limited due to the complex structure of lignocellulosic biomass. Therefore, lignocellulosic biomass is subjected to pretreatment before enzymatic hydrolysis. Pretreatment helps in removing the structural barriers like lignin and hemicellulose from the biomass [196]. It also alters physical properties of the biomass like surface area, pore size, crystallinity, and degree of polymerization [35]. The solid residue that cannot be hydrolyzed by enzymes is called unhydrolyzed solids (UHS). It is generally composed of lignin, bound enzymes, undigested carbohydrates, and ash [35],[197].

Table A6.1. Literature values of HTL processing conditions and products obtained

Feedstock	Catalyst used	Processing Conditions	Products	Reference
Pinewood saw dust	Na ₂ CO ₃ /NaOH	300 °C, 30 min, 10 wt% (catalyst)	Biocrude oil – 48%	[198]
Pinewood	Ca(OH) ₂	350 °C, 0.28:1 ratio (catalyst to biomass)	Bio-oil – 40.8 Biochar – 46.2 Gas yield – 11.6	[199]
Corn stalk (cob)	Commercial fluid catalytic cracking (FCC) unit	500 °C, 0.7:1.5 (catalyst to biomass)	Bio-oil – 41.18 Biochar – 30.62 Gas yield – 15.29	[200]
Wheat Straw	Mordenite	350 °C, 0.1:1(catalyst to biomass)	Bio-oil – 24.5 Biochar – 34.2 Gas yield – 35.9	[201]
Barley Straw	K ₂ CO ₃	280-400 °C, 11.2 MPa	Increased Oil yield (34.85%) High phenolic compounds to biooil Char reduction	[202]
Empty Fruit Bunch	CaO, MnO, MgO, SnO, CeO ₂ , NiO, La ₂ O ₃ , Al ₂ O ₃	390 °C, 25 MPa	Maximized bio-oil for 1.4 times with CeO ₂ , MnO, CaO, and La ₂ O ₃ catalysts	[203]
Pine sawdust	Zn/HZSM-5 (supercritical ethanol)	300 °C, 17.62 MPa	High biocrude yield at 59.09% Biofuel with high hydrocarbon content at 15.03%	[204]
Wet biomass, Organic wastes	KOH, K ₂ CO ₃	550-600 °C, 25 MPa	Degradation of hydrocarbons to <1 vol%	[205]
Pine sawdust (PSD)	K ₂ CO ₃ , Ni/HZSM-5	300 °C, initial N ₂ pressure 10 psi, 1 hr.	Biocrude yield – 60% Solid Residue – 25% Gas yield – 15%	[206]
Pinewood	Ni(NO ₃) ₂ , Ca(NO ₃) ₂ , Co(NO ₃) ₂ , Fe(NO ₃) ₂	1:10, 1:30, 1:75 biomass to solvent(B:S) ratio, 225-275 °C, 30-120 min.	Higher H ₂ of 12.25 mol% at 250 °C, Maximum biocrude of 55 wt% at 250 °C, Higher lactic acid of 83.92 wt% at 1:75(B:S), 250 °C	[102]

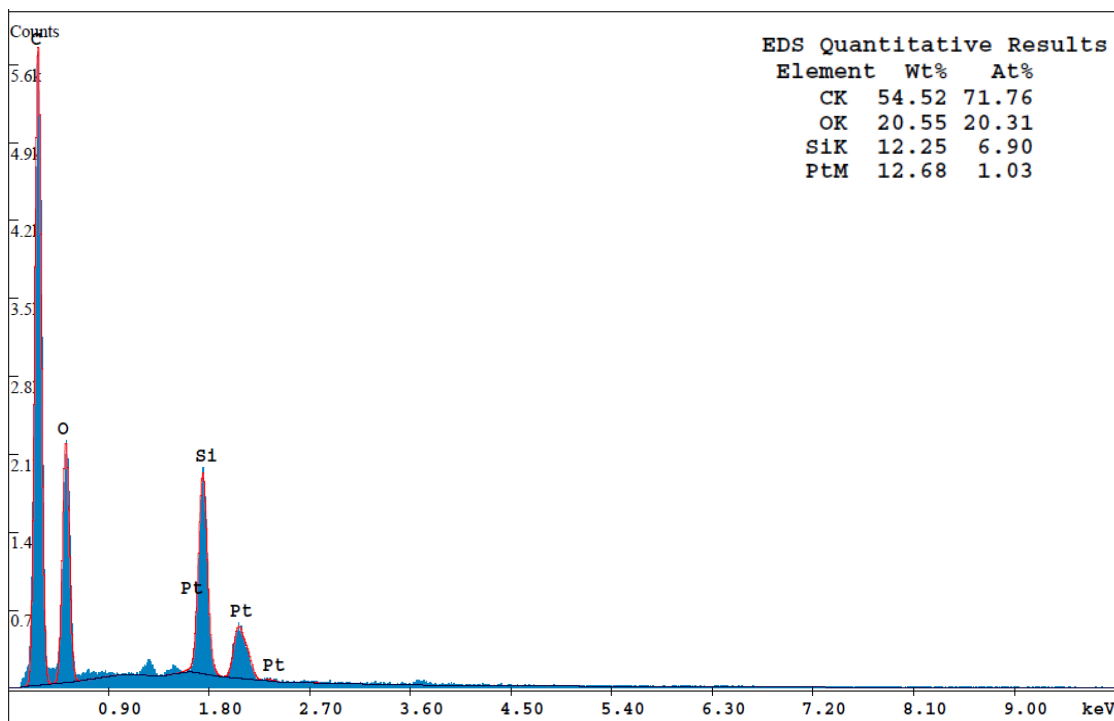


Figure A6.2. EDAX elemental spectra and subsequent elemental weight and atomic percentages are shown for UHS-SDC9. Platinum was detected from a typical sample preparation technique involving Pt sputtering of the sample stage prior to SEM imaging.

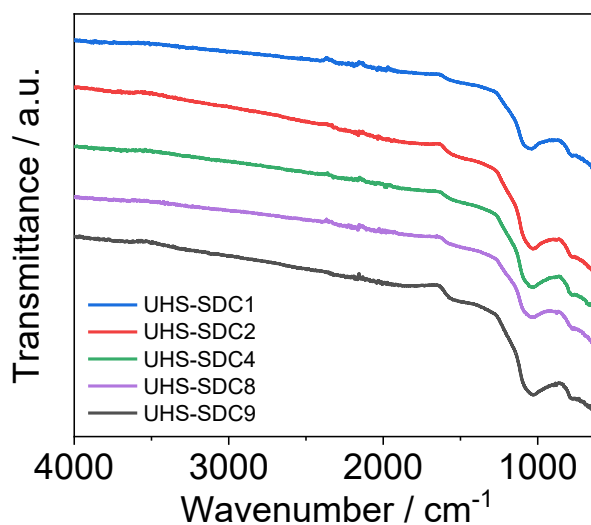


Figure A6.3. ATR-FTIR of biocarbon of UHS-SDC1, UHS-SDC2, UHS-SDC4, UHS-SDC8, and UHS-SDC9.

Table 6.S2. HTL processing parameters and physical characteristics of the prepared biocarbons, including electrochemical, BET, and Raman results, where applicable.

Sample Name	HTL Parameters				Physical Characteristics					
	Mass	Temperature	Initial Pressure	Reaction time	Specific Capacitance at 5 mV s ⁻¹	Specific Capacitance at 0.05 A g ⁻¹	Energy Density	S _{BET} SSA	Pore Volume	I _g I _d ⁻¹
	g	°C	psig	h	F g ⁻¹	F g ⁻¹	Wh kg ⁻¹	m ² g ⁻¹	cm ³ g ⁻¹	--
UHS-SDC1	15	250	40	1	173	119	2.8	272	0.12	1.17
UHS-SDC2	15	275	40	1	154	104	7.8	240	0.09	1.11
UHS-SDC3	15	300	40	1	161	111	--	--	--	1.00
UHS-SDC4	15	275	0	1	180	125	8.4	80	0.03	0.98
UHS-SDC5	15	275	100	1	139	96	--	--	--	1.03
UHS-SDC6	15	275	150	1	168	126	--	--	--	1.00
UHS-SDC7	15	275	40	0.5	184	130	--	270	0.11	1.07
UHS-SDC8	15	275	40	2	207	160	5.2	211	0.08	1.03
UHS-SDC9	5	275	40	1	242	190	9.9	215	0.12	1.07
UHS-SDC10	25	275	40	1	188	162	--	--	--	1.09

Appendix A7. Supplemental for Phytoremediation of Nickel via Water Hyacinth for Biocarbon-derived Supercapacitor Applications



Figure A7.1. Hydroponic system setup for cultivation of water hyacinth.

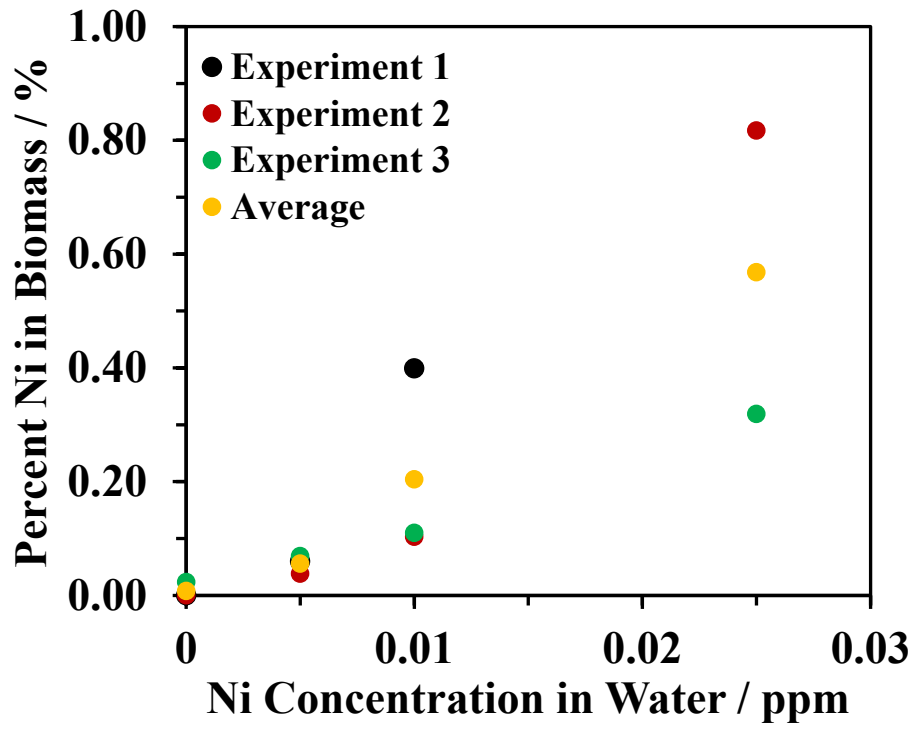


Figure A7.2. ICP-OES data of WH nickel uptake from all experiments.

Table A7.1. Specific capacitances of from all electrochemical performance testing with energy densities.

Sample Name	Cyclic Voltammetry, 3-Cell / F g ⁻¹				Charge-Discharge, 3-Cell / F g ⁻¹				
	5 mV s ⁻¹	20 mV s ⁻¹	50 mV s ⁻¹	100 mV s ⁻¹	0.1 A g ⁻¹	1 A g ⁻¹	3 A g ⁻¹	5 A g ⁻¹	10 A g ⁻¹
WH-0	356	305	256	199	217	174	155	133	110
WH-5	541	472	400	336	334	264	242	228	203
WH-10	264	208	157	107	166	124	96	88	80
WH-25	159	139	122	91	92	77	77	62	53
Sample Name	Charge-Discharge, 2-Cell / F g ⁻¹					Other Electrochemical Characterizations			
	0.1 A g ⁻¹	1 A g ⁻¹	3 A g ⁻¹	5 A g ⁻¹	10 A g ⁻¹	Energy Density, 0.1 A g ⁻¹ / W h kg ⁻¹			
WH-0	110	74	63	55	40	15.3			
WH-5	220	66	45	35	20	30.5			
WH-10	84	61	51	45	30	11.6			
WH-25	46	36	33	25	20	6.4			

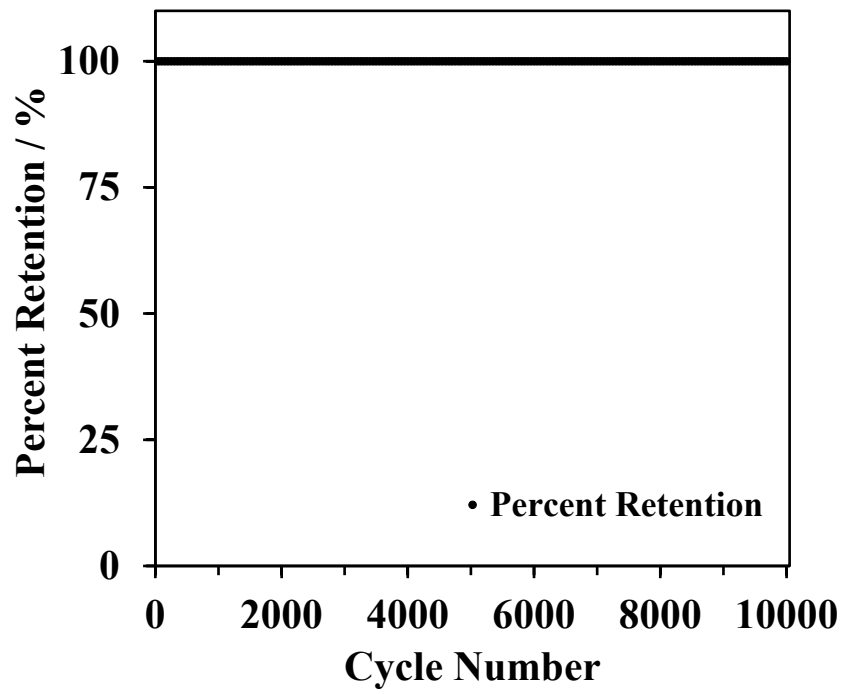


Figure A7.3. Percent retention for WH-5 biocarbon fabricated into a CR2032 coin cell.

Appendix A8. Supplemental for Electrochemical Studies on Graphitized Biocarbon Derived from Hydrothermally Liquefied Low Ash Content Corn Stover

Table A8.1. Reported parameters of various biomass-derived biocarbons.

Biomass	Activation method	SSA (m ² g ⁻¹)	V _{BET} (cm ³ g ⁻¹)	Capacitance (F g ⁻¹)	Retention (%)	Reported Cycles	Electrolyte	Ref.
Corn Stover	ZnCl ₂ /NiNO ₃	753	0.27	316	100	10000	2 M KOH	-
Corn Stover	Microwave pyrolysis	1433	0.76	246	n/a	n/a	n/a	[66]
Corn Stover	Facile thermal carbonization	215	0.12	242	92	2500	2 M KOH	[113]
Corn Cob	KOH	3054	1.50	328	91	10000	0.5 M H ₂ SO ₄	[149]
Corn Stem	KOH	1420	n/a	232	n/a	10000	n/a	[98]
Corn Silk	KOH	2285	1.44	160	87.6	n/a	6 M KOH	[68]
Corn Husk	KOH, thermal carbonization	867	0.51	356	95	2500	6 M KOH	[69]
Corn Stalk	KOH, Ni catalyst	2495	1.23	323	98	1000	6 M KOH	[100]
Corn Stalk	Fe catalyst, pyrolysis	540	0.48	213	99 (columb.)	6000	6 M KOH	[67]
Corn Straw	Hydrothermal carbonization	1771	1.85	222	94	5000	6 M KOH	[99]
Corn Starch	H ₃ PO ₄	1167	1.80	162	93	5000	6 M KOH	[65]
Fungi	Hydrothermal	80	0.50	196	99	1000	6 M KOH	[207]
Fish scale	KOH	2273	2.74	168	77	n/a	7 M KOH	[208]

Seaweed	Thermal	15 - 1307	n/a	119~264	89	10000	1 M H ₂ SO ₄	[209]
Tea-leaves	KOH	2245 - 2841	1.07 - 1.37	275 - 330	92	2000	2 M KOH	[210]
Waste paper	KOH	416	0.225	180	99	2300	6 M KOH	[211]
Banana peel	Hydrothermal	1650	1.26	206	88	1000	6 M KOH	[212]
Sunflower seed shell	KOH	619 - 2585	0.48 - 0.62	213 - 311	n/a	n/a	30% KOH	[213]
Wheat straw	KOH	2316	1.50	251	n/a	n/a	MeEt ₃ NBF ₄ /AN	[214]
Silk protein	KOH	2557	n/a	264	93	10000	1 M H ₂ SO ₄	[215]
				168	97		BMIM BF ₄ /AN	
Pollen	Hydrothermal and KOH	3037	2.27	185	96	5000	TEABF ₄ /AN	[216]
				207	95		EMIM BF ₄	
Rice husk	CO ₂	1500	n/a	76	95	5000	TEABF ₄ /PC	[217]
Animal bone	KOH	2157	2.26	185	n/a	n/a	7 M KOH	[218]
Cherry stone	KOH	1171	0.67	232	n/a	n/a	2 M H ₂ SO ₄	[219]
				120			TEABF ₄ /AN	
Fir wood	Steam	1064	0.61	180	n/a	n/a	0.5 M H ₂ SO ₄	[220]
		1016	0.75	110			6 M KOH	
Coconut shell	ZnCl ₂	1874	1.21	268	> 99	5000	6 M KOH	[221]
				196	n/a		TEABF ₄ /PC	
Lignin	KOH	3775	2.70	286.7	n/a	n/a	6 M KOH	[222]
Lignin	KOH	2265	n/a	336	100	1000	6 M KOH	[223]
Lignin	Composite	802	n/a	880	96	5000	6 M KOH	[224]
Lignin	KOH	2957	1.79	348	100	10000	1 M KOH	[225]

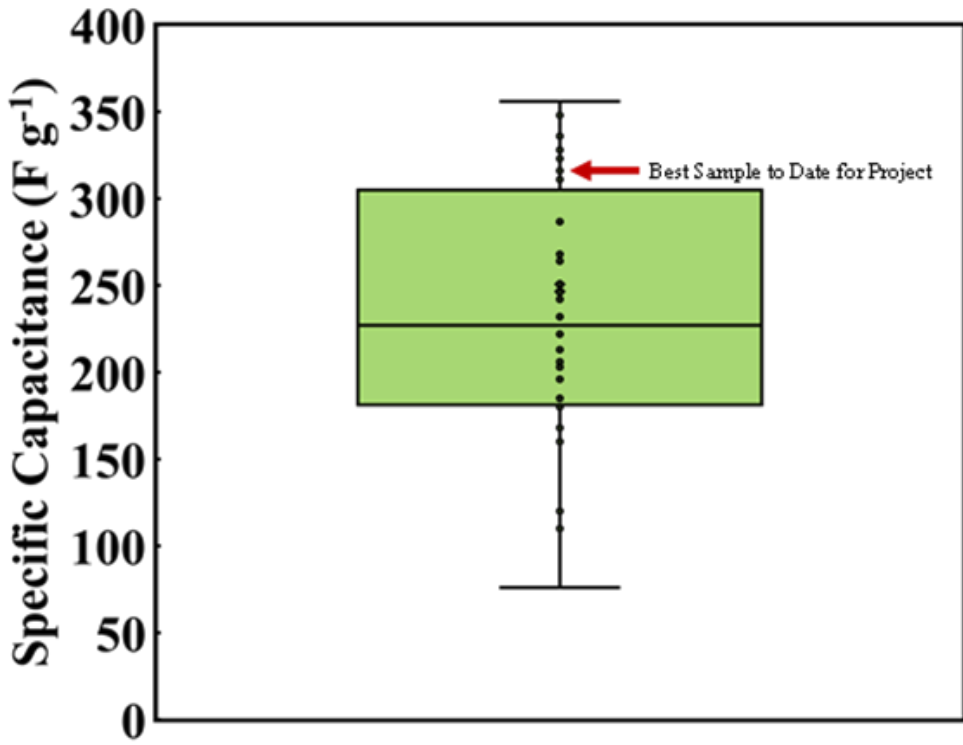


Figure A8.1. Box and whisker plot of specific capacitance values denoted in Table S1.

Appendix 9A. Mechanism of Electrochemical Impedance Spectroscopy (EIS)

EIS is performed to determine internal resistances associated with various aspects of the electrode materials, thus providing important details into material characteristics. It is important to understand how this testing works in order to draw conclusions based on the plots derived from experimental data. To begin, impedance is measured by applying an AC voltage (potential) and measuring the subsequent current. Current is denoted as the sum of several sinusoidal waves, known as a Fourier series. For electrochemical cells the current derived at a particular potential is the same frequency as the potential, but shifted with respect to the voltage wave (Figure 9A.1). This is known as a phase shift. A common way to plot the results of electrochemical impedance is through Nyquist plots. Nyquist plots utilize Equation 9A.1 for obtaining the X and Y-axis parameters.

$$Z(\omega) = Z_0(\cos(\phi) + j\sin(\phi))$$

Where Z is the generalized expression of impedance, ω is the radial frequency in Hz, Z_0 is impedance at $\omega=0$, and ϕ is the phase shift. $Z(\omega)$ contains real (Z') and imaginary (Z'') counterparts that are plotted on the X and Y-axis respectively. Each point on the plot denotes the impedance at one frequency. During testing the frequency can change orders of magnitude, depending on the specified frequency parameters, giving the various regions designated in this dissertation.

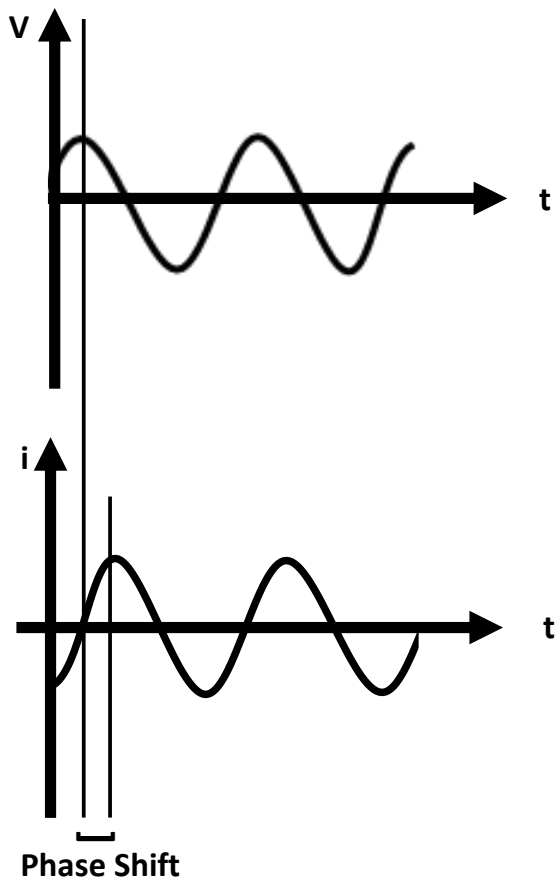


Figure 9A.1. Depiction of the phase shift that occurs when a voltage is applied during EIS.